Understanding the Electrochemical Reaction Mechanism of Manganese- and Iron-based Layered Cathode Materials for Sodium Batteries

Zur Erlangung des akademischen Grades eines
DOKTORS DER NATURWISSENSCHAFTEN
(Dr. rer. nat.)

von der KIT-Fakultät für Chemie und Biowissenschaften
des Karlsruher Instituts für Technologie (KIT)
genehmigte

DISSERTATION

von
M. Sc. Jiali Peng
aus Jiangsu, China

KIT-Dekan: Prof. Dr. Rolf Schuster
Referent: Prof. Dr. Helmut Ehrenberg
Korreferentin: Prof. Dr. Annie Powell
Tag der mündlichen Prüfung: 27.10.2023

Contents

Abbreviation, Constants, Symbols

LIBs	Lithium-ion batteries
SIBs	Sodium-ion batteries
SRD	Synchrotron radiation diffraction
TM	Transition metal
XANES	X-ray absorption near edge spectroscopy
NMR	Nuclear magnetic resonance
sXAS	Soft X-ray absorption spectroscopy
HVs	Hybrid vehicles
O	Octahedral
P	Prismatic
EC	Ethylene carbonate
PC	Propylene carbonate
DMC	Dimethyl carbonate
DEC	Diethyl carbonate
EMC	Ethyl methyl carbonate
VC	Vinylene carbonate
FEC	Fluoroethylene carbonate
SEM	Scanning electron microscope

EDX	Energy-dispersive X-ray
HRTEM	High-resolution transmission electron microscopy
HAADF-STEM	High-angle annular dark-field scanning transmission electron microscopy
EDS	Energy dispersive X-ray spectroscopy
C65	Conductive carbon
PVDF	Poly (vinylidene difluoride)
NMP	1-methyl-2-pyrrolidinone
GITT	Galvanostatic intermittent titration technique
V_m	Molar volume
SoC	State of charge
OCV	Open circuit voltage
EELS	Electron energy loss spectroscopy
IS	Isomer shift
QS	Quadrupolar splitting
iFY	Inverse fluorescence yield
PDF	Pair distribution function
U^o	Open-circuit potential

Abstract

Energy production and storage technologies have attracted a great deal of attention for day-to-day applications. The development of lithium-ion batteries (LIBs) have been the main focus because of their high energy density and almost every portable device today is operated by various forms of LIBs. However, the sustainability and limited availability of lithium metals have motivated researchers to seek for alternative energy storage systems. Sodium-ion batteries (SIBs) are considered as the best candidate for power sources owing to the abundance and low cost of foreseen raw materials, driving the energy storage to high-scale and low cost. Although several materials have been explored, further processes toward high performance cathode materials are still needed. Among many cathode candidates, layered sodium transition metal oxides ($NaTMO_2$, TM = Ti, V, Cr, Mn, Fe, Co, Ni, and a mixture of 2 or 3 of these elements) offer many advantages due to their simple structures, high capacities, and ease of synthesis. This thesis mainly focuses on the design strategy, characterization, and investigation of the electrochemical reaction mechanism of manganese- and iron-based layered cathode materials for SIBs.

Fe/Mn-based layered oxides are an appealing system from an application point of view owing to natural abundance, environmental benignity, high operating voltage of Fe^{3+}/Fe^{4+}, and large specific capacity of Mn^{3+}/Mn^{4+}. Pure P2-type ($P6_3/mmc$) $Na_{2/3}Fe_{1/2}Mn_{1/2}O_2$ (NMFO) and O3-type (R-3m) $NaFe_{1/2}Mn_{1/2}O_2$ were synthesized by controlling the ratio of Na/(Fe and Mn) and temperature. *In situ* synchrotron radiation diffraction (SRD) was utilized to investigate the structural evolution during cycling. In contrast with O3-type $NaFe_{1/2}Mn_{1/2}O_2$, P2-type NMFO delivers a large capacity of 190 mAh g^{-1} at 0.05 C rate and better cycling stability with an average voltage of 2.8 V.

However, the phase changes at high voltage and the Jahn-Teller effect are still the drawbacks of P2-type NMFO which lead to short cycle life and poor rate capability. In this regard, this

thesis describes the optimization of the structure of a NMFO cathode via partial substitution of Fe by Mn and Ti and exploration of the redox activity of P2-type Mn/Fe-based layered cathodes. Furthermore, the investigation of the effect of simultaneous Mn/Ti cationic substitution on the electrochemical performance and structural stability of P2-NMFO are also presented. The obtained P2-$Na_{2/3}Mn_{7/12}Fe_{1/3}Ti_{1/12}O_2$ (NMFTO) exhibits a solid solution mechanism during the complete desodiation/resodiation process and delivers an initial discharge capacity of 170 mAh g^{-1} at 0.1 C rate and a capacity retention of 80% after 50 cycles. The modified P2 composition has a stable cycle performance in the potential window from 1.5 V to 4.5 V vs Na^+/Na. The main focus of this research is to understand the electrochemical mechanism of the layered cathode material P2-NMFTO by exploring the redox processes of transition metal (TM) cations and oxygen anions upon cycling. *In situ* X-ray absorption near edge spectroscopy (XANES) is used to elucidate the local electronic structure of Fe and Mn atoms and their evolution throughout electrochemical cycling. ^{23}Na solid-state nuclear magnetic resonance (NMR) spectroscopy is used to investigate the changes in the Na environments during desodiation/resodiation. *Ex situ* soft X-ray absorption spectroscopy (sXAS) reveals the participation of oxygen anions in the electrochemical reactions.

Beside the improvements of different materials to explore their electrochemical reaction mechanism, the research performed within this thesis also involves the comparison and investigation of P2-, P2/P3- and P3-type cathodes with same compositions. Different types of NMFTO were synthesized from same precursors at different heating temperature. To understand the electrochemical reaction mechanism of these cathodes, a series of *in situ* and *ex situ* measurements were utilized. Furthermore, the cycling stability of these different materials were compared at different voltage windows to explore materials with higher capacity and cycling stability.

These discoveries not only contribute to a comprehensive understanding of the correlation between preparation, structure and performance for next-generation SIBs, but also provide new

insights into the reaction mechanism of different phases during synthesis and electrochemical cycling.

Zusammenfassung

Technologien zur Energieerzeugung und -speicherung haben für alltägliche Anwendungen große Aufmerksamkeit auf sich gezogen. Die Entwicklung von Lithium-Ionen-Batterien (LIBs) stand wegen ihrer hohen Energiedichte im Mittelpunkt, und fast jedes tragbare Gerät wird heute mit verschiedenen Formen von LIBs betrieben. Allerdings haben die Nachhaltigkeit und die begrenzte Verfügbarkeit von Lithiummetallen die Forscher dazu veranlasst, nach alternativen Energiespeichersystemen zu suchen. Natrium-Ionen-Batterien (SIBs) gelten als die besten Kandidaten für Energiequellen, da die vorgesehenen Rohstoffe im Überfluss vorhanden und kostengünstig sind, was die Energiespeicherung in großem Maßstab und zu niedrigen Kosten ermöglicht. Obwohl bereits mehrere Materialien erforscht wurden, sind weitere Verfahren zur Entwicklung von Hochleistungs-Kathodenmaterialien erforderlich. Unter den vielen Kathodenkandidaten bieten geschichtete Natrium-Übergangsmetalloxide ($NaTMO_2$, TM = Ti, V, Cr, Mn, Fe, Co, Ni und eine Mischung aus 2 oder 3 Elementen) aufgrund ihrer einfachen Strukturen, hohen Kapazitäten und einfachen Synthese viele Vorteile. Diese Arbeit konzentrierte sich hauptsächlich mit der Designstrategie, der Charakterisierung und der Untersuchung des elektrochemischen Reaktionsmechanismus von Mangan- und Eisen-basierten Schichtkathodenmaterialien für SIBs.

Schichtoxide auf Fe/Mn-Basis sind aufgrund ihres natürlichen Vorkommens, ihrer Umweltfreundlichkeit, der hohen Betriebsspannung von Fe^{3+}/Fe^{4+} und der großen spezifischen Kapazität von Mn^{3+}/Mn^{4+} ein attraktives System für Anwendungen. Reiner P2-Typ (*P*63/*mmc*) $Na_{2/3}Fe_{1/2}Mn_{1/2}O_2$ (NMFO) und O3-Typ (*R*-3*m*) $NaFe_{1/2}Mn_{1/2}O_2$ wurden durch Kontrolle des Verhältnisses von Na/(Fe und Mn) und Temperatur synthetisiert. Mit Hilfe der In-situ-Synchrotronstrahlungsbeugung (SRD) wurde die strukturelle Entwicklung während des Zyklus untersucht. Im Gegensatz zum O3-Typ $NaFe_{1/2}Mn_{1/2}O_2$ liefert der P2-Typ NMFO eine hohe

Kapazität von 190 mAh g^{-1} bei Rate von 0,05 C und eine bessere Zyklenstabilität mit einer durchschnittlichen Spannung von 2,8 V.

Die Phasenveränderungen bei hoher Spannung und der Jahn-Teller-Effekt sind jedoch nach wie vor die Nachteile von P2-NMFO, die zu einer kurzen Zyklenlebensdauer und einer schlechten Ratenfähigkeit führen. Vor diesem Hintergrund wird in dieser Arbeit die Optimierung der Struktur einer NMFO Kathode durch partielle Substitution von Fe^{3+} durch Mn^{4+} und Ti^{4+} beschrieben und die Redoxaktivität von P2-Typ Mn/Fe-basierten Schichtkathoden untersucht. Darüber hinaus wurden die Auswirkungen der gleichzeitigen kationischen Substitution von Mn/Ti auf die elektrochemische Leistung und die strukturelle Stabilität von P2-NMFO untersucht. Die erhaltene P2-$Na_{2/3}Mn_{7/12}Fe_{1/3}Ti_{1/12}O_2$ (NMFTO) zeigt einen Mechanismus der festen Lösung während des vollständigen Desodierungs-/Resodierungsprozesses und liefert eine anfängliche Entladungskapazität von 170 mAh g^{-1} bei einer Rate von 0,1 C und eine Kapazitätserhaltung von 80% nach 50 Zyklen. Die modifizierte P2-Zusammensetzung weist eine stabile Zyklusleistung im Potenzialfenster von 1,5 V bis 4,5 V gegen Na^+/Na. Das Hauptaugenmerk dieser Forschung liegt auf dem Verständnis des elektrochemischen Mechanismus des Schichtkathodenmaterials P2-NMFTO durch die Untersuchung der Redoxprozesse von Übergangsmetallkationen (TM) und Sauerstoffanionen während des Zyklus. In situ Röntgenabsorptionsspektroskopie (XANES) wird verwendet, um die lokale elektronische Struktur von Fe- und Mn-Atomen und ihre Entwicklung während des elektrochemischen Zyklus zu erforschen. ^{23}Na-Festkörpermagnetresonanzspektroskopie (NMR) wird verwendet, um die Veränderungen in den Na-Umgebungen während der Desodierung/Resodierung zu untersuchen. Ex-situ-Soft-Röntgenabsorptionsspektroskopie (sXAS) zeigt die Beteiligung von Sauerstoffanionen an den elektrochemischen Reaktionen.

Neben den Verbesserungen der verschiedenen Materialien zur Erforschung ihres elektrochemischen Reaktionsmechanismus zu erforschen, umfasst die Forschung im Rahmen dieser Arbeit auch den Vergleich und Untersuchung von P2-, P2/P3- und P3-Type Kathoden

mit gleichen Zusammensetzungen. Die verschiedenen NMFTO-Typen wurden aus denselben Vorläufern bei unterschiedlichen Heiztemperaturen synthetisiert. Zum Verständnis der Unterschiede und elektrochemischen Reaktions dieser Kathoden zu verstehen, wurden eine Reihe von in situ und ex situ Messungen durchgeführt. Darüber hinaus wurde die Zyklenstabilität dieser verschiedenen Materialien in unterschiedlichen Spannungsfenstern verglichen, um Materialien mit höherer Kapazität und Zyklenstabilität zu finden.

Diese Entdeckungen tragen nicht nur zu einem umfassenden Verständnis der Zusammenhänge zwischen Herstellung, Struktur und Leistung von SIBs der nächsten Generation bei, sondern liefern auch neue Erkenntnisse über den Reaktionsmechanismus der verschiedenen Phasen während der Synthese und der elektrochemischen Zyklen.

Chapter 1 Motivation & Outline

Intensive research efforts in sustainable energy conversion and storage devices are required to achieve the goal of carbon neutrality by the mid-21st century[1]. Electrochemical secondary batteries can be used for large-scale storage of electricity due to their flexibility, high energy conversion efficiency, and simple maintenance. Lithium-ion batteries (LIBs) have become common power sources in the portable electronic market due to their energy density and long cycle life. However, with the increasing of market volume of hybrid electric vehicles (EVs) and stationary storage, the cost and supply are raised because of the non-uniform distribution and low abundance of lithium and cobalt within the Earth's crust[2, 3]. Due to the unlimited distribution of sodium metal and the similar cell configuration and working mechanism to LIBs, sodium-ion batteries (SIBs) have been proven as ideal and potential alternatives for long-scale energy storage systems[4].

Advanced SIBs with higher energy and powder densities, better cycle life and lower cost which are correlated to the composition, structure and reaction mechanism of electrode active materials are needed to enable the practical implementation[5, 6]. Many sodium-ion cathode materials have been selected for first generation of commercial SIBs, including Prussian blue/white[7], phosphates[8], and organic materials[9] which have the demerits of intrinsic water toxicity, low specific capacity, and low capacity retention. The easy synthesis of layered transition metal oxides, Na_xTMO_2 ($0<x<1$ and TM = transition metals), are of particular interest for SIBs due to their promising electrochemical properties[10-12]. In Na_xTMO_2, TM ions reside within layers of edge sharing metal-oxide (TMO_6) octahedra, while Na ions are sandwiched in between these oxide layers. According to the surrounding Na environment and the number of unique oxide layer packing, Na layered oxides can be synthesized in O3-, P2-, P3-phases. The letters O (octahedral) and P (prismatic) indicate the Na local environment and are followed by

the number of unique interlayers which are surrounded by different oxide layers[13]. A prime (') symbol is added to the nomenclature to differentiate the corresponding distorted materials[14].

In the O3 structure type, the oxygen layers stacking follows the ABCABC pattern. Na^+ ions are located on octahedral NaO_6 sites which only share edges with the surrounding TMO_6 octahedra. Materials with an O3 structure type are commonly obtained for a Na/TM ratio equal or close to one. In the P2-phase, oxide layer stacking follows the ABBA pattern and all NaO_6 octahedra share either common edges (Na_e site) or common faces (Na_f site) with neighboring TMO_6 octahedra. The observed Na_f : Na_e ratio is usually close to 1 : 2. In the P3 structure type, the oxygen layers stacking follows an ABBCCA sequence and the Na^+ ions occupy prismatic sites sharing faces and edges with the surrounding TMO_6 octahedra[13].

Electrochemical behaviors are influenced by the structure of the phase not only because of the amount of Na in the pristine state but also due to the stability of each layer and kinetics affected by the surrounding environment of Na. Therefore, the objective of this PhD thesis is to understand the electrochemical reaction mechanism of manganese- and iron-based layered cathode material for sodium batteries. The research work can be divided into three parts:

(1) The first part describes the synthesis and includes an overall comparison of pure P2 and O3 phase $Na_x(Mn_{1/2}Fe_{1/2})O_2$ and an investigation of the structure and electrochemical properties of layered cathode materials with different Fe, Mn, and Ti fractions in TM layers.

(2) The second part is a structural optimization of the P2-type layered NMFO positive electrode material via a partial substitution of Fe by Mn and Ti in order to explore the electrochemical mechanism of redox activity of P2-type Mn/Fe based layered cathodes.

(3) The last part compares the electrochemical properties of P2-, P2/P3- and P3-type cathodes with same compositions and investigates the redox reactions of transition metals and oxygen to explain the mechanism of the better electrochemical performance of P3-type Mn/Fe based layered cathodes.

Chapter 2 Fundamentals of Sodium Secondary Batteries

Batteries are electrochemical devices that operate by converting chemical energy into electrical energy. A battery consists of one or more electrochemical cells, primarily comprised of a positive electrode (cathode), a negative electrode (anode), a separator, and an electrolyte medium (ion conductor). During the operation of a battery, electrons migrate through an electron conductor (electrode) accompanied by the migration of ions through an ion conductor (electrolyte) to ensure the maintenance of electrical neutrality[15]. Based on the reversibility of chemical reactions, batteries can be classified as primary batteries and secondary batteries. Primary batteries are designed to be used only once because the reaction that occurs is not (completely) reversible. Secondary batteries, also known as rechargeable batteries, can be recharged after discharge, and the application of a current can reverse the chemical reaction that occurs during discharge.

2.1 Basic concepts of sodium ion batteries

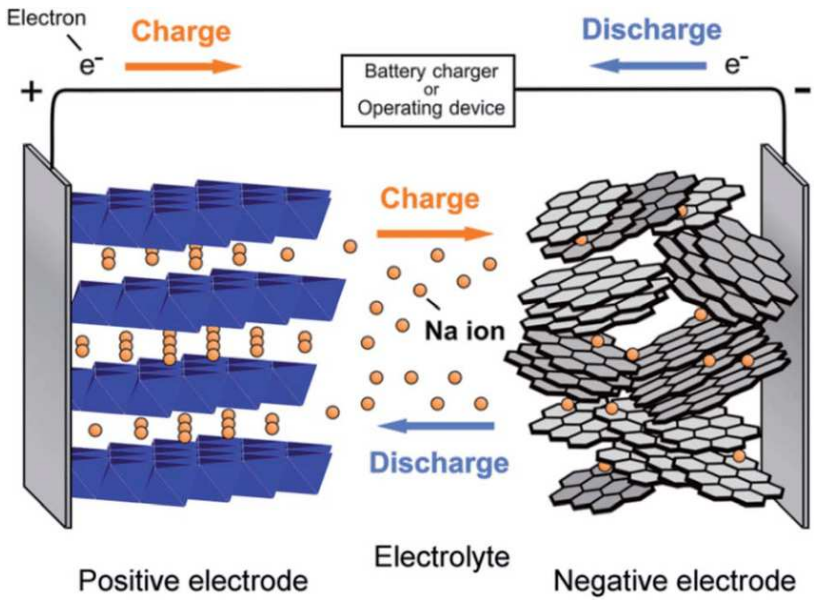

Figure 2.1 Schematic illustration of sodium-ion battery. Adapted from reference[16].

SIBs use the alkali ions only as charge carries while energy is reversibly stored and released in intercalation and/or conversion electrodes, as illustrated in Figure 2.1[16]. As any generic alkali-

ion-shuttling battery, SIBs typically consist of one positive electrode, one negative electrode, electrolyte, separator, and battery case. When charged, sodium ions are extracted from the cathode material (positive electrode) and shuttle through the electrolyte to transfer to the anode material, while electrons move along the external circuit in the same direction. The discharge process of sodium batteries involves the flow of electrons from the anode to the cathode through an external circuit. Sodium ions are released from the anode electrode and move through the electrolyte towards the cathode. During the discharge process, the electrolyte also plays a critical role by transporting the sodium ions between the two electrodes.

Due to the increasing demand for energy storage systems, SIBs provide an attractive alternative because of the wide availability and accessibility of sodium. The selection of electrode materials is very important for the electrochemical performance of batteries, as the deintercalation/intercalation reaction of sodium is closely related to the intrinsic properties of the electrode materials. Figure 2.2 illustrates several representative candidate materials such as anode and cathode materials, electrolytes and binders which have been identifies as the most promising materials[17]. Improvements need to be made to the following key parameters in order to develop advanced electrode materials for the next generation of sodium-ion batteries:

- high rate capability
- high energy density
- long cyclability
- low cost
- high safety

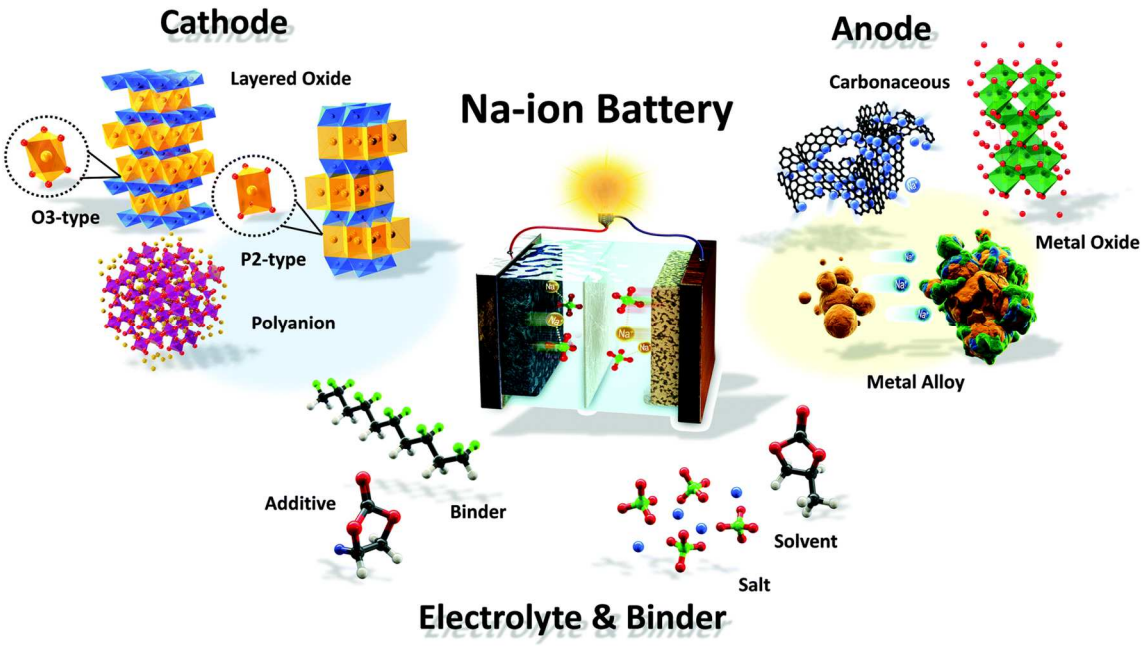

Figure 2.2 The illustration of electrode and electrolyte materials in sodium-ion battery system. Adapt from reference[17].

2.2 Anode materials for sodium-ion batteries

Research on anode materials for SIBs can be divided into three main categories based on the reaction mechanism occurring during the sodiation/resodiation processes, which are represented in Figure 2.3: (1) insertion reaction materials, (2) alloying reaction materials, (3) conversion reaction materials[18].

Carbonaceous and titanium-based oxides have been extensively studied as anodes for SIBs which are based on insertion reaction. Carbon-based materials are widely accepted due to their ability to accommodate Na^+ ions into their structure[19]. In general, low operational potential can lead to safety issues like the formation of metal sodium plating and sodium dendrites on the anode surface in practical applications[20, 21]. Similar to LIBs, metal oxide compounds have been studied as Na^+ ion insertion host materials. Titanium-based oxides, such as titanium dioxide[22-24], spinel lithium titanium oxide[25, 26], and sodium titanium oxide[27-29] are particularly interesting as anodes because they have reasonable working voltage, cost, and non-toxicity[30, 31].

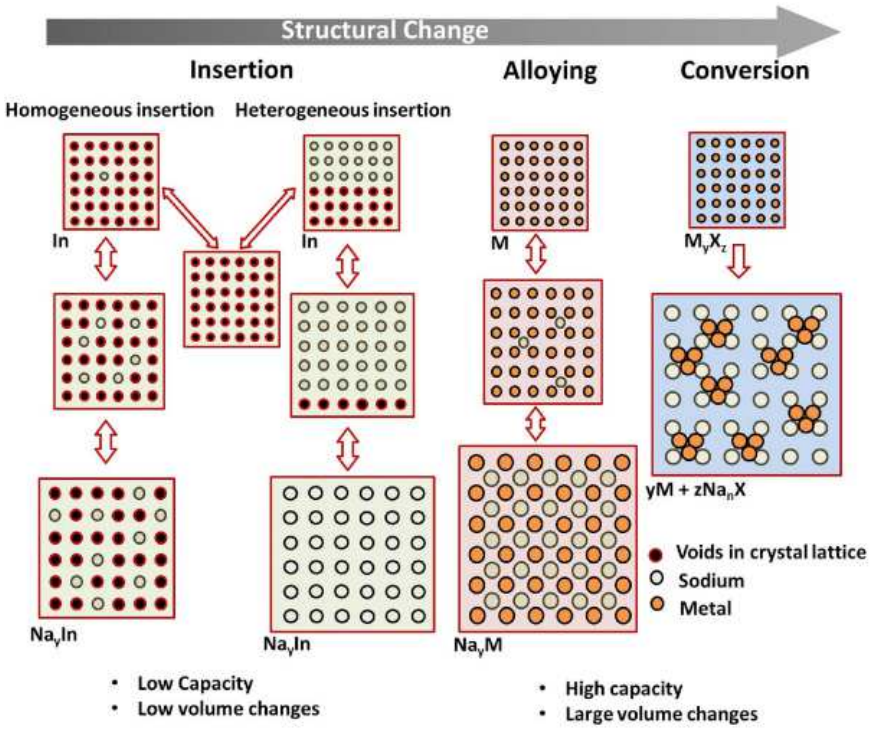

Figure 2.3 Schematic representation of reaction mechanisms occurring during storage of Na^+ in various classes of anode materials. In= Insertion/Intercalation host. Adapt from reference[18].

Na^+ insertion materials have been successfully applied as Na storage materials but they still suffer from limited capacity utilization due to their intrinsic constraints, e.g. available Na sites. Alloying materials are suggested as attractive anodes for SIBs because they can store a large amount of sodium ions in the structure, with a relatively low working potential (below 1.0 V)[32]. Metal (Sn, Bi), metalloid (Si, Ge, As, Sb)[33], and multi-atomic non-metallic compounds (P) in group 14 or group 15[34]of the periodic table have been extensively studied as potential anode materials for SIBs. To date, various experimental efforts have focused on the electrochemical and mechanical reactions of these alloys with Na, and ideal structures and/or enhanced electrode designs have been investigated[17].

Unlike insertion reaction materials and alloying reaction materials, conversion reaction materials, such as transition metal oxides[35], transition metal sulfide[36] and transition metal phosphide[37] compounds, involve the chemical conversion of one or more elements from a host

lattice to form new compounds[38]. The generalized formula for Na-based conversion reaction can thus be written as[39]:

$$\mathrm{M}_y\mathrm{X}_Z + (\mathrm{zn}) \cdot \mathrm{Na} \rightleftharpoons \mathrm{yM} + \mathrm{z}Na_n\mathrm{X}$$

where X represents either oxygen or sulfur in the host compound, and n, y, and z define the stoichiometric composition of the starting material and the formed Na-containing compound. Similar to the reaction in LIBs, conversion reaction materials have been considered as potential anodes for SIBs due to their high theoretical specific capacity. The idea anode materials should possess an elemental in its composition with low weight and low density and possess a potential as close to that of pure sodium metal as possible.

2.3 Electrolytes

Electrolytes play a critical role for performance and safety of batteries. They separate the electrodes and provides proper ion transfer between cathodes and anodes during the cycling process[40]. An ideal electrolyte should satisfy the following criteria[41-43]:

1) High electrochemical and chemical stability to ensure that no chemical reaction occurs at the surface of electrodes within the operating voltage window.
2) Wide operating temperature range to allow the solvent to remain in the liquid state at the desired operating temperature because of the performance advantages of using liquid electrolytes in batteries.
3) High ionically conductive and electronically insulating behavior to reduce the cell resistances and to avoid the cell short-circuit.
4) High dielectric permittivity to allow the solvent to dissolve a high concentration of solutes.
5) Low toxicity with low production cost. The solvent should be nontoxic and available at low cost to ensure sustainability.

The electrolyte of SIBs is composed of solvent, sodium salt and additives, the proportion of which depends on the technology and voltage range, and also on the usage. The salt should exhibit: (1) solubility in the solvent, (2) stability versus reduction and oxidation, (3) chemical stability against the cell components, (4) safety concerns during cycling. The solvent should: (1) be polar with a high dielectric constant, (2) exhibit low viscosity in order to improve the ionic mobility, (3) remain inert to the charged surfaces of the cathode and the anode during cell operation, and (4) have a wide liquid range (i.e. a low melting point and a high boiling point)[44, 45]. In previous studies, $NaClO_4$ and $NaPF_6$ were used as electrolyte salts in carbonate-ester binary or ternary mixtures, which have become the dominant electrolyte compositions used for Na^+ chemistry[46]. Komaba et al. investigated the electrochemical performance of hard carbon anodes in sodium cells in beaker-type cells with various electrolyte solvents containing 1 M $NaClO_4$ salt in EC, PC, EC: DMC (50: 50, *v/v*), EC: EMC (50: 50, *v/v*), EC: DEC (50: 50, *v/v*), and PC: VC (98: 2, *v/v*). The results showed that 1 M $NaClO_4$ in PC, EC and EC: DEC solutions exhibited better electrochemical performance than the other mixtures[47].

2.4 Cathode materials for sodium-ion batteries

2.4.1 Layered transition-metal oxides

Early investigation of sodium-based layered oxides was performed by Delmas in the early 1980s[13, 14, 48]. Layered oxides, Na_xTMO_2 (TM: transition metal elements), are composed of repeating sheets of edge-sharing TMO_6 octahedral layers with Na ions being sandwiched in between the oxide layers[17]. Typical Na_xTMO_2 can be classified into O3-, O2-, P2-, and P3-phases as shown in Figure 2.4 depending on the surrounding Na environment and the number of unique oxide layer packings, in which the letter indicates the environment where Na ions are accommodated at octahedral (O) and prismatic (P) sites and the following number indicates the number of unique interlayers that are surrounded by different oxide layers. The prime symbol (') is added to the abbreviation when the crystal lattice contains in-plane distortion[49].

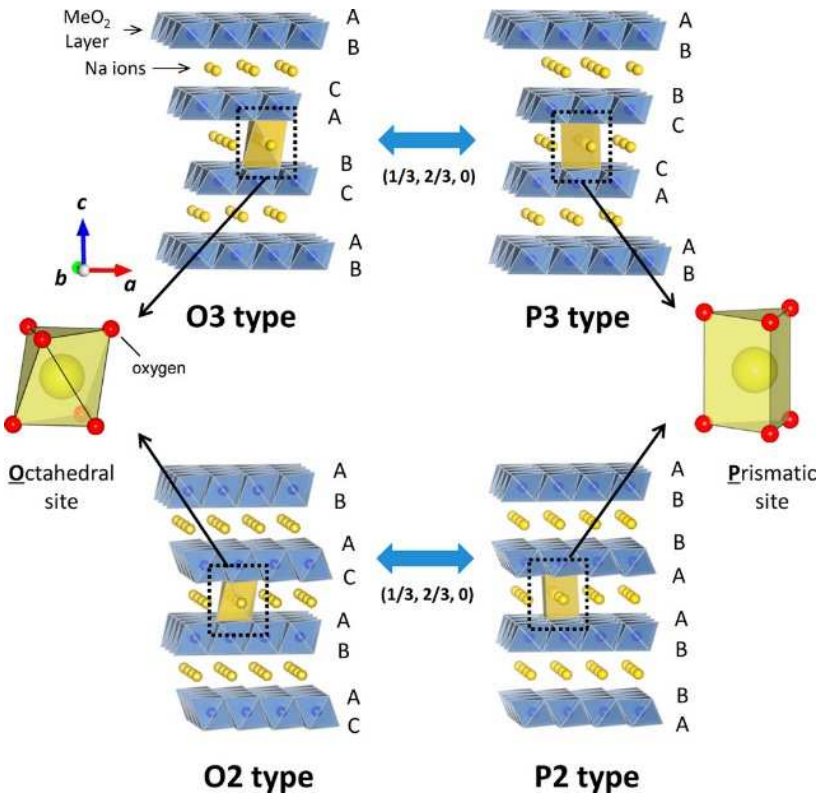

Figure 2.4 Classification of Na-Me-O layered materials with sheets of edge-sharing MeO_6 octahedra and phase transition processes induced by sodium extraction. Adapted from reference[16].

O3-type Na_xTMO_2 which is classified as a 3R phase with a space group of R-3m is stable when x is close to 1, in which the average oxidation state of TM is close to 3+[16]. Sodium and 3d transition-metal ions are accommodated at distinct octahedral (O) sites in O3-type layered oxides, and edge-shared NaO_6 and TMO_6 octahedra order into alternate layers perpendicular to the [111] direction, forming the NaO_2 and TMO_2 slabs. Every unit cell of O3-type Na_xTMO_2 is composed of three different TMO_2 layers (AB, CA, and BC), and sodium ions are accommodated at "O" sites between TMO_2 layers. Electrochemical de-/sodiation of the O3 structure progresses with reversible structural transformation of O3↔O'3↔P3↔P'3[16]. Sodium ions can also be located at trigonal "prismatic" (P) sites because of their larger size compared to lithium ions. For the P3-type phase, prismatic sites which are formed by the gliding of TMO_2 slabs with the oxygen packing (AB, BC, and CA) become energetically stable when sodium

ions are partly extracted from the O3-type phase. In some cases, the P3-type phase can be synthesized by solid-state reaction without electrochemical sodium extraction in Na batteries[50].

The P2-type layered structure which is classified as 2H phase with a space group of $P6_3/mmc$ consists of two different TMO_2 layers (AB and BA). For P2-type Na_xTMO_2, the structure is stable if the value of x is in the range of 0.3~0.7. In the P2-type structure, sodium ions occupy two different types of prismatic sites: Na_f (Na_1) which is in contact with two TMO_6 octahedra of the adjacent slabs along its face and Na_e (Na_2) which is in contact with six surrounding TMO_6 octahedra along its edges[55]. Usually, electrochemical de-/sodiation of the P2-type structure progresses with reversible structural transformation of P2↔O2. At low potentials (<2.0 V vs Na/Na^+), there is a phase transition P2-P2' associated with the manganese redox activity and a significant Jahn-Teller distortion[51]. The O2-type phase is formed by the gliding of TMO_2 slabs from prismatic sites to octahedral sites after extraction of sodium ions. This O2-type phase contains two different TMO_2 layers (AB and AC) with a unique oxygen packing, "AB AC AB". Two glide vectors (1/3, 2/3, z) and (2/3, 1/3, z) of slabs exist to form O2 phase, which induces formation of stacking faults after sodium extraction from the P2 phase[52].

2.4.1.1 Iron- and manganese-based layered oxides and derivatives

Na_xFeO_2

Iron-based cathode materials also have been an important topic in the battery field because iron is one of the most abundant, nontoxic, and environmentally friendly transition metals on the earth crust[53]. De-intercalation does not occur in lithium batteries[54-56], because the randomization of the iron distribution from the 3b ordered state to the 3b-6c disordered state during charge resulting an irreversible capacity[57, 58]. Considering the poor performance of the iron-based layered oxide cathodes for lithium batteries, the successful operation of the Fe^{3+}/Fe^{4+} redox couples in sodium-ion batteries is very encouraging[59].

The compound $NaFeO_2$ has three different structural modifications called α, β and γ phase. The structure of α-$NaFeO_2$ with space group of R-3m can be derived from the rock-salt structure in which both iron and sodium ions are located on octahedral sites inside the cubic close packed oxygen structure in an ordered way with iron layers separated by O^{2-}-Na^{+}-O^{2-} sandwiches. α-$NaFeO_2$ is known as a typical example of a O3-type layered structure and easily prepared by conventional solid-state reaction[60]. Electrochemical reversibility and illustration of the redox activity the Fe^{3+}/Fe^{4+} couple during the desodiation/resodiation process for a single phase O3-$NaFeO_2$ are shown in Figure 2.5a and 2.5b[59]. Takeda et al. demonstrated electrochemical Na extraction from $NaFeO_2$ in nonaqueous Li/$NaFeO_2$ (lithium metal as a counter electrode)[57]. The reversible sodium cycling from α-$NaFeO_2$ in sodium-ion cells using a sodium metal counter electrode was first reported by Okada, in which the cell was charged up to 3.6 V to obtain the initial charge capacity of 103 mAh g^{-1} and reversibly discharged to 1.5 V to obtain an initial discharge capacity of 85 mAh g^{-1}. Yabuuchi et al. studied the influence of cutoff voltage on the sodium extraction process[61] and the migration of the Fe^{3+} into the neighboring tetrahedral site as shown in Figure 2.5c. The irreversible structural change was observed by *ex situ* X-ray diffraction analysis in their report when the $Na_{1-x}FeO_2$ electrode was charged beyond x > 0.5, and the acceptable cycling range was determined to be x = 0-0.45. The reversible process in the Na cell can be expressed as follows[16]:

$$NaFeO_2 \underset{reduction}{\overset{oxidation}{\rightleftharpoons}} \square_x\, Na_{1-x}FeO_2 + xNa^+ + xe^-$$

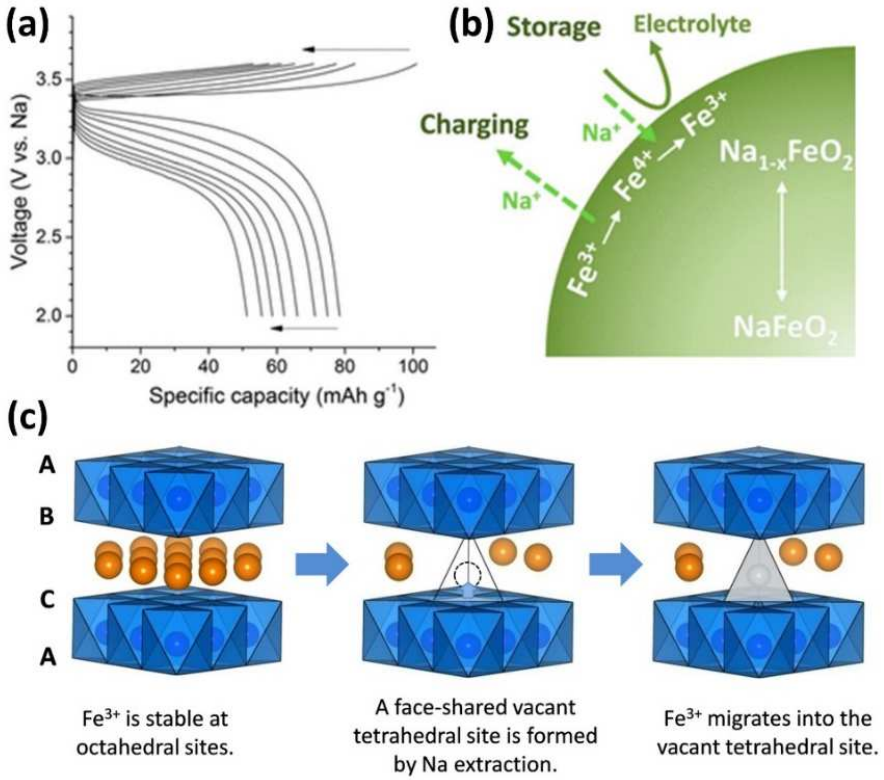

Figure 2.5 (a) Galvanostatic charge/discharge curves of Na/$NaFeO_2$ cell; (b) The illustration of the desodiation/resodiation of Na/$NaFeO_2$ cell during charge/discharge; (c) Proposed mechanism of the iron migration process on the sodium extraction. Adapted from reference[59].

β-$NaFeO_2$ has a structure with space group *Pna*, where oxygens ions form a hexagonal close packing and both iron and sodium ions occupy half of tetrahedral sites randomly, γ-$NaFeO_2$ is said to have almost the same structure as β-$NaFeO_2$, but the symmetry is raised to tetragonal from orthorhombic[60].

Na_xMnO_2

Na_xMnO_2 oxides are attractive due to the cost-effectiveness of the Na and Mn elements. Na_xMnO_2 ($x<0.5$) consists of alternating MnO_2 and Na sheets which exists in α and β polymorphic forms[62]. The layers are flat in the α-$NaMnO_2$ polymorph with monoclinic symmetry (*C2/m* space group) at low temperature[63] and corrugated (zigzag-like) in β-$NaMnO_2$ with orthorhombic symmetry (*Pmnm* space group) at high temperature[64] as shown in Figure 2.6[65]. The first study on Na-Mn-O ternary oxides for rechargeable sodium-ion batteries dates

back to the 1980s[49], which demonstrated reversibility of Na extraction/insertion from/into O'3-type α-$NaMnO_2$. Ma et al. reported that O'3-type α-$NaMnO_2$ exhibits a discharge capacity of 197 mAh g^{-1} in the voltage range 2.0-3.8 V at C/30 rate[66]. β-$NaMnO_2$ has a zigzag layered structure composed of two edge-sharing MnO_6 octahedra between which Na^+ ions occupy octahedral sites within two neighboring sheets[67]. Bruce et al. investigated β-$NaMnO_2$ with a high capacity of 190 mAh g^{-1} at a rate of C/20, along with a good rate capability of 141 mAh g^{-1} at a rate of C/2 and a good capacity retention of 100 mAh g^{-1} after 100 Na extraction/insertion cycles at a rate of 2 C. The collapse of the long-range structure at low Na content is expected to compromise the reversibility of the Na (de)intercalation reaction occurring upon charge and discharge of the cathode materials[68].

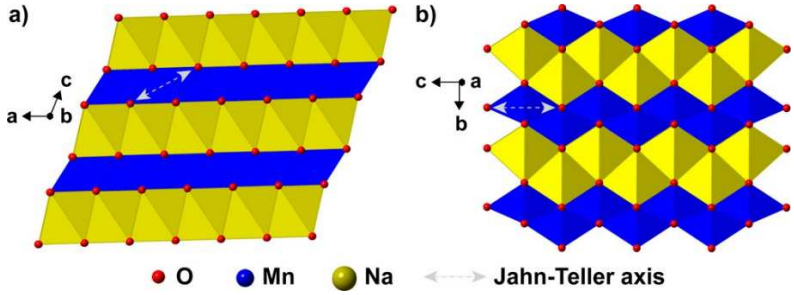

Figure 2.6 Experimental crystal structures of the two polymorphs of $NaMnO_2$: (a) monoclinic α-$NaMnO_2$ (*C*2/*m* space group); (b) orthorhombic β-$NaMnO_2$ (*Pmnm* space group). Adapted from reference[65].

The research group of C. Delams was the first to discover that sodium reacts with MnO_2 to form Na_xMnO_2 compounds, whose structure is determined by the Na content and preparation temperature[63]. When the Na-to-Mn ratio is 1, the O3 structure is stabilized, but due to the presence of Jahn-Teller Mn^{3+} ions, the layered structure is monoclinically distorted. The P2 structure becomes stable as the Na-to-Mn ratio decreases from 1.0 to 0.7[69]. Mn^{4+} ions are used to compensate for the Na deficiency, resulting in the formula $Na_xMn_x^{3+}Mn_{1-x}^{4+}O_2$. Despite the orthorhombic distortion of P2 caused by the high Mn^{3+} content, a monoclinic distortion of P2 has also been observed[70]. At a temperature of 1000 °C, orthorhombic P'2-$Na_{0.7}MnO_2$ (with space group: *Cmcm*) remains stable, while under controlled synthesis condition nondistorted

hexagonal P2-Na_xMnO_2 (with space group: *P6₃/mmc*) can be also produced[71]. The electrode performance of P2-Na_xMnO_2 has been the most intensively studied with a reversible capacity of over 150 mAh g^{-1} [51]. The rapid capacity fade of Na_xMnO_2 is due to the strong Jahn-Teller effect of Mn^{3+} and/or the instability of the structure in the presence of moisture. Substituting for a quantity of Mn^{3+} might stabilize the structure of P2-type Na_xMnO_2 and enhance its cycle life at the same time[72].

$Na_x[Mn_yFe_{1-y}]O_2$ and derivatives

P2-Na_xMnO_2 has promising electrode performance based on its reversible capacity, but its average operating voltage with a Mn^{3+}/Mn^{4+} redox couple is limited to less than 3 V *vs* metallic Na. O3-$NaFeO_2$ has a much higher average operating voltage (3.2-3.3 V) than P2-Na_xMnO_2, despite having a narrower reversible range due to irreversible iron migration. P2-Na_xFeO_2 is considered a possible candidate for high-capacity and high-energy electrode materials, but previous attempts failed because Fe^{4+} cannot be stabilized in the oxide-ion framework under ambient conditions.

To stabilize the P2 phase, manganese ions were substituted for ion, which results in the successful synthesis of P2-$Na_{2/3}[Fe_{1/2}Mn_{1/2}]O_2$. The SXRD pattern, an SEM image, and a schematic illustration of $Na_{2/3}[Fe_{1/2}Mn_{1/2}]O_2$ are shown in Figure 2.7a. Symbols A, B and C in the schematics represent the three different oxygen layers described by the ABC notation. Fe/Mn-based layered oxides are attractive due to their natural abundance, environmental safety, high operating voltage of Fe^{3+}/Fe^{4+}, and large specific capacity of Mn^{3+}/Mn^{4+}[73]. P2-$Na_{2/3}[Fe_{1/2}Mn_{1/2}]O_2$ can deliver a capacity of 190 mAh g^{-1} in the voltage window of 1.5-4.2 V based on the Fe^{3+}/Fe^{4+} and Mn^{3+}/Mn^{4+} redox couples, as shown in Figure 2.7b. This results in an estimated energy density of 520 Wh kg^{-1} versus Na metal. Additionally, it is possible to prepare O3-type $Na[Fe_{1/2}Mn_{1/2}]O_2$ by changing the ratio of sodium/(iron and manganese), which is demonstrated in Figure 2.7c with an SXRD pattern, SEM image, and schematic

illustration. The electrode performance of O3-$Na[Fe_{1/2}Mn_{1/2}]O_2$ in the Na cell is shown in Figure 2.7d, where large polarization (>1 V) is observed when the Na cell is cycled in the voltage range of 1.5-4.2 V. In comparison with the O3 phase, the P2 phase shows a larger reversible capacity, which is clearly illustrated in Figure 2.7e[73]. A first-cycle discharge capacity of 190 mAh g^{-1} corresponds to 72% of the theoretical capacity assuming a single-electron redox process of a Me^{3+}/Me^{4+} (Me = $Fe_{1/2}Mn_{1/2}$) redox couple, which shows the superior electrode performance of the P2 phase compared to the O3 phase. The physical origin of stability and differences in Na ion diffusion between the P2 and O3 phases could be attributed to the electrostatic interactions within oxide layers that dictate the behavior of these phases[74].

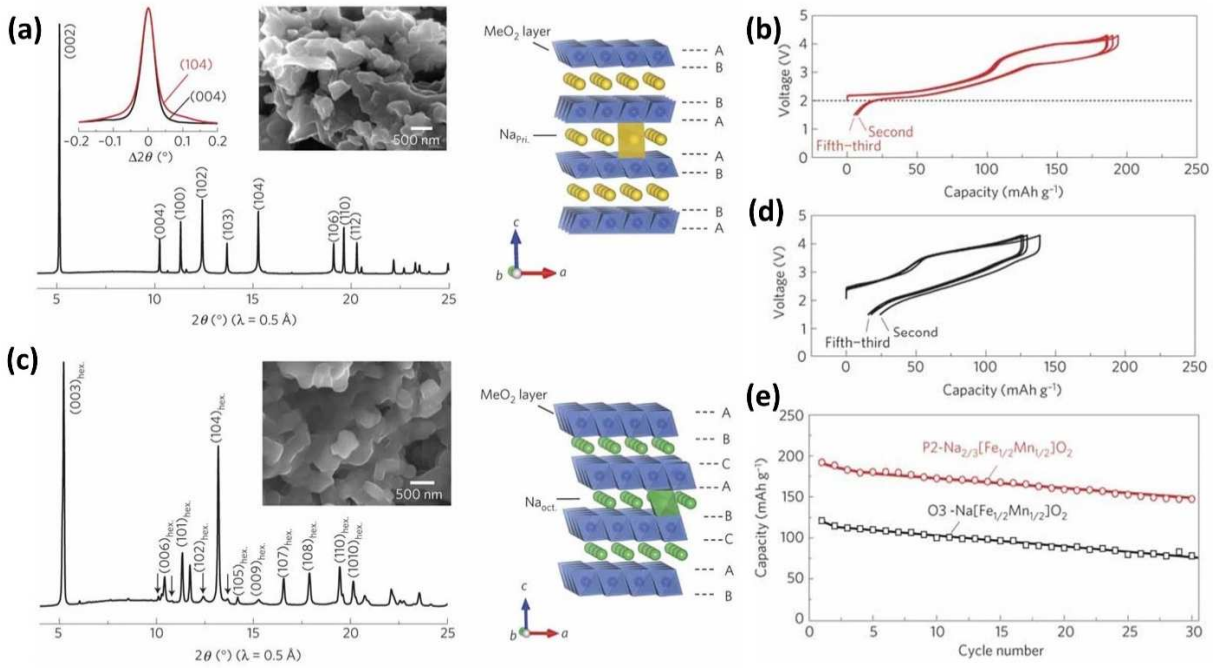

Figure 2.7 SXRD patterns, SEM images and schematic illustrations of (a) $Na_{2/3}[Fe_{1/2}Mn_{1/2}]O_2$ (a = 2.9335(3) and c = 11.224(1) Å), (b) $Na[Fe_{1/2}Mn_{1/2}]O_2$ ($a_{hex.}$ = 2.9590(6) and $c_{hex.}$ = 16.522(2) Å). Symbols A, B and C in the schematics represent the three different oxygen layers described by the ABC notation; Galvanostatic charge/discharge (oxidation/reduction) curves for (c) $Na/Na_{2/3}[Fe_{1/2}Mn_{1/2}]O_2$ and (d) $Na/Na[Fe_{1/2}Mn_{1/2}]O_2$; (e) Comparison of the discharge capacity retention of the sodium cells. Adapted from reference[73].

During the desodiation and resodiation process of the P2-$Na_{2/3}[Fe_{1/2}Mn_{1/2}]O_2$ material over the 1.5-4.2 V (*vs* Na) window, the *in situ* synchrotron X-ray powder diffraction data reveal a

sequence of phase transitions from $P6_3/mmc$ (P2-type at the open-circuit voltage) to $P6_3$ (OP4-type when fully charged) to $P6_3/mmc$ (P2-type at 3.4-2.0 V) to *Cmcm* (P'2-type at 2.0-1.5 V) as shown in Figure 2.8[75]. At voltages exceeding 4.0 V during deintercalation, P2-$Na_{2/3}[Fe_{1/2}Mn_{1/2}]O_2$ undergoes a phase transformation to the disordered OP4 phase. P2-$Na_{2/3}Fe_{0.4}Mn_{0.6}O_2$[76] and P2-$Na_{2/3}Mn_{2/3}Fe_{1/3}O_2$[77] with higher Mn content can maintain the P2-type phase until the discharged state, while also coexisting with the distorted orthorhombic P'2 phase and at least two other phases at high potentials. To improve the cycle life and rate capability, two approaches have been used to alleviate the issues. The first approach is chemical modification which can suppress structural transitions. Shin et. al studied the Fe L_3-edge, Mn L_3-edge, Na K-edge, and O K-edge spectra of the pristine and charged states of the $Na_{0.67}Fe_{0.25}Mn_{0.75}O_2$ (FMO) and $Na_{0.67}Li_{0.2}Fe_{0.2}Mn_{0.6}O_2$ (LFMO)[78] primary particles obtained using STXM. The spectral analysis revealed that the average oxidation states of the Fe, Mn, and Na ions were +3, +3.5 ~ +3.9, and +1, respectively. When comparing LFMO particles to FMO samples, the Fe L_3-edge and O K-edge spectra showed fewer changes between the pristine and charged states in LFMO, indicating better structural stability. The Na ions in LFMO show a more homogeneous arrangement when the material is sodiated, and the Mn ions exhibited a more homogeneous oxidation state of approximately +4 when the material is desodiated. Moreover, in LFMO particles, the change in the oxidation numbers of Na and Mn ions was increased, indicating a larger electrochemical capacity and improved performance in comparison to FMO[78]. Zhou et. al prepared a series of $Na_{0.67}(Fe_{0.5}Mn_{0.5})_{1-x}Mg_xO_2$ (x=0.05, 0.1, 0.15, 0.2, 0.25) cathode materials for SIBs and systematically investigated the effects of Mg-substitution on the morphology, structure and electrochemical performance for the cathodes. The electrochemical performance of the optimized P2/O3 biphasic NMg-0.15 is excellent in comparison to other samples. It has an initial discharge capacity of 98.1 mAh g^{-1} at 1 C and exhibits outstanding capacity retention of 96% after 50 cycles. The cathode also maintains a capacity retention of 88% after 100 cycles. These results indicate that the integrated P2 and O3

phase is an effective approach to enhance the electrochemical performance of SIBs[79]. Yang et. al proposed Ti-doping strategy to suppress the Jahn-Teller distortion and the related P2-P'2 transition in $Na_{2/3}Mn_{2/3}Fe_{1/3}O_2$ cathode material. The inclusion of Ti doping in $Na_{2/3}Fe_{1/3}Mn_{0.57}Ti_{0.1}O_2$ results in a single P2 phase throughout the charge-discharge process by strongly inhibiting the P2-P2' phase transition at low discharge voltage, thus improving the cycling stability of the electrode by reducing mechanical strain[77]. Another approach is to limit the high voltage cutoff to 4.1 V to avoid the P2-OP4 transition. Ti-doping in P2-phase $Na_{2/3}Mn_{0.8}Fe_{0.1}Ti_{0.1}O_2$ results in improved electrochemical performance and fast Na^+ mobility in the interlayer space, which results in a specific capacity of 99.40 mAh g^{-1} at 1 C, and a capacity retention of 87.7% is achieved from the second to the 300th cycle within the voltage range of 2.0-4.0 V[80].

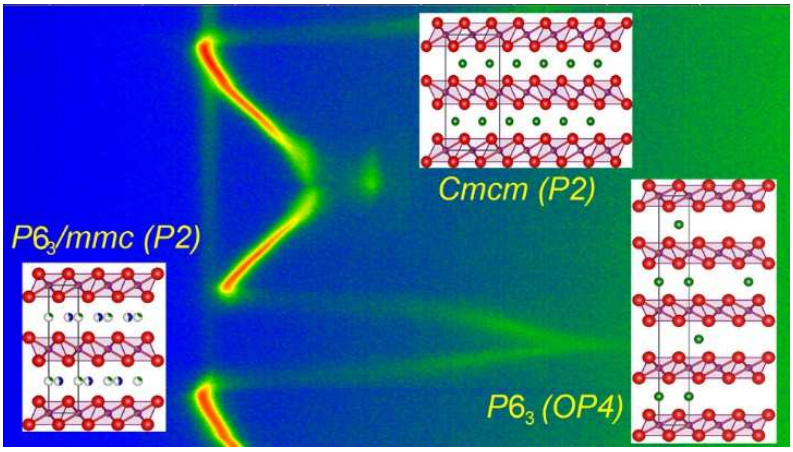

Figure 2.8 Contour plots of operando SXRPD data for $Na_{2/3}[Fe_{1/2}Mn_{1/2}]O_2$. Adapted from reference[75].

2.4.1.2 Other 3d transition-metal oxides with layered structures and derivatives

Na_xCoO_2 and derivatives

Layered Na_xCoO_2 has been extensively researched as a host for sodium insertion[14], with the O3, O'3, and P3 layer structures forming in the temperature range of 400-600 ^oC. The P2 structure is only stable at temperatures above 700 ^oC in an oxygen atmosphere and involves the conversion of the P3 phase, which includes the rotation of CoO_6 octahedra and Co-O bond

breakage. The de-/resodiation voltage profile, operating voltage, and phase transition are similar for both the O3 and P3 phases. Regardless of the stacking sequence of CoO_2 layers, the different phases of Na_xCoO_2 exhibit several voltage plateaus. A high reversible capacity of 140 mAh g^{-1} is observed for the O3 phase, while the P3 and P2 phases exhibit capacities of 130 mAh g^{-1} and 120 mAh g^{-1}, respectively[16].

The O3 phase of Na_xCoO_2 has octahedral sites that share three edges with CoO_6 octahedra, whereas the P2 phase has two distinct prismatic sites: edge shared and face shared prismatic sites with the CoO_6 octahedra[16]. The P2 phase exhibits behavior similar to the O3 and P3 phases in the voltage range of 2.7-3.5 V, but the phase transition is more complex below 2.7 V compared to the O3 and P3 phases due to the difference in Na^+ ordering[17]. The first demonstration of SIBs was conducted in 1988 using P2- and P3-type Na_xCoO_2 as positive electrode materials and a composite of poly(p-phenylene) and Na_xPb as the negative electrode. The capacity retention for P2-$Na_{0.7}CoO_2$ was over 80% for 300 cycles, while P3- $Na_{0.7}CoO_2$ exhibited a retention of approximately 60% for over 250 cycles. The higher capacity of the P2 phase may be due to its higher crystallinity compared to the P3 material produced at low temperatures[81]. Ca-doped $Na_{5/8}Ca_{1/24}CoO_2$ can suppress phase separation in P2-type Na_xCoO_2, resulting in improved cycling performance. However, large Ca^{2+} ions occupy the Na layers, which would hinder the transportation of Na^+ during cycling[82]. It is unlikely that Na_xCoO_2 can reach a performance comparable to that of $LiCoO_2$ in LIBs. Suppressing the ordering of Na^+/vacancies and reducing the content of the expensive Co element in P2-Na_xCoO_2 by cations substitution are key issues to be solved[83].

Na_xNiO_2 and derivatives

Research on Na_xNiO_2, a layered oxide material, has focused on its potential use as a cathode material in SIBs. There are two stable polymorphs of Na_xNiO_2, which include a low-temperature O3-type and a high-temperature rhombohedral phase. The Ni-O layer in $NaNiO_2$

shares edges between NiO_6 octahedra, and the Jahn-Teller active Ni^{3+} ions are located in elongated octahedra in a manner similar to α-$NaFeO_2$. During the initial electrochemical process, $NaNiO_2$ exhibited a significant loss of capacity that cannot be recovered. However, when the upper voltage cutoff was adjusted to 3.75 V, the capacity retention improved significantly, reaching up to 94% (115 mAh g^{-1}) after 20 cycles[84]. The O'3 type structure of $NaNiO_2$ with the *C*2/*m* space group is synthesized in an oxidative environment due to the divalent Ni starting material.

Na_xNiO_2 has demonstrated potential as a cathode material for SIBs with high specific capacity and good cycling stability. Nevertheless, there are certain obstacles to address, including poor rate performance and capacity fading, which hinder its widespread practical application. Ti-doped rhombohedral O3-$NaNi_{0.5}Ti_{0.5}O_2$ has shown remarkable cyclic stability at moderate conditions, delivering a reversible capacity of 121 mAh g^{-1} at 20 mA g^{-1} based on the redox couple of Ni^{2+}/Ni^{3+} at an average operating potential of 3.1 V (vs Na^+/Na)[85]. Komaba and colleagues used $Li[Ni_{0.5}Mn_{0.5}]O_2$ as a model to prepare $Na[Ni_{0.5}Mn_{0.5}]O_2$ with an O3-type layered structure that undergoes redox reactions of $Ni^{2+/4+}$. Due to the presence of tetravalent Mn, $Na[Ni_{0.5}Mn_{0.5}]O_2$ contains Ni^{2+} and had a high discharge capacity of 185 mAh g^{-1} in a voltage range of 2.5-4.5 V. The upper voltage cutoff was optimized to 3.8 V, resulting in a capacity of over 100 mAh g^{-1} after 20 cycles. Unlike $NaNiO_2$, the O3 → O'3 → P3 → P'3 phase transition was highly reversible between 2.5-3.8 V[86]. Hwang et al. introduced a cathode material with a radially aligned hierarchical columnar structure in spherical particles with varied chemical composition from the center ($Na[Ni_{0.75}Co_{0.02}Mn_{0.23}]O_2$) to the outer part ($Na[Ni_{0.58}Co_{0.06}Mn_{0.36}]O_2$) of the structure. The cathode material delivers a discharge capacity of 157 mAh g^{-1} (15 mA g^{-1}) based on the electrochemical reaction of $Ni^{2+}/^{3+}/^{4+}$. The cathode material shows a capacity retention of 80% (125 mAh g^{-1}) over 300 cycles when combined with a hard carbon anode and has a rate capability of 132.6 mAh g^{-1} (1500 mA g^{-1}, 10 C-rate), which

exhibits good temperature performance even at -20 °C. The unique chemistry of the cathode material enables the Ni redox reaction and minimizes the surface area contacting corrosive electrolyte, which contributes to the observed results[87].

2.4.2 Metal hexacyanoferrates

Metal hexacyanoferrates, also known as Prussian blue analogs (PBAs), which include $A_2M[Fe(CN)_6]$ (where A is an alkali metal such as Li^+, Na^+, K^+ and M is a transition metal such as Fe, Co, Mn, Ni, or Cu), possess a highly stable open framework structure, numerous redox-active sites, and robust structural stability[88]. PBAs have large ionic channels and interstices in the lattice, which make them one of the few host materials capable of accommodating larger alkali cations like Na^+ and K^+ ions for fast and efficient reversible insertion reactions. This structural feature has led to intensive research on PBAs compounds as a new alternative and low-cost cathode for practical battery application[89].

2.4.3 Polyanionic compounds

Compared to other types of cathode materials, polyanion-type electrode materials are attractive and often seen as potential sodium-host electrodes in the future because of their strong covalent bonding framework that offers high structural and thermal stability, as well as improved cycling durability and safety[90]. Polyanionic cathodes can have various structures, including olivine-type in the *Pnma* space group (Figure 2.9a)[91], pyrophosphate-type structures with triclinic space group P1 (Figure 2.9b)[92], NASICON-structured in the *Pnma* space group (Figure 2.9c)[93], and mixed polyanionic compounds in the orthorhombic *Pn21a* space group (Figure 2.9d)[94]. NASICON-type cathode materials, including $Na_xM_y(XO_4)_n$ (where X = S, P, Si, As, Mo, and W; M = transition metal), have tetrahedral anion units $(XO_4)^{n-}$ and its derivatives $(X_mO_{3m+1})^{n-}$. These materials have strong covalent bonds in MO_x polyhedral, and they exhibit excellent performance for sodium storage in batteries[95]. The redox potentials of different transition metal species in NASICON-structured $Na_xM_y(XO_4)_n$ systems are shown in Figure 2.9e. One

advantage of polyanionic cathodes is their ability to accommodate different types of cations, which allows for the development of multi-valent and multi-cation cathodes. This can lead to higher energy densities and improved performance. However, there are still some challenges that need to be addressed, such as low electronic conductivity and poor rate performance, before polyanionic cathodes can be widely used in commercial sodium-ion batteries.

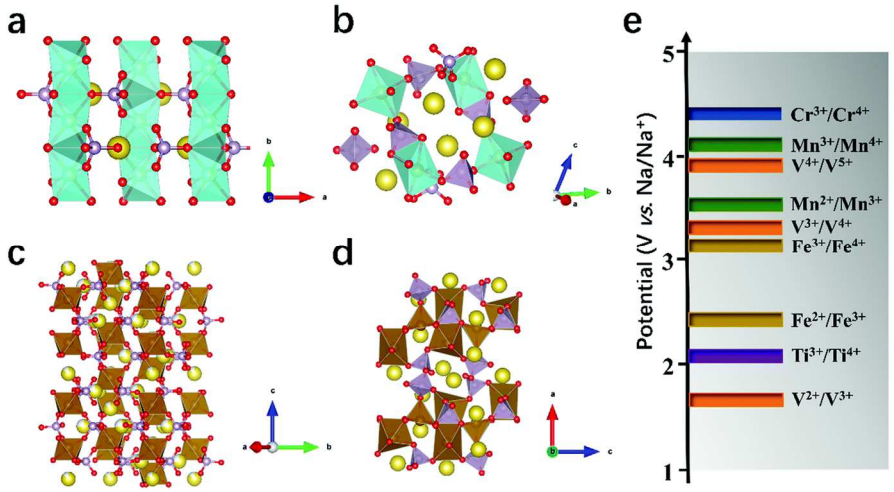

Figure 2.9 Crystal structures of representative polyanion-type compounds, which are mainly based on phosphate units: (a) olivine $NaFePO_4$ in the Pnma space group, (b) $Na_2FeP_2O_7$ in the triclinic structure in space group P1, (c) NASICON-structured $Na_3Fe_2(PO_4)_3$ in the R-3c space group, (d) mixed polyanionic compound $Na_4Fe_3(PO_4)_2(P_2O_7)$ in the orthorhombic Pn21a space group where the $(P_2O_7)^{4-}$ dimers generate large channels for sodium ion diffusion. (e) The redox potentials of different transition metal species in NASICON-structured $Na_xM_y(XO_4)_n$ systems. Adapted from reference[90].

2.5 Thesis overview

This PhD thesis consists of five chapters. **Chapter 1** is the motivation and outline of the whole work. **Chapter 2** gives a brief description of sodium batteries and cathode materials. **Chapter 3** introduces the materials synthesis, materials characterization, and electrochemical measurement. **Chapter 4** presents the details on the results, discussion, and conclusions of research. **Chapter 5** summarizes and recommends the strategy for further studies.

Chapter 3 Material Synthesis and Characterization Techniques

3.1 Material synthesis

3.1.1 Introduction of solid-state reaction

Solid-state reaction which occurs in solid-state at high temperatures has been widely used due to its simplicity, low cost, and potential for large-scale production. In solid-state reactions, the reactants are positioned in close proximity to enable the formation of new chemical bonds. The reactants are typically in the form of powder or crystals that are intimately mixed and heated to high temperatures, which allows for the diffusion of atoms and the formation of new phases. The solid-state reaction process relies on heat conduction and thermal convection of the material from a heat source and requires long annealing times to complete the reaction and slow crystallization process. The products of solid-state reactions are typically solid materials that exhibit unique properties and structures due to the specific conditions under which they were formed. In addition, ball milling is necessary to synthesize the desired particle morphology and crystal size[96].

3.1.2 Synthesis of different cathodes

Synthesis of P2-NMFO and O3-$NaMn_{1/2}Fe_{1/2}O_2$

P2-NMFO and O3-$NaMn_{1/2}Fe_{1/2}O_2$ were synthesized by a solid-state method from stoichiometric amounts of Na_2O_2 (Alfa Aesar, 99%), Mn_2O_3 (Sigma-Aldrich, 99%), and Fe_2O_3 (Sigma-Aldrich, 99%) with molar ratios of 2/3:1/2:1/2 and 2/3:1/2:1/2, respectively. For P2-NMFO, the mixture was pelletized and heated at 850 °C for 12 h. For O3-$NaMn_{1/2}Fe_{1/2}O_2$, the mixture was pelletized and heated at 650 °C for 12 h. Due to the sensitivity against ambient atmosphere, samples then were quenched to room temperature and stored in an Ar-filled glove box until use.

Synthesis of P2-, P2/P3- and P3-NMFTO

NMFTO were synthesized by a solid-state method from stoichiometric amounts of Na_2O_2 (Alfa Aesar, 99%), Mn_2O_3 (Sigma-Aldrich, 99%), Fe_2O_3 (Sigma-Aldrich, 99%) and TiO_2 (Sigma-Aldrich, 99.8%) with molar ratios of 2/3:7/12:1/3:1/12, respectively. For P2-, P2/P3- and P3-NMFTO, the mixture was pelletized and heated at 650 °C, 750 °C and 850 °C for 12 h.

Synthesis of $Na_{2/3}Mn_{1/3}Fe_{1/3}Ti_{1/3}O_2$ ($NM_{1/3}F_{1/3}T_{1/3}O$)

$Na_{2/3}Mn_{1/3}Fe_{1/3}Ti_{1/3}O_2$ ($NM_{1/3}F_{1/3}T_{1/3}O$) were synthesized by a solid-state method from stoichiometric amounts of Na_2O_2 (Alfa Aesar, 99%), Mn_2O_3 (Sigma-Aldrich, 99%), Fe_2O_3 (Sigma-Aldrich, 99%) and TiO_2 (Sigma-Aldrich, 99.8%) with molar ratios of 2/3:1/3:1/3:1/3, respectively. The mixture was pelletized and heated at 850 °C for 12 h.

Synthesis of $Na_{2/3}Mn_{1/2}Fe_{1/3}Ti_{1/6}O_2$ ($NM_{1/2}F_{1/3}T_{1/6}O$)

$Na_{2/3}Mn_{1/2}Fe_{5/6}Ti_{1/6}O_2$ ($NM_{1/2}F_{1/3}T_{1/6}O$) were synthesized by a solid-state method from stoichiometric amounts of Na_2O_2 (Alfa Aesar, 99%), Mn_2O_3 (Sigma-Aldrich, 99%), Fe_2O_3 (Sigma-Aldrich, 99%) and TiO_2 (Sigma-Aldrich, 99.8%) with molar ratios of 2/3:1/2:5/6:1/6, respectively. The mixture was pelletized and heated at 850 °C for 12 h.

Synthesis of $Na_{2/3}Mn_{1/3}Fe_{1/2}Ti_{1/6}O_2$ ($NM_{1/3}F_{1/2}T_{1/6}O$)

$Na_{2/3}Mn_{5/6}Fe_{1/2}Ti_{1/6}O_2$ ($NM_{1/3}F_{1/2}T_{1/6}O$) were synthesized by a solid-state method from stoichiometric amounts of Na_2O_2 (Alfa Aesar, 99%), Mn_2O_3 (Sigma-Aldrich, 99%), Fe_2O_3 (Sigma-Aldrich, 99%) and TiO_2 (Sigma-Aldrich, 99.8%) with molar ratios of 2/3:5/6:1/2:1/6, respectively. The mixture was pelletized and heated at 850 °C for 12 h.

Synthesis of $Na_{2/3}Mn_{1/2}Fe_{5/12}Ti_{1/12}O_2$ ($NM_{1/2}F_{5/12}T_{1/12}O$)

$Na_{2/3}Mn_{1/2}Fe_{5/12}Ti_{1/12}O_2$ ($NM_{1/2}F_{5/12}T_{1/12}O$) were synthesized by a solid-state method from stoichiometric amounts of Na_2O_2 (Alfa Aesar, 99%), Mn_2O_3 (Sigma-Aldrich, 99%), Fe_2O_3 (Sigma-Aldrich, 99%) and TiO_2 (Sigma-Aldrich, 99.8%) with molar ratios of 2/3:1/2:5/12:1/12, respectively. The mixture was pelletized and heated at 850 °C for 12 h.

Synthesis of $Na_{2/3}Mn_{5/12}Fe_{1/2}Ti_{1/12}O_2$ ($NM_{5/12}F_{1/2}T_{1/12}O$)

$Na_{2/3}Mn_{5/12}Fe_{1/2}Ti_{1/12}O_2$ ($NM_{5/12}F_{1/2}T_{1/12}O$) were synthesized by a solid-state method from stoichiometric amounts of Na_2O_2 (Alfa Aesar, 99%), Mn_2O_3 (Sigma-Aldrich, 99%), Fe_2O_3 (Sigma-Aldrich, 99%) and TiO_2 (Sigma-Aldrich, 99.8%) with molar ratios of 2/3:5/12:1/2:1/12, respectively. The mixture was pelletized and heated at 850 °C for 12 h.

Synthesis of $Na_{2/3}Mn_{1/3}Fe_{7/12}Ti_{1/12}O_2$ ($NM_{1/3}F_{7/12}T_{1/12}O$)

$Na_{2/3}Mn_{1/3}Fe_{7/12}Ti_{1/12}O_2$ ($NM_{1/3}F_{7/12}T_{1/12}O$) were synthesized by a solid-state method from stoichiometric amounts of Na_2O_2 (Alfa Aesar, 99%), Mn_2O_3 (Sigma-Aldrich, 99%), Fe_2O_3 (Sigma-Aldrich, 99%) and TiO_2 (Sigma-Aldrich, 99.8%) with molar ratios of 2/3:1/3:7/12:1/12, respectively. The mixture was pelletized and heated at 850 °C for 12 h.

3.2 Materials characterization

3.2.1 Powder diffraction

***Ex situ* powder diffraction.** The powder X-ray diffractometer (XRD) was used to measure the phase composition and crystal structure of the materials. The measurement was performed using a STOE STADI/P diffractometer with Mo K α1 radiation (50 kV, 40 mA, λ= 0.709320 Å) in the range 5-50°. The XRD data of materials were analyzed using Rietveld refinement using the FullProf software package[97].

***In situ* synchrotron radiation diffraction (SRD).** High-resolution *in situ* SRD experiments on the cathode materials were performed with a photon energy of 60 keV (λ = 0.2072 Å) at beamline P02.1, storage ring PETRA III at Deutsches Elektronensynchrotron (DESY) in Hamburg, Germany[98]. The diffraction patterns were acquired using a VAREX XRD 4343CT (150×150 μm^2 pixel size, 2880 x 2880-pixel area) 2D position-sensitive detector. The exposure time for each pattern was 60 s. CR2032 coin cells with glass windows (diameter = 6 mm) were used. Data calibration (LaB6, NIST-660c) and integration were done using the DawnSci software[99].

Structure model. All the structural and electron density distribution models were obtained from refinement results and visualized using VESTA software[100].

3.2.2 Microscopic observation

SEM-EDX. The morphology of samples was observed using a scanning electron microscope (SEM, Zeiss Merlin) with an acceleration voltage of 10 keV. The coupled energy-dispersive X-ray (EDX) analysis was conducted using a Quantax 400 system from Bruker.

STEM. The crystal structure and elemental distribution of the samples were measured by high-resolution transmission electron microscopy (HRTEM) and high-angle annular dark-field scanning transmission electron microscopy (HAADF-STEM)-energy dispersive X-ray spectroscopy (EDS) mapping measurements at 300 kV acceleration voltage using a Thermo-Fisher Themis-Z equipped with double aberration correctors (TEM and STEM).

3.2.3 Spectroscopic techniques

***In situ* XAS.** *In situ* X-ray Absorption Spectroscopy (XAS) on cathode electrodes was performed during charging/discharging using a cell design similar to that used for the *in situ* SRD studies. XAS was performed at beamline P65 at PETRA-III, Germany. Electrochemical cycling was conducted in 2032-type coin cells with a 6 mm Kapton window in the voltage range of 1.5 - 4.3V. XAS spectra at the Fe K-edge (7112 eV) and Mn K-edge (6539 eV) were acquired with a beam size of 0.3×1.5 mm^2. All XAS spectra were analyzed and processed utilizing the ATHENA software package[101].

sXAS. Soft X-ray Absorption Spectroscopy (sXAS) measurements were carried out at the beamline WERA of the KARA synchrotron in Karlsruhe, Germany. The measurements were conducted on electrodes which were charged or discharged to different voltages. Data were acquired in the inverse fluorescence yield (iFY) and fluorescence yield (FY) mode using silicon photodiodes.

^{57}Fe Mössbauer spectroscopy. *In situ* Mössbauer spectroscopy was performed at room temperature with a constant-acceleration spectrometer in transmission mode and a ^{57}Fe (Rh) source. All isomer shifts were given relative to that of α-Fe metal. Synthesis of the cathode materials was done with Fe_2O_3 enriched in ^{57}Fe (95%). The cathodes powder together with the conductive carbon (C65) and poly (vinylidene difluoride) (PVDF) binder in a weight ratio of 8:1:1 were mixed in 1-methyl-2-pyrrolidinone (NMP) and cast onto Al foil. After drying at 80 °C, electrode tapes were cut into discs of 19 mm diameter, pressed with a hydraulic press at 6 tons, and dried at 120 °C under vacuum overnight. Electrochemical cycling was conducted in special cells with a 14 mm Kapton window in the voltage range of 1.5 - 4.3 V.

^{23}Na NMR spectroscopy. ^{23}Na magic-angle spinning nuclear magnetic resonance (MAS NMR) experiments were performed at a Bruker Avance neo 200 MHz spectrometer at a field of 4.7 T using a 1.3 mm MAS probe at spinning speed of 55 kHz. The recycle delay was set to 1 s, and the Larmor frequency was 52.9 MHz. ^{23}Na MAS NMR spectra were acquired using a rotor-synchronized Hahn-echo pulse sequence (90°-τ-180°-τ-acquisition) with a 90° pulse length of 0.8 μs. Spectral intensities were normalized with respect to sample mass and number of scans.

3.3 Electrochemical characterization of electrodes

Construction of coin cells. The electrochemical performance of the prepared materials was investigated by galvanostatic cycling in a coin-type half-cell (CR2025) setup *vs*. sodium metal anode. To prepare electrodes, the obtained cathodes powder together with conductive carbon (C65) and poly (vinylidene difluoride) (PVDF) binder were mixed in a weight ratio of 8:1:1 in 1-methyl-2-pyrrolidinone (NMP) and cast onto Al foil. After drying at 80 °C, electrode tapes were cut into discs of 12 mm diameter, pressed with a hydraulic press at 6 tons, and dried at 120 °C under vacuum overnight. Metallic sodium foil served as counter electrode, and the electrodes were measured in 2032-type two-electrode coin cells. One molar $NaClO_4$ in a 1:1

(*v*:*v*) ratio of ethylene carbonate/diethyl carbonate (EC/DMC) with 5 wt% fluoroethylene carbonate (FEC) was used as electrolyte.

Galvanostatic tests. The half-cell measurements were conducted at various C-rates between 1.5 and 4.3 V (vs. Na^+/Na) at 25 °C. All electrochemical measurements were controlled by a Bio-logic VMP3 potentiostat.

GITT. For the galvanostatic intermittent titration technique (GITT) measurement, short current pulses were applied to the cell with a resting time of 5 h inserted after each pulse. The diffusion coefficient could be calculated based on the following equation[102]:

$$D_s = \frac{4}{\pi}\left(\frac{IV_m}{FS}\right)^2\left(\frac{dU°/dy}{dV/d\sqrt{t}}\right)^2, t \ll R^2/D_s$$

where I is the current value for the short pulse, F is Faraday's constant, V_m is the molar volume of the active materials, S is the composite electrode active area, U° is the open-circuit potential at the end of each rest period, y is the state of charge (SoC), V and t are the voltage and time during pulse periods, and R is the diffusion length. Instead of giving the absolute diffusion coefficients, DsS^2/V_m^2 was calculated since the molar volume (V_m) and active surface area (S) are difficult to obtain. Two additional GITT experiments were conducted on identical samples to increase the reliability of the conclusions.

Chapter 4 Results and Discussion

4.1 Exploring the structural and electrochemical behavior of Ti substituted $Na_{2/3}Mn_xFe_yTi_{1-x-y}O_2$

4.1.1 Introduction

An attractive alternative to lithium-ion batteries for future sustainable society are sodium-ion batteries made from earth-abundant and non-toxic metal elements such as Na, Fe, and Mn[103]. During electrochemical cycling, α-$NaFeO_2$ demonstrates a stable and consistent voltage profile. However, it experiences an irreversible structural transformation above a voltage of 3.6 V. This transformation leads to a rapid decline in capacity after only a few cycles, resulting in diminished performance[61]. Mn-containing layered oxides have notable drawbacks, such as the potential for Mn ions to dissolve in the electrolyte and the propensity for rapid capacity deterioration. This deterioration is attributed to structural strain caused by the introduction of Jahn-Teller high-spin Mn^{3+} ($t_{2g}^3e_g^1$) during electrochemical cycling, despite the initial high reversible capacity and low polarization[49, 66]. Extensive research has been conducted on $Na_xFe_{1-y}Mn_yO_2$ ($x \leqslant 1$; $0 \leqslant y \leqslant 1$) due to their environmentally friendly nature, low cost associated with abundant metal elements, and their ability to deliver a high reversible capacity. The study of Komaba's group shows that P2-$Na_{2/3}Fe_{1/2}Mn_{1/2}O_2$ has the ability to deliver 190 mAh g^{-1} of reversible capacity in sodium cells with the Fe^{3+}/Fe^{4+} redox[73]. Mortemard et.al conducted a comparison of the electrochemical properties of the P2- and O3-$Na_xFe_{1/2}Mn_{1/2}O_2$ phases with other materials which confirmed that the P2 phase demonstrates a significantly higher reversible capacity[104].

Cobalt- and nickel-free cathode materials are desirable for developing low-cost SIBs. The properties of P2/O3-$Na_{0.8}Li_{0.2}Fe_{0.2}Mn_{0.6}O_2$ and its behavior at different states of charge/discharge are reported by Yang et.al, where an initial reversible capacity of 174 mAh g^{-}

[1] is delivered with a retention of 82% dominated by Fe^{3+}/Fe^{4+} redox activity along with contributions from oxygen and partial $Mn^{3+/4+}$ redox contributions[105]. Zhou et. al developed a novel hybrid phase P2/O3-$Na_{0.67}Fe_{0.5}Mn_{0.46}Mg_{0.04}O_2$ cathode material for sodium batteries, which delivered 182 mAh g^{-1} at 0.2 C[106]. Chen et. al created a P2/O3 biphasic $Na_{0.67}Li_{0.11}Fe_{0.36}Mn_{0.36}Ti_{0.17}O_2$ through high-proportion Li^+ and Ti^{4+} co-substitution in TM layers, which delivers an ultrahigh capacity of ~ 235 mAh g^{-1} with great cycling stability (85% capacity retention for 100 cycles)[107]. The substitution of Ti does not alter the phase structure, while it does lead to the formation of robust Mn-O-Ti-O-Fe bonds within the transition metal (TM) layers, significantly improving the stability of the overall structure. However, this enhancement comes at the cost of reduced capacity due to the inactivity of Ti[108]. In the present study, the electrochemical performance and structural stability of partially substituted iron- and manganese- based sodium cathode materials are investigated. We synthesized P2- and O3-$Na_xFe_{1/2}Mn_{1/2}O_2$ and studied the structural changes occurring during cycling by *in situ* synchrotron X-ray powder diffraction (*in situ* SRPD). Moreover, we explored the structure and electrochemical properties of layered cathode materials with different Fe, Mn, and Ti ratios in TM layers.

4.1.2 Results and discussion

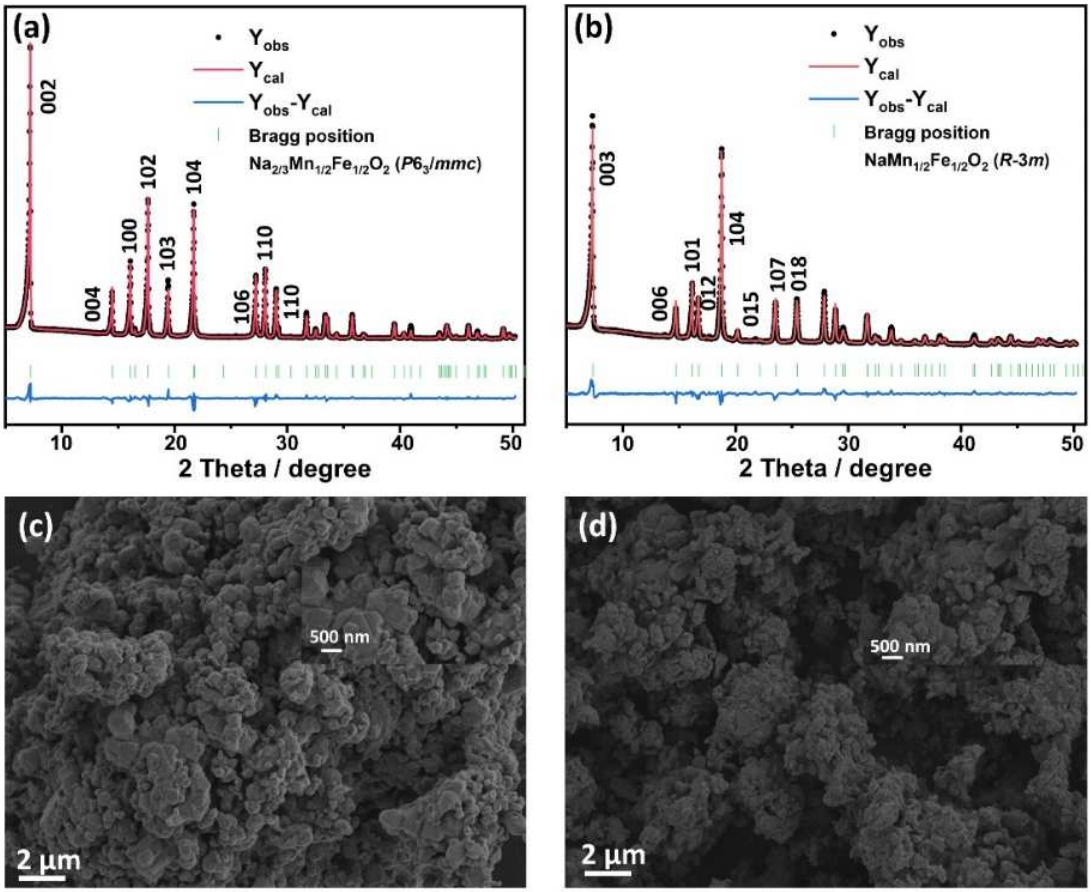

Figure 4.1 Rietveld refinement based on XRD diffraction of cathode materials (a) P2-NMFO and (b) O3-$NaFe_{1/2}Mn_{1/2}O_2$. Morphology of pristine (c) P2-NMFO and (d) $NaFe_{1/2}Mn_{1/2}O_2$.

SXRD patterns for P2-NMFO and O3-$NaFe_{1/2}Mn_{1/2}O_2$ are shown in Figure 4.1a and 4.2b, which were synthesized as single phases. The hexagonal lattice with space group $P6_3/mmc$ was identified as the structure for all diffraction lines of P2-NMFO. The unit cell parameters of P2-NMFO are $a = b = 2.9241(7)$ Å, $c = 11.2491(52)$ Å. In contrast, major diffraction lines of O3-$NaFe_{1/2}Mn_{1/2}O_2$ are assigned to a rhombohedral lattice with space group R-3m with $a = b = 2.9433(2)$ Å, $c = 16.5933(3)$ Å. Figures 4.1c and 4.1d reveal that the primary particle size of P2- NMFO and O3-$NaFe_{1/2}Mn_{1/2}O_2$ is around 500 nm. The particles are agglomerated, resulting in several micrometer-sized secondary particles. There is no significant difference in morphology between the two samples.

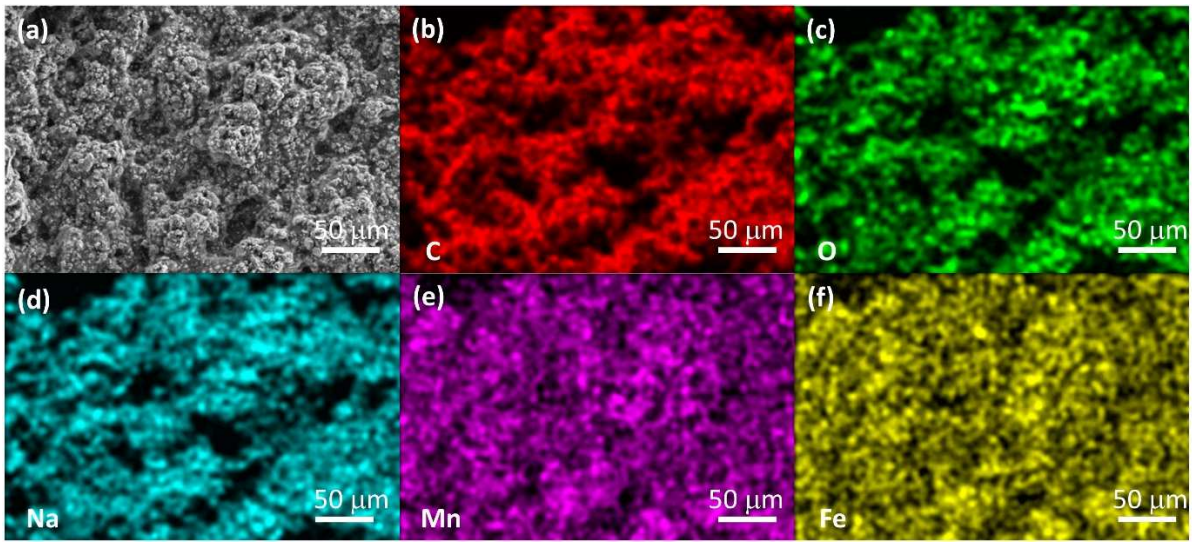

Figure 4.2 (a) EDX elemental mapping analysis of P2-NMFO electrode. (a) SEM electronic image, (b-f) the distribution map of C, O, Na, Mn, and Fe elements.

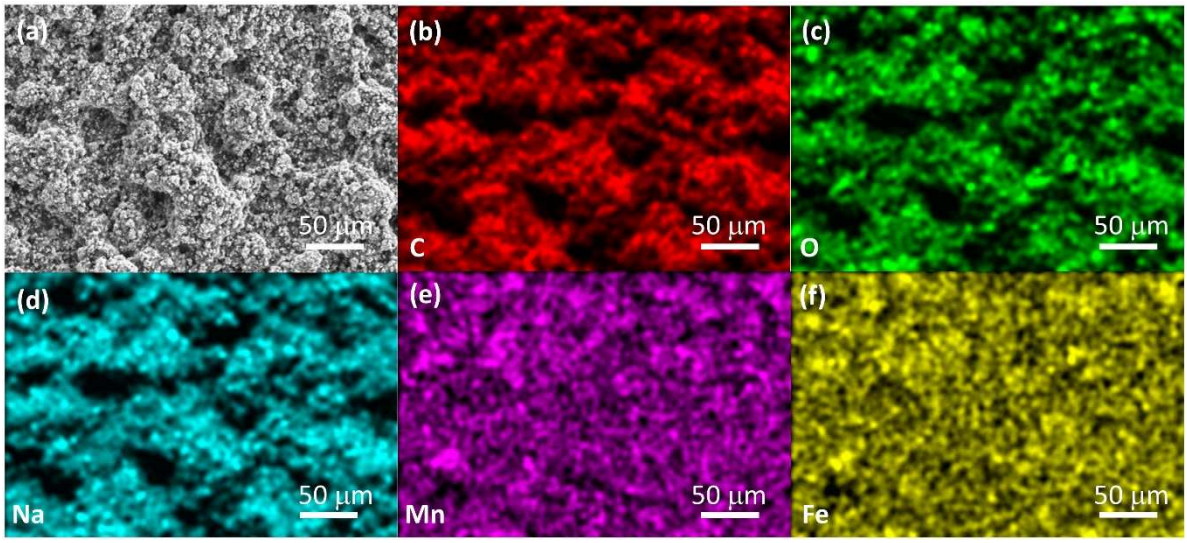

Figure 4.3 (a) EDX elemental mapping analysis of O3-$NaFe_{1/2}Mn_{1/2}O_2$ electrode. (a) SEM electronic image, (b-f) the distribution map of C, O, Na, Mn, and Fe elements.

Figures 4.2 and 4.3 show the energy-dispersive X-ray (EDX) elemental mapping assessing the elemental composition of P2-NMFO and O3-$NaFe_{1/2}Mn_{1/2}O_2$ electrodes. There is no significant difference in morphology between P2-NMFO and O3-$NaFe_{1/2}Mn_{1/2}O_2$ electrodes which was observed by SEM electronic images Figure 4.2a and 4.3a. The elemental analysis mapping as shown in Figure 4.2 (b-f) and 4.3 (b-f) disclosed the homogenous distribution of C, O, Na, Mn and Fe throughout the P2-NMFO and O3-$NaFe_{1/2}Mn_{1/2}O_2$ electrodes.

The electrochemical performance of P2-NMFO and O3-$NaFe_{1/2}Mn_{1/2}O_2$ cells was evaluated in the voltage range of 1.5-4.3 V. The first two charge/discharge curves of P2-NMFO (Figure 4.4a) at 0.05 C exhibit a sloped region below 4.0 V and a plateau above 4.0 V. The cell shows a discharge capacity of 193 mAh g^{-1}. In the second cycle, the cell exhibits a decreased discharge capacity of ~185 mAh g^{-1} compared to that in the first cycle. The first charge/discharge curve of O3-$NaFe_{1/2}Mn_{1/2}O_2$ (Figure 4.4b) at 0.05 C shows a discharge capacity of 175 mAh g^{-1}. In the second cycle, the cell exhibits a decreased discharge capacity of ~170 mAh g^{-1} compared to that in the first cycle. The rate capabilities of P2-NMFO and O3-$NaFe_{1/2}Mn_{1/2}O_2$ are shown in Figure 4.4c and 4.4d. P2-NMFO delivers 42% of the reversible capacity at 1 C compared to the capacity at 0.1 C. O3-$NaFe_{1/2}Mn_{1/2}O_2$ delivers 43% reversible capacity which is similar to that of P2-NMFO. The comparison of the discharge capacity retention of P2-NMFO and O3-$NaFe_{1/2}Mn_{1/2}O_2$ is shown in Figure 4.4e. O3-$NaFe_{1/2}Mn_{1/2}O_2$ delivers 120-155 mAh g^{-1} of reversible capacity at 0.1 C in the voltage range of 1.5-4.3 V. The capacity retention of O3-$NaFe_{1/2}Mn_{1/2}O_2$ is 77% after 30 cycles. In comparison with the O3 phase, the P2 phase shows a better electrode performance, which delivers 145-170 mAh g^{-1} of reversible capacity. The capacity retention of P2-NMFO is 85% after 30 cycles.

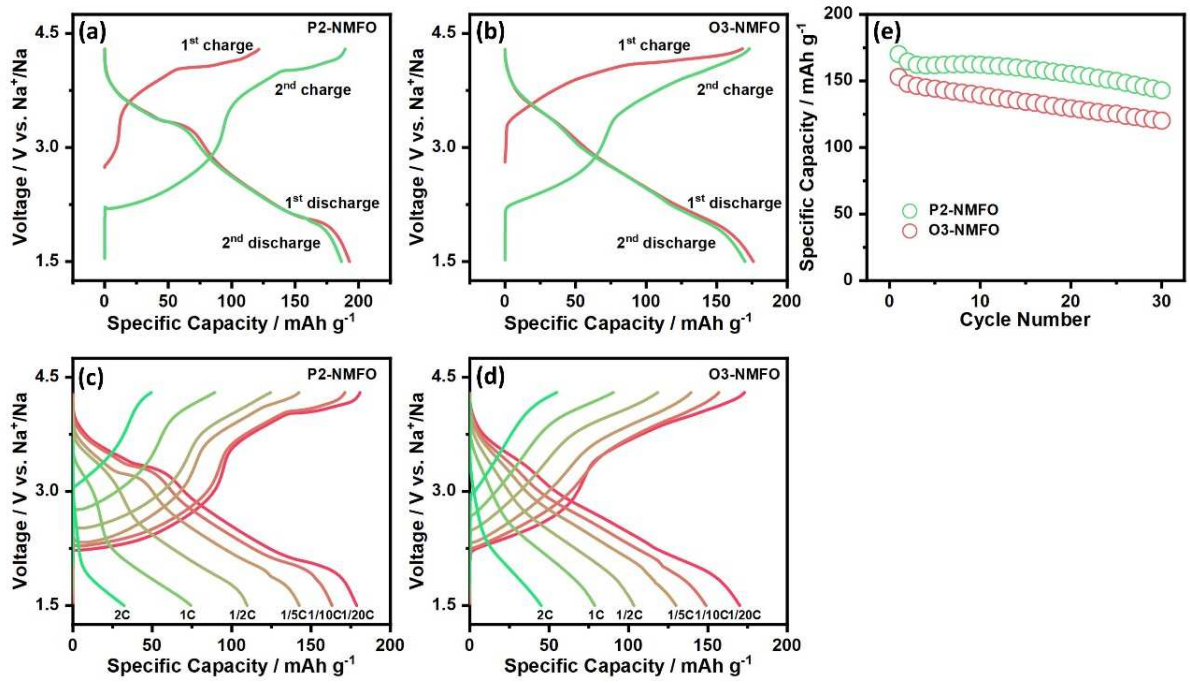

Figure 4.4 Cell voltage as a function of specific capacity of P2-NMFO for the first two cycles at 0.05C.(a) Na/NMFO and (b) Na/$NaFe_{1/2}Mn_{1/2}O_2$; Rate capability of (c) Na/NMFO and (d) Na/$NaFe_{1/2}Mn_{1/2}O_2$; (e) Comparison of the discharge capacity retentions of the sodium cells.

The electrochemical sodium extration/insertion mechanisms of P2-NMFO and O3-$NaFe_{1/2}Mn_{1/2}O_2$ were analyzed by SRD, as shown in Figure 4.5 and 4.7. The SRD patterns and contour maps for P2-NMFO acquired during the charging/discharging process at 0.1 C rate in the voltage range 1.5-4.3 V are shown in Figures 4.5a and 4.5b. From the open circuit voltage (OCV) to 4.1 V, the 002, 004, and 106 reflections of NFMO shifted to lower angles reflecting a gradual expansion of the interlayer spacing (Figure 4.5c). At the same time, the 100, 102, 110, and 112 reflections are shifted towards larger angles, revealing a contraction of the distances within the layer (Figure 4.5d). When the NMFO cathode is charged to voltages above 4.1 V, new reflections appear indicating the phase transition in this material, due to the gliding of $[Fe_{1/2}Mn_{1/2}]O_2$ slabs[109]. This phase transition is the transition from the P2 to the Z structure, as reported previously for P2-$Na_x[Fe_{1/2}Mn_{1/2}]O_2$[109]. Upon further charging, the reflections of P2 disappear due to the formation of the Z phase. This phase transition is reversibly achieved by the gliding of the TM slabs, which is attributed to the thermodynamic instability of unoccupied

prismatic sites. Rietveld refinements against the in situ SXRD patterns show that the lattice parameter a (Figure 4.5c) initially decreases, while the lattice parameter c (Figure 4.5d) increases which is in good agreement with previous results on P2-NMFO[73]. According to the contour maps and corresponding cell parameters, no phase change occurs for NMFO during the initial desodiation process up to ~4.1 V. In the following discharging to 3.1 V, the positive electrode changes back from the Z to the P2 phase. During further discharging to 1.9 V, a new orthorhombic phase P2' starts to appear because of the reduction of Mn^{4+} to Jahn-Teller distorted Mn^{3+}. Selected XRD diffraction patterns during charging/discharging of NMFO with different phases and the Rietveld refinement of P2'-NMFO are shown in Figure 4.6a and 4.6b.

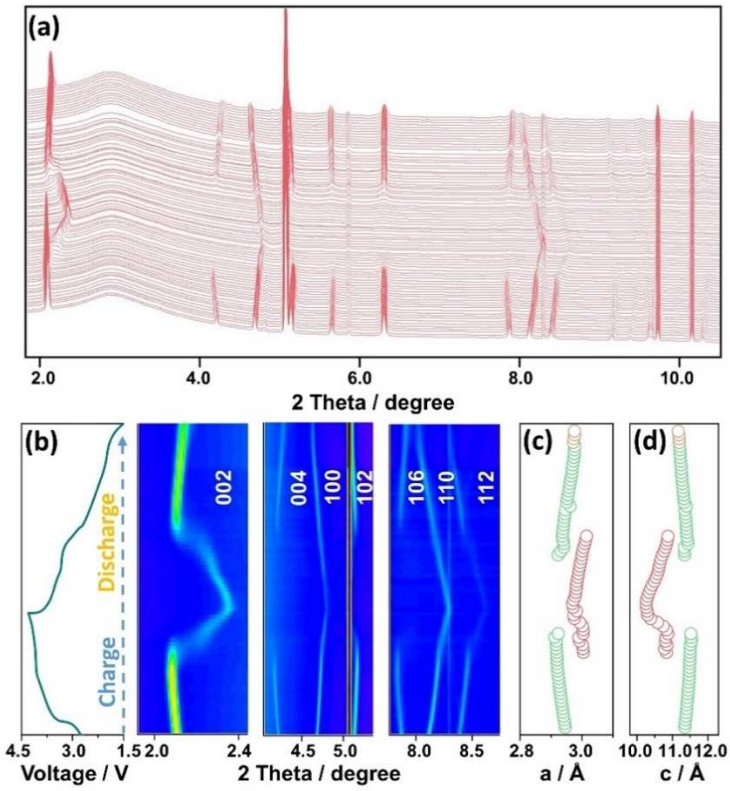

Figure 4.5 XRD patterns (a) and contour maps (b) of *in situ* synchrotron diffraction data collected during the first charge/discharge process and the corresponding voltage profiles on the left side and the changes of the lattice parameters on the right side (c, d) for P2-NMFO at 0.1C rate and over the voltage range 1.5-4.3 V. The lattice parameters of P2 phase are shown as green labels. The lattice parameters of Z phase are shown as green labels. The lattice parameters of P2' phase are shown as olive labels.

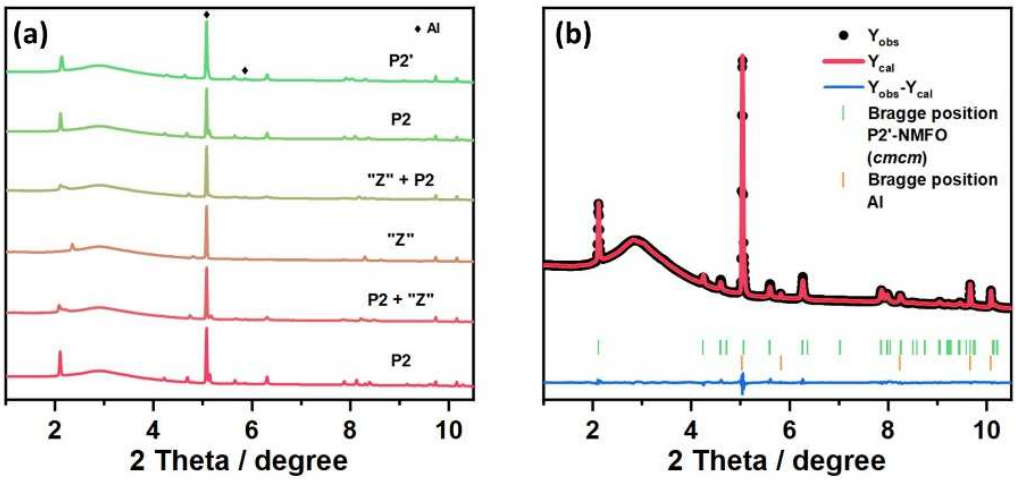

Figure 4.6 (a) Selected XRD patterns during charging/discharging with different phases; (b) Rietveld refinement based on the XRD diffraction pattern of P2'-NMFO which was obtained at the end of discharging of P2-NMFO.

SRD patterns and contour maps for O3-$NaFe_{1/2}Mn_{1/2}O_2$ during the charging/discharging process at 0.1C rate in the voltage range 1.5-4.3 V are shown in Figures 4.7a and 4.7b. Selected XRD patterns acquired during charging/discharging with different phases are shown in Figure 4.8, which illustrates the phase change of O3-$NaMn_{1/2}Fe_{1/2}O_2$ via the phases O3 → O3+P3 → "X" → O3+P3 → O3. From the open circuit voltage (OCV) to 3.5 V, the 002 and 006 reflections of O3-NFMO shifted to lower angles reflecting a gradual expansion of the interlayer spacing (Figure 4.7b). At the same time, the 101 and 104 reflections are shifted towards larger angles, revealing a contraction of the distances within the layer (Figure 4.7b). A biphasic region with the phases O3 and P3 appears during charging from 3.5 V to 3.75 V, as can be seen from the Rietveld refinement based on XRD diffraction, and the enlarged view of selected XRD patterns acquired during discharging is shown in Figures 4.9a and 4.9b. When the O3-NMFO cathode is charged to voltage above 3.75 V, the intensities of the 003 and 104 reflections is reduced because of the formation of the "X" which is causes by the gliding of TMO_2 slabs[110, 111]. This gliding continuous to the discharging period at 3 V. Upon further discharging to 2.25 V, the positive electrode changes back from the "X" phase to the biphasic O3+P3 region. The Rietveld refinement based on XRD diffraction and the enlarged view of selected XRD patterns acquired during discharging is shown in Figures 4.9c and 4.9d. This phase transition is reversibly

achieved by the gliding of the TM slabs, which is attributed to the thermodynamic instability of unoccupied prismatic sites. During further discharging to 1.5 V, the structure comes back to the O3 phase. The Rietveld refinement based on XRD diffraction and the enlarged of selected XRD patterns in the fully discharged state are shown in Figures 4.9e ang 4.9f.

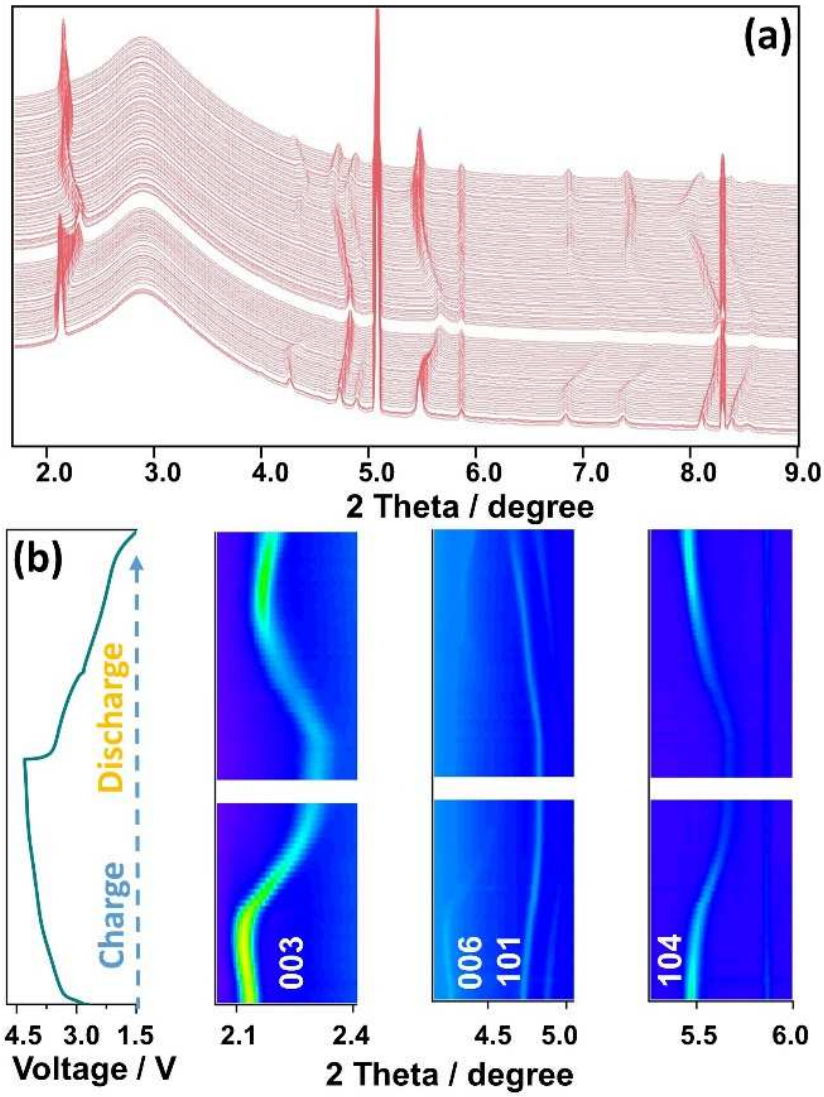

Figure 4.7 XRD patterns (a) and contour maps (b) of *in situ* synchrotron diffraction data collected during the first charge/discharge process for O3-$NaFe_{1/2}Mn_{1/2}O_2$ at 0.1 C rate over the range 1.5-4.3 V.

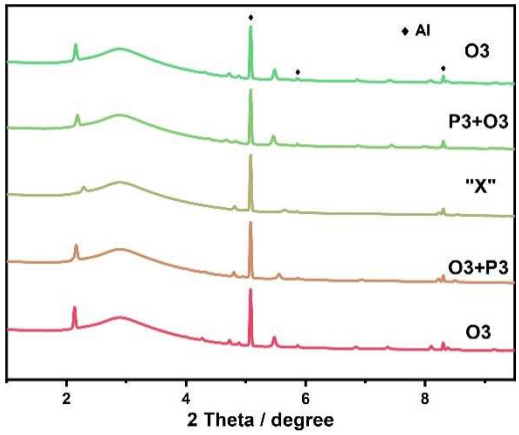

Figure 4.8 Selected XRD patterns of O3-$NaFe_{1/2}Mn_{1/2}O_2$ acquired during charging/discharging with different phases.

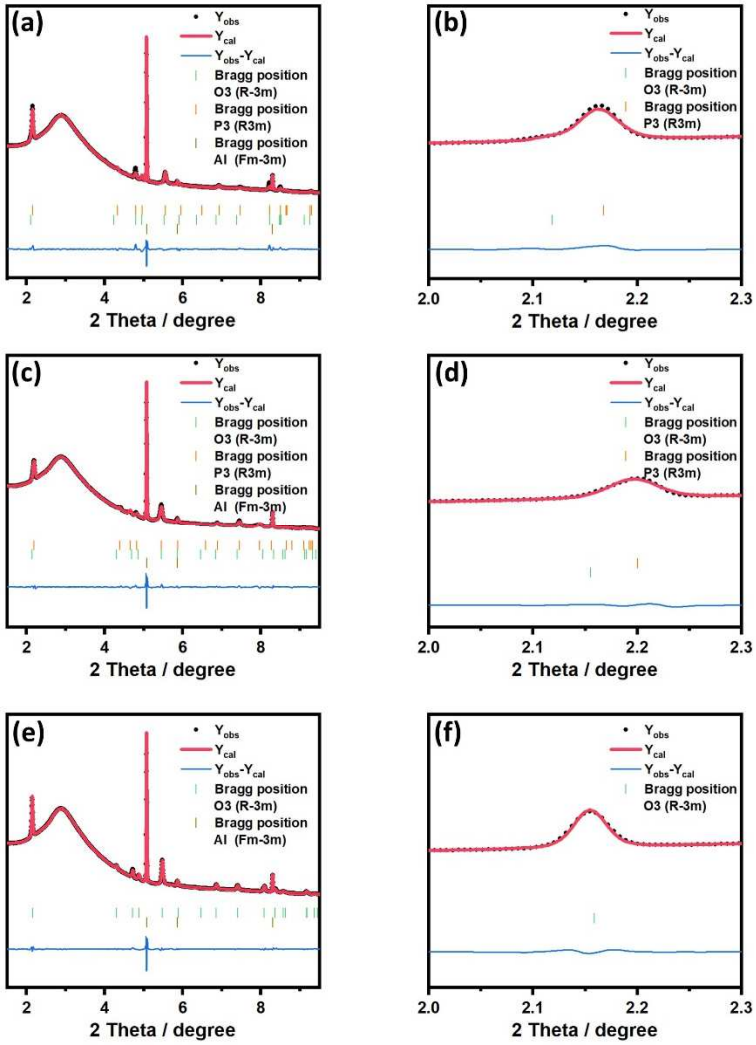

Figure 4.9 Rietveld refinement based on (a) XRD diffraction and (b) enlarged view of selected XRD pattern acquired during charging; Rietveld refinement based on (c) XRD diffraction and (d) enlarged view of selected XRD pattern acquired during discharging; Rietveld refinement based on (e) XRD diffraction and (f) enlarged view of the XRD pattern acquired in the fully discharged state.

Complex structural transitions exist in both P2-NMFO and O3-$NaMn_{1/2}Fe_{1/2}O_2$, which result in poor capacity retention. An effective strategy for suppressing these structural changes over a wider range of compositions has been demonstrated through the replacement of transition metal (TM) atoms in the TMO_2 slabs. The substitution of inactive Ti does not alter the crystallographic structure, while it does lead to the formation of robust Mn-O-Ti-O-Fe bonds within the TM layers, significantly improving the stability of the overall structure. Since a better electrochemical performance was observed for P2-NMFO compared to O3-$NaMn_{1/2}Fe_{1/2}O_2$, different ratios were synthesized for $Na_{2/3}Mn_xFe_yTi_{1-x-y}O_2$ to explore the structure and electrochemical properties of Mn- and Fe-based layered cathode materials.

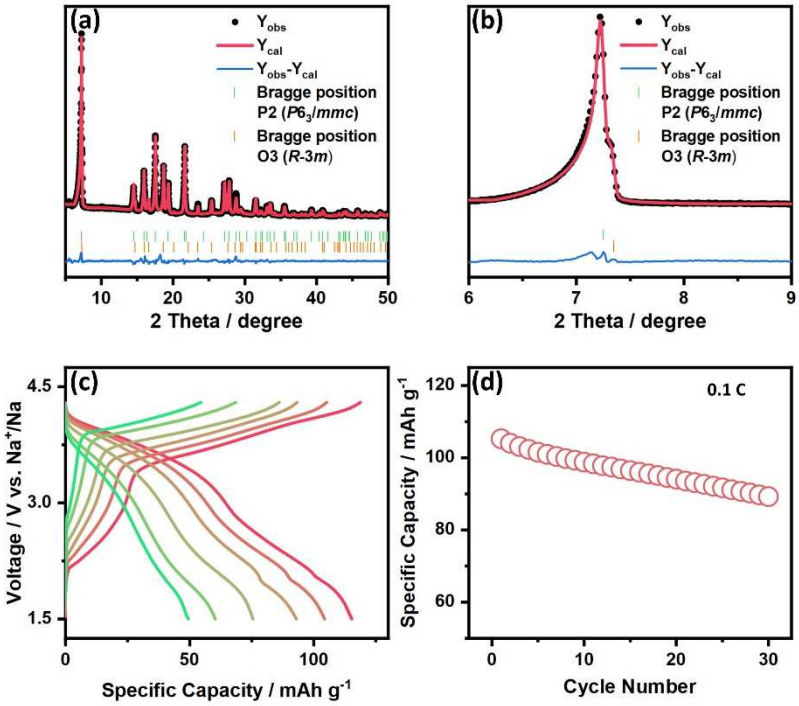

Figure 4.10 (a) Rietveld refinement based on XRD diffraction of $NM_{1/3}F_{1/3}T_{1/3}O$; (b) enlarged view of the XRD diffraction pattern; (c) Rate capability of $NM_{1/3}F_{1/3}T_{1/3}O$; (d) Discharge capacity retention of Na/$NM_{1/3}F_{1/3}T_{1/3}O$.

$NM_{1/3}F_{1/3}T_{1/3}O$ was synthesized with biphasic P2/O3 structure. Rietveld refinement based on the XRD pattern and an enlarged view of the XRD diffraction of $NM_{1/3}F_{1/3}T_{1/3}O$ are shown in Figures 4.10a and 4.10b. The electrochemical performance of cells with $NM_{1/3}F_{1/3}T_{1/3}O$ cathodes were evaluated in the voltage range of 1.5-4.3 V. $NM_{1/3}F_{1/3}T_{1/3}O$ sample delivers 60 mAh g^{-1} which is 58% of the reversible capacity at 1 C compared to the capacity at 0.1 C (Figure

4.10c). The capacity retention of $NM_{1/3}F_{1/3}T_{1/3}O$ is 85% after 30 cycles (Figure 4.10d). However, the capacity is just 115 mAh g^{-1} even at 0.05 C due to the inactivity of Ti. To synthesized cathodes with high capacity, reducing the amount of Ti in the substitution process should be considered. $NM_{1/2}F_{1/3}T_{1/6}O$ was synthesized with P2 phase and $NM_{1/3}F_{1/2}T_{1/6}O$ was synthesized with biphasic P2/O3 composition. Rietveld refinement based on the XRD patterns and an enlarged view of the XRD pattern of $NM_{1/2}F_{1/3}T_{1/6}O$ are shown in Figures 4.11a and 4.11b. The rate capacity of $NM_{1/3}F_{1/2}T_{1/6}O$ is shown in Figure 4.11e. This material delivers 150 mAh g^{-1} at 0.1 C and 58% of the reversible capacity at 1 C compared to the capacity at 0.1C. The capacity retention of $NM_{1/2}F_{1/3}T_{1/6}O$ is 76% after 30 cycles (Figure 4.11f). For $NM_{1/3}F_{1/2}T_{1/6}O$, Rietveld refinement based on XRD and an enlarged view of the XRD pattern are shown in Figures 4.11c and 4.11d. The rate capability of $NM_{1/2}F_{1/3}T_{1/6}O$ is shown in Figure 4.11g. This material delivers 134 mAh g^{-1} at 0.1 C and 47% of the reversible capacity is obtained at 1 C compared to the capacity at 0.1 C. The capacity retention of $NM_{1/3}F_{1/2}T_{1/6}O$ is 79% after 30 cycles (Figure 4.11h).

When comparing $NM_{1/2}F_{1/3}T_{1/6}O$ and $NM_{1/3}F_{1/2}T_{1/6}O$ to $NM_{1/3}F_{1/3}T_{1/3}O$, the capacities are increased due to the smaller amount of substituted Ti. However, the capacities of $NM_{1/2}F_{1/3}T_{1/6}O$ and $NM_{1/3}F_{1/2}T_{1/6}O$ are still lower than that of P2-NMFO at the same rate. To explore the electrochemical performance of cathodes with less Ti content, $Na_{2/3}Mn_{1/2}Fe_{5/12}Ti_{1/12}O_2$ ($NM_{1/2}F_{5/12}T_{1/12}O$), $Na_{2/3}Mn_{5/12}Fe_{1/2}Ti_{1/12}O_2$ ($NM_{5/12}F_{1/2}T_{1/12}O$), $Na_{2/3}Mn_{7/12}Fe_{1/3}Ti_{1/12}O_2$ ($NM_{7/12}F_{1/3}T_{1/12}O$), and $Na_{2/3}Mn_{1/3}Fe_{7/12}Ti_{1/12}O_2$ ($NM_{1/3}F_{7/12}T_{1/12}O$) were synthesized.

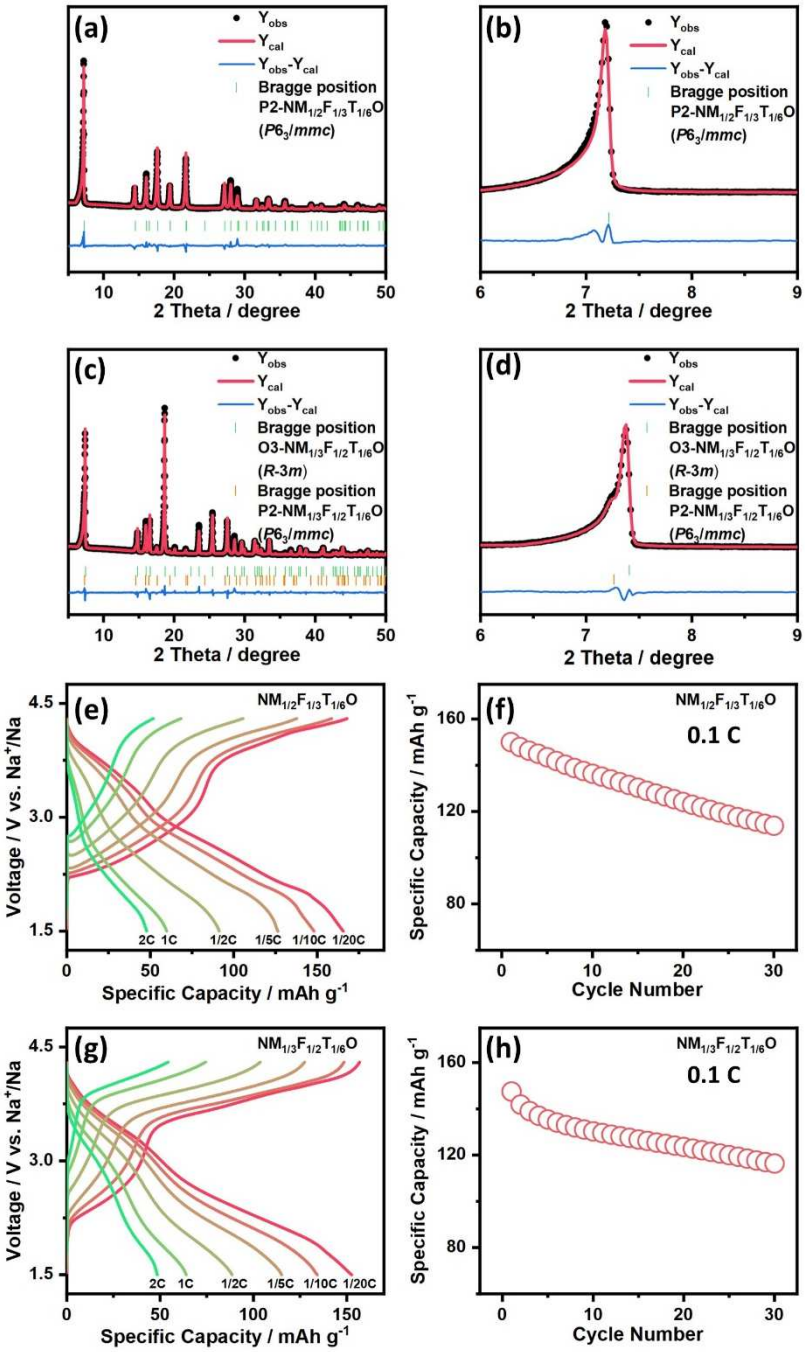

Figure 4.11 (a) Rietveld refinement based on XRD and (b) enlarged view of the XRD pattern of $NM_{1/2}F_{1/3}T_{1/6}O$; (c) Rietveld refinement based on XRD and (d) enlarged view of the XRD pattern of $NM_{1/3}F_{1/2}T_{1/6}O$; Rate capability of (e) $NM_{1/2}F_{1/3}T_{1/6}O$ and (g) $NM_{1/3}F_{1/2}T_{1/6}O$; Capacity retention of (f) Na/$NM_{1/2}F_{1/3}T_{1/6}O$ and (h) Na/ $NM_{1/3}F_{1/2}T_{1/6}O$.

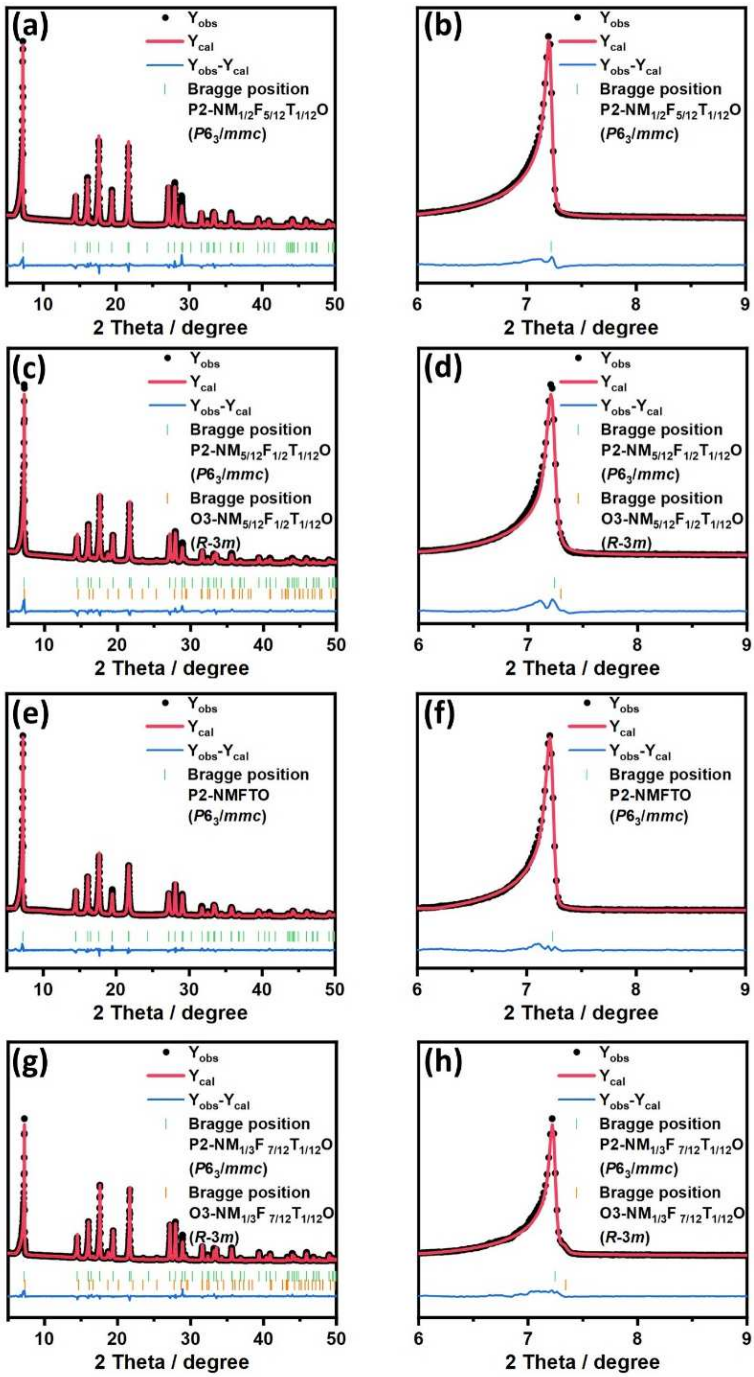

Figure 4.12 (a) Rietveld refinement based on XRD and (b) enlarged view of $NM_{1/2}F_{5/12}T_{1/12}O$; (c) Rietveld refinement based on XRD and (d) enlarged view of $NM_{5/12}F_{1/2}T_{1/12}O$; (e) Rietveld refinement and (f) enlarged view of NMFTO; (g) Rietveld refinement and (h) enlarged view of $NM_{1/3}F_{7/12}T_{1/12}O$.

$NM_{1/2}F_{5/12}T_{1/12}O$ and NMFTO were synthesized as single P2 phase. The Rietveld refinement based on XRD pattern and an enlarged view of the XRD pattern of $NM_{1/2}F_{5/12}T_{1/12}O$ are shown in Figures 4.12a and 4.12b. The same is shown for NMFTO in Figures 4.12c and 4.12d. $NM_{7/12}F_{1/3}T_{1/12}O$ and $NM_{1/3}F_{7/12}T_{1/12}O$ were synthesized as P2/O3 biphasic materials. Rietveld

refinement and an enlarged view of the XRD pattern are shown in Figures 4.12e and 4.12f. The same is shown for $NM_{1/3}F_{7/12}T_{1/12}O$ in Figures 4.12g and 4.12h. The rate capabilities of $NM_{1/2}F_{5/12}T_{1/12}O$, $NM_{5/12}F_{1/2}T_{1/12}O$, NMFTO, and $NM_{1/3}F_{7/12}T_{1/12}O$ are shown in Figures 4.13a-d. $NM_{1/2}F_{5/12}T_{1/12}O$ delivers 173 mAh g^{-1} at 0.1 C and 58% of this is retained at 1 C. The capacity retention of $NM_{1/2}F_{5/12}T_{1/12}O$ is 80% after 30 cycles as shown in Figure 4.13e. $NM_{5/12}F_{1/2}T_{12}O$ delivers 158 mAh g^{-1} at 0.1 C and 50% of this is retained at 1 C. The capacity retention of $NM_{1/2}F_{5/12}T_{1/12}O$ is 78% after 30 cycles, see Figure 4.13f. NMFTO delivers 171 mAh g^{-1} at 0.1 C and 64% of this capacity is retained at 1 C. The rate capacity retention of $NM_{1/2}F_{5/12}T_{1/12}O$ is 90% after 30 cycles (Figure 4.13g). $NM_{1/3}F_{7/12}T_{1/12}O$ delivers 164 mAh g^{-1} at 0.1 C and 56% of this at 1 C. The capacity retention of $NM_{1/2}F_{5/12}T_{1/12}O$ is 79% after 30 cycles (Figure 4.13h).

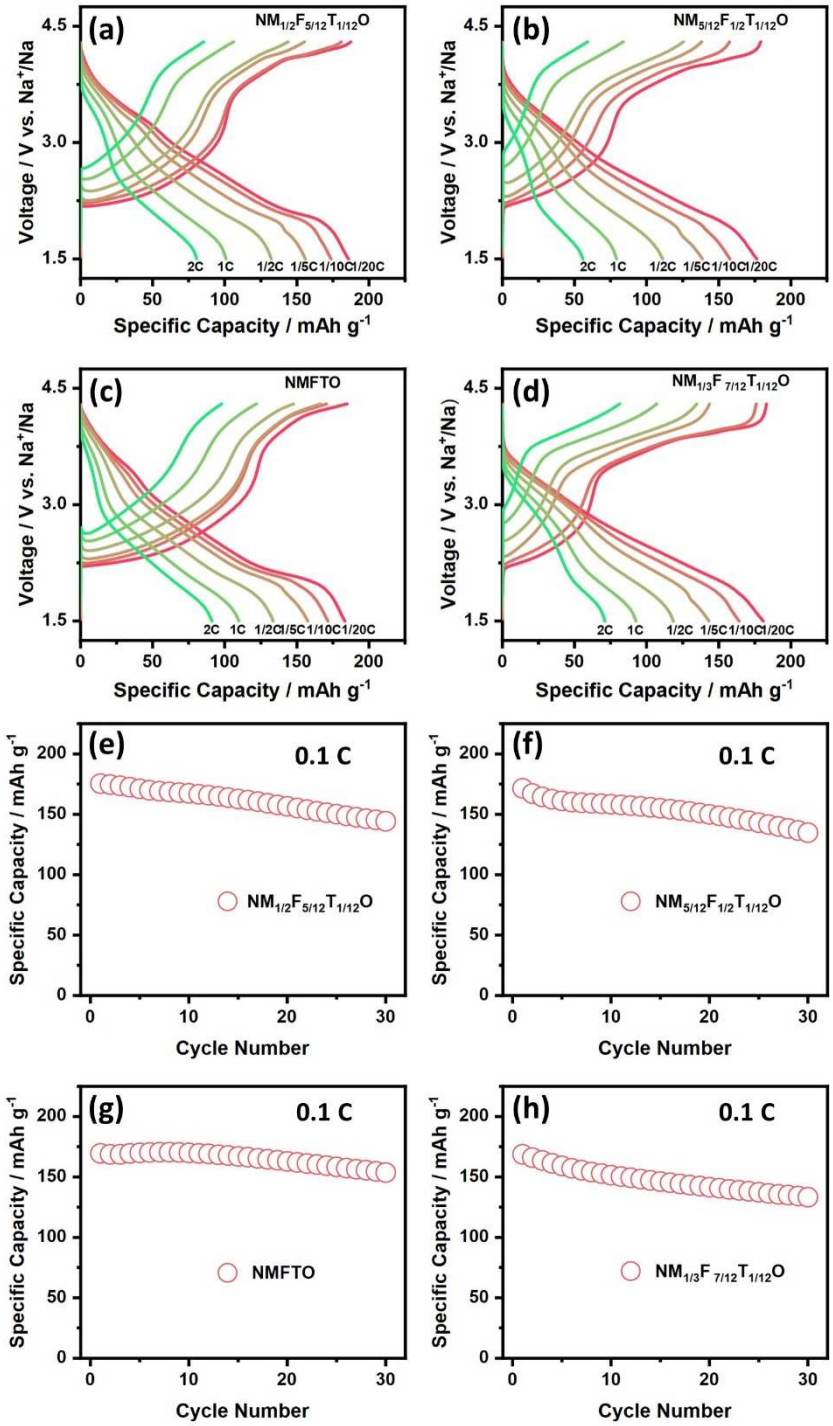

Figure 4.13 Rate capability of (a) $NM_{1/2}F_{5/12}T_{1/12}O$, (b) $NM_{5/12}F_{1/2}T_{1/12}O$, (c) NMFTO and (d) $NM_{1/3}F_{7/12}T_{1/12}O$; Discharge capacity retention of (e) $NM_{1/2}F_{5/12}T_{1/12}O$, (f) $NM_{5/12}F_{1/2}T_{1/12}O$, (g) NMFTO and (h) $NM_{1/3}F_{7/12}T_{1/12}O$.

Table 4.1 Detailed structural information of cathode materials obtained from the Rietveld refinements.

		a (Å)	b (Å)	c (Å)	V (Å^3)
$NaMn_{1/2}Fe_{1/2}O_2$	O3	2.9433(2)	2.9433(2)	16.5933(19)	124.491(16)
NMFO	P2	2.9241(7)	2.9241(7)	11.2491(52)	83.298(6)
$NM_{1/3}F_{1/3}T_{1/3}O_2$	P2 (75%)	2.9454(33)	2.9454(33)	11.2108(24)	84.228(62)
	O3 (25%)	2.9601(33)	2.9601(33)	16.5957(84)	125.972(46)
$NM_{1/2}F_{1/3}T_{1/6}O_2$	P2	2.9264(26)	2.9264(26)	11.2719(100)	83.600(88)
$NM_{1/3}F_{1/2}T_{1/6}O_2$	P2 (9%)	2.9461(33)	2.9461(33)	11.1497(44)	84.219(68)
	O3 (91%)	2.9757(28)	2.9757(28)	16.4706(54)	125.583(7)
$NM_{1/2}F_{5/12}T_{1/12}O_2$	P2	2.9257(15)	2.9257(15)	11.2556(57)	83.437(74)
$NM_{5/12}F_{1/2}T_{1/12}O_2$	P2 (94%)	2.9310(25)	2.9310(25)	11.2062(98)	83.821(25)
	O3 (6%)	2.9336(33)	2.9336(33)	16.8461(19)	125.707(21)
$NMFTO_2$	P2	2.9191(1)	2.9191(1)	11.2369(10)	82.9236(10)
$NM_{1/3}F_{7/12}T_{1/12}O_2$	P2 (93%)	2.9366(10)	2.9366(10)	11.2282(40)	83.754(25)
	O3 (7%)	2.9507(15)	2.9507(15)	16.6452(97)	125.312(17)

Table 4.1 shows the details of structural information of all synthesized cathodes obtained from the Rietveld refinements. Compared to P2-NMFO, reducing the content of Mn is more inclined to generate P2/O3 biphasic cathodes at the same synthesis temperature.

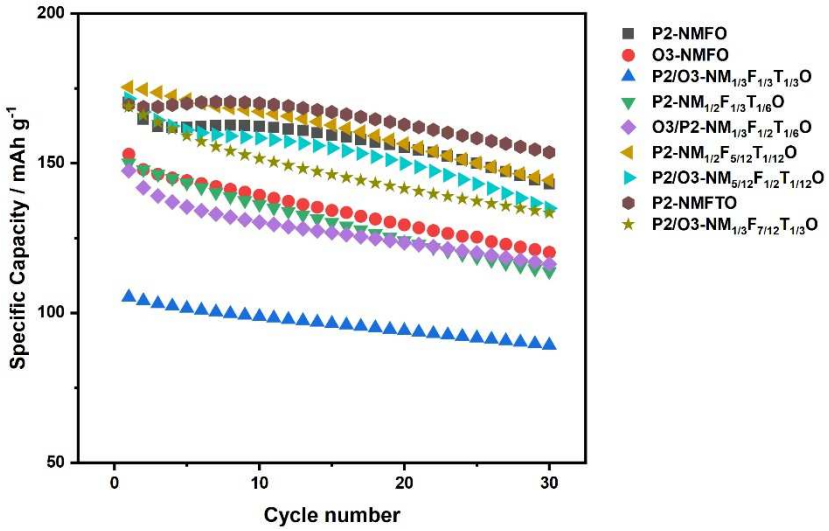

Figure 4.14 The electrochemical performance comparison of the synthesized cathode materials.

Table 4.2 The electrochemical performance comparison of synthesized cathode materials

	1st discharge capacity (mAh g^{-1})	Working voltage range	Cycle number and capacity retention
$NaMn_{1/2}Fe_{1/2}O_2$	153	1.5-4.3 V	30/78%
NMFO	168	1.5-4.3 V	30/73%
$NM_{1/3}F_{1/3}T_{1/3}O$	105	1.5-4.3 V	30/85%
$NM_{1/2}F_{1/3}T_{1/6}O$	150	1.5-4.3 V	30/76%
$NM_{1/3}F_{1/2}T_{1/6}O$	147	1.5-4.3 V	30/79%
$NM_{1/2}F_{5/12}T_{1/12}O$	173	1.5-4.3 V	30/82%
$NM_{5/12}F_{1/2}T_{1/12}O$	158	1.5-4.3 V	30/79%
NMFTO	170	1.5-4.3 V	30/90%
$NM_{1/3}F_{7/12}T_{1/12}O$	164	1.5-4.3 V	30/79%

The variations in discharge capacity for the first 30 cycles observed for the different cathodes is shown in Figure 4.14, which illustrates that the substitution of inactive Ti has a negative effect on most cathodes. The capacity of P2/O3-$NM_{1/3}F_{1/3}T_{1/3}O$ is only around 100 mA h^{-1} at 0.1 C in the voltage window of 1.5-4.3 V. The cathodes with a Ti content of 1/12 in the TM layers have higher capacity than P2-NMFO in the first three cycles. However, the capacities of $NM_{1/2}F_{5/12}T_{1/12}O$ and $NM_{5/12}F_{1/2}T_{1/12}O$ decrease very fast during cycling. The detailed electrochemical performance comparison of all synthesized cathode materials is shown in Table 4.2. The 1st discharge capacity of $NM_{1/3}F_{7/12}T_{1/2}O$ is a little bit higher than that of NMFTO, but the capacity retention after 30 cycles of NMFTO is the best among all synthesized cathodes.

4.1.3 Conclusion

Single phase P2-NMFO and O3-$NaMn_{1/2}Fe_{1/2}O_2$ were synthesized by a solid-state method. We have investigated the electrochemical performance and studied the structural changes occurring during cycling by *in situ* SRD. Moreover, to improve the electrochemical performance of Mn- and Fe-based layered sodium oxides, we substituted Ti into the TM layer to receive robust Mn-O-Ti-O-Fe bonds significantly improve the stability of the overall structure. We explored the structure and electrochemical properties of layered cathode materials with different Fe, Mn, and Ti ratios in the TM layers. Compared to P2-NMFO, reducing the content of Mn is more inclined to form P2/O3 biphasic materials, while inactive Ti reduces the capacity of the cathode material. By studying cathode materials with different compositions, we found that the Mn and Ti co-substituted P2-NMFTO material has the best electrochemical performance among all synthesized materials. The electrochemical reaction mechanism of the layered cathode material P2-NMFTO during cycling in sodium-ion batteries is explored in chapter 4.2.

4.2 Understanding the electrochemical reaction mechanism of the Co/Ni free layered cathode material P2-$Na_{2/3}Mn_{7/12}Fe_{1/3}Ti_{1/12}O_2$ for sodium-ion batteries

4.2.1. Introduction

Sodium-ion batteries (SIBs) are a low-cost alternative to lithium-ion batteries (LIBs) in large-scale electric energy storage applications due to the natural-abundant sodium resources and similar working principles to LIBs during cycling[108, 112, 113]. Until now, many different cathodes for SIBs have been studied, including layered transition metal (TM) oxides (Na_xTMO_2, $x \leq 1$), Prussian blue-type compounds, polyanionic and organic compounds. Among them, Na_xTMO_2 has been extensively investigated, due to its layered structure, facile synthesis, promising electrochemical properties, and feasibility for commercial production[11, 114-116]. The classification of layered oxides into O3, P2 and P3 types is based on the coordination environment of Na cations, which can be found in either octahedral or prismatic sites, and the stacking order of different oxygen layers such as ABCABC, ABBA, and ABBCCA[117]. At low potentials (<2.0 V vs Na/Na^+), there is a phase transition P2-P2' connected with the manganese redox activity and a significant Jahn-Teller distortion[51]. Compared with the O3-type structure, the P2-type Na_xTMO_2 provides higher specific capacity and better structural stability due to the lower diffusion barriers associated with prismatic sites of Na ions[118]. However, Na^+/vacancy interactions/orderings result in phase transitions upon cycling, leading to short cycle life and poor rate capability[119]. A first approach to alleviate the limits of P2-type cathodes is limiting the cut-off voltage to 4.1 V to avoid the P2-O2 transition[117]. The second approach is chemical modification which can suppress structural transitions at higher voltages. The initial report about P2-type NMFO is from Komaba's group, which demonstrated the activity of Fe^{3+}/Fe^{4+} redox couple during cycling. However, structural transitions result in poor capacity retention[73]. To address this challenge, replacing TM atoms in the TMO_2 slabs such as Ni-substituted and Mn/Ni co-substituted P2-$Na_x[Fe_{0.5-2y}Ni_yMn_{0.5+y}]O_2$ have been demonstrated as an effective

strategy to suppress these structural changes over a wider compositional range. As one example from the literature, Zn-doping prevents the phase transition of $Na_{0.60}Fe_{0.5}Mn_{0.5}O_2$ cathodes from P2 to OP4 during cycling[120]. Compared with NMFO, P2-type $Na_{2/3}Mn_{2/3}Fe_{1/3}O_2$ merely shows stacking fault distortions instead of a phase transition from P2-Z during cycling, where Z is a low-crystallinity phase which can be characterized as an evolving intergrowth that includes varying ratios of P2, O2, and OP4 structures, progressing from P2 through OP4 to O2 during the charging process (Na extraction)[121, 122]. This can improve the capacity retention. Nevertheless, the remaining P2' phase with space group *Cmcm* observed at the low potential range leads to anisotropic strain in the layered structure and deteriorates the electrochemical performance[75]. One way to avoid the Jahn-Teller distortion is to increase the low cut-off voltage to a value higher than 2.0 V with compromised specific capacity[77]. Moreover, the insertion of electrochemically inactive elements (Al[123], Mg[124]) into the layered oxide structure is an effective approach to mitigate Jahn-Teller distortion and enhance cycling performance.

Meanwhile, anionic redox activity, which has been frequently reported recently for LIBs, is also involved in the electrochemical process in a few cathode materials for SIBs. For example, Ma et al. provided evidence of the participation of oxygen anions in the charge compensation process of the high energy P2-type $Na_{0.78}Ni_{0.23}Mn_{0.69}O_2$ cathode material by electron energy loss spectroscopy (EELS) and soft X-ray absorption spectroscopy (sXAS)[125]. Maitra et al. claimed that oxygen redox activity in $Na_{2/3}Mg_{0.28}Mn_{0.72}O_2$ is associated with an extra capacity[126].

Herein, we present a structure optimization of the P2-type layered NMFO positive electrode material via a partial substitution of Fe by Mn and Ti to explore the electrochemical mechanism of redox activity of P2-type Mn/Fe based layered cathodes. The NMFO cathode exhibits subsequent phase transitions P2 → P2/Z → Z → Z/P2 → P2 → P2' during cycling[109], with Z being a highly disordered phase with cooperative Jahn-Teller distortions and possibly gliding of the TMO_2 slabs. However, in the modified NMFTO structure, the additional Mn^{4+} and Ti^{4+}

cations in the TM layers can suppress the P2-Z phase transition and decrease distortions in the structure. The similar ionic radii and the same valence of Mn^{4+} and Ti^{4+} ensure a homogenous incorporation of Ti^{4+} into the TM layers. As a result, the Mn^{4+}/Ti^{4+} co-substituted material (NMFTO) exhibits a single P2 phase during the whole charging/discharging process as revealed by *in situ* synchrotron radiation diffraction (SRD). *In situ* ^{57}Fe Mössbauer spectroscopy and *in situ* X-ray absorption spectroscopy (XAS) are used to characterize the reversible oxidation of Fe^{3+} to Fe^{4+}. The oxidation of Mn is also observed by *in situ* XAS. Moreover, *ex situ* ^{23}Na nuclear magnetic resonance (NMR) spectroscopy and *ex situ* soft X-ray absorption spectroscopy (sXAS) are performed to investigate the changes in the Na environments and the participation of oxygen anions during electrochemical cycling, respectively.

4.2.2. Results and discussion

Both P2-type layered compounds NMFO and NMFTO were synthesized as a single-phase material. X-ray diffraction (XRD) patterns (Figures 4.15a and 4.15b) show that all reflections of these two materials can be ascribed to a hexagonal lattice with space group $P6_3/mmc$, which is isostructural with P2-type Na_xCoO_2[14]. The unit cell parameters of NMFO ($a = b = 2.9241(7)$ Å, $c = 11.2491(52)$ Å) turn out to be larger than those of the substituted NMFTO ($a = b = 2.9191(1)$ Å, $c = 11.2369(10)$ Å). The received crystallographic characteristics for both materials are given in Table S4.3. The crystal structure illustration of both materials is shown in Figures 4.15c (NMFO) and 4.15d (NMFTO). The increased sodium interlayer spacing of the substituted material can promote Na^+ intercalation/deintercalation. The radii of Ti^{4+} (0.605 Å) and Mn^{4+} (0.53 Å) are smaller than that of Fe^{3+} (0.645 Å)[127], which leads to the reduced slab thickness of the TM layer of the substituted material. The primary particle size of both materials is approximately 500 nm, as shown in Figures 4.15e and 4.15f, and these primary particles are agglomerated forming several micrometer-sized secondary particles.

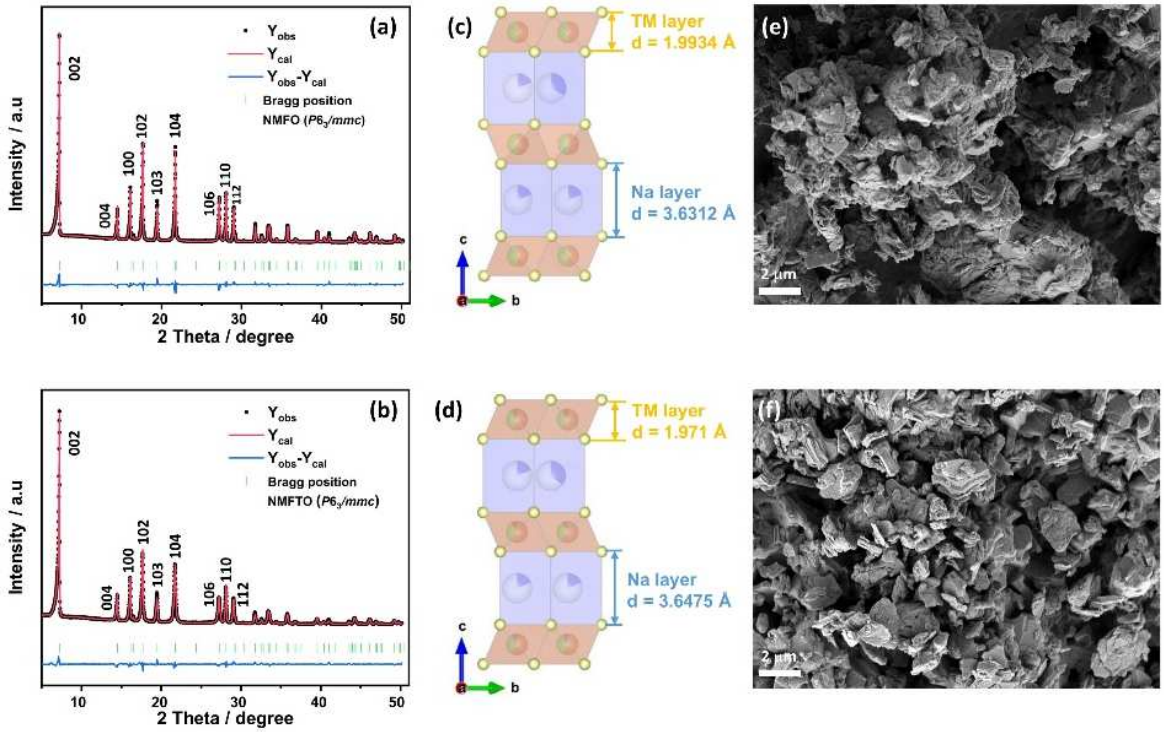

Figure 4.15. Rietveld refinement based on XRD (λ = 0.71 Å) of cathode materials (a) NMFO and (b) NMFTO. Crystal structure of (c) NMFO and (d) NMFTO. SEM images of pristine (e) NMFO and (f) NMFTO.

Table 4.3. Detailed structural information of P2-NMFO and P2-NMFTO

NMFO space group: *P6₃/mmc*		**R_p= 4.84%**		**R_{wp}= 6.64%**		
a = b = 2.9241(7) (Å)		**c = 11.2491(52) (Å)**		**V=83.298(6) (Å^3)**		
Atom	**Wyckoff position**	**x**	**y**	**z**	**Occupancy**	**U**
Na1	**2b**	**0**	**0**	**1/4**	**0.250**	**0.045**
Na2	**2d**	**1/3**	**2/3**	**3/4**	**0.420**	**0.053**
Mn	**2a**	**0**	**0**	**0**	**0.500**	**0.010**
Fe	**2a**	**0**	**0**	**0**	**0.500**	**0.010**
O	**4f**	**1/3**	**2/3**	**0.08830**	**1.000**	**0.009**

NMFTO space group: *P6₃/mmc*	**R_p= 4.46%**	**R_{wp}=5.93%**
a = b = 2.9191(1) (Å)	**c = 11.2369(10) (Å)**	**V=82.924(10) (Å^3)**

Atom	Wyckoff position	x	y	z	Occupancy	U
Na1	**2b**	**0**	**0**	**1/4**	**0.250**	**0.072**
Na2	**2d**	**1/3**	**2/3**	**3/4**	**0.420**	**0.037**
Mn	**2a**	**0**	**0**	**0**	**0.583**	**0.008**
Fe	**2a**	**0**	**0**	**0**	**0.333**	**0.008**
Ti	**2a**	**0**	**0**	**0**	**0.083**	**0.008**
O	**4f**	**1/3**	**2/3**	**0.08760**	**1.000**	**0.001**

A high-resolution transmission electron microscopy (HRTEM) image (Figure 4.16b) of NMFO displays two sets of lattice fringes with d-spacings of 0.247 and 0.253 nm, which can be indexed to the $(1\bar{1}1)$ and (010) planes of the $P6_3/mmc$ symmetry. The HRTEM image of NMFTO shown in Figure 4.17b displays two sets of lattice fringes with *d*-spacings of 0.246 and 0.252 nm, which are very similar to the values of the unsubstituted material. The corresponding fast Fourier transform (FFT) patterns (Figures 4.16c and 4.17c) exhibit an array of dots with a hexagonal symmetry. The high-angle annular dark-field scanning transmission electron microscopy (HAADF-STEM) together with energy dispersive X-ray spectroscopy (EDX) demonstrates that the elements are homogeneously distributed over the particles for both NMFO (Figure 4.16a, 4.16d-g) and NMFTO (Figure 4.17a, 4.17d-h).

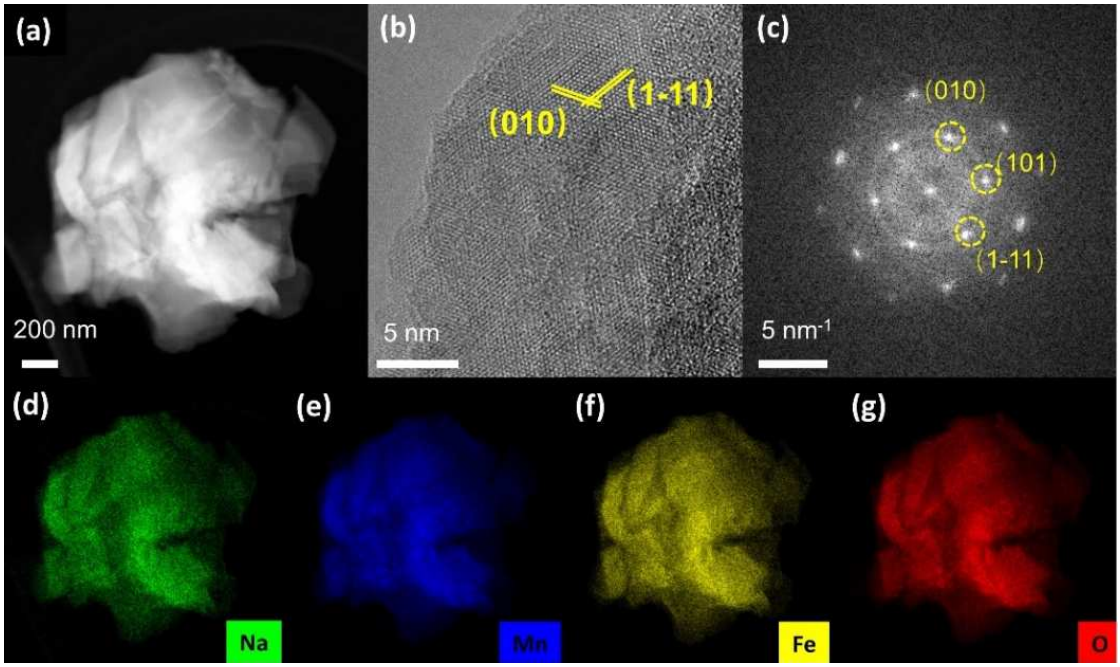

Figure 4.16. Morphology of pristine P2-NMFO. (a) HAADF-STEM image. (b) HRTEM image, and (c) corresponding FFT pattern. (d–f) HAADF-STEM-EDX elemental mapping.

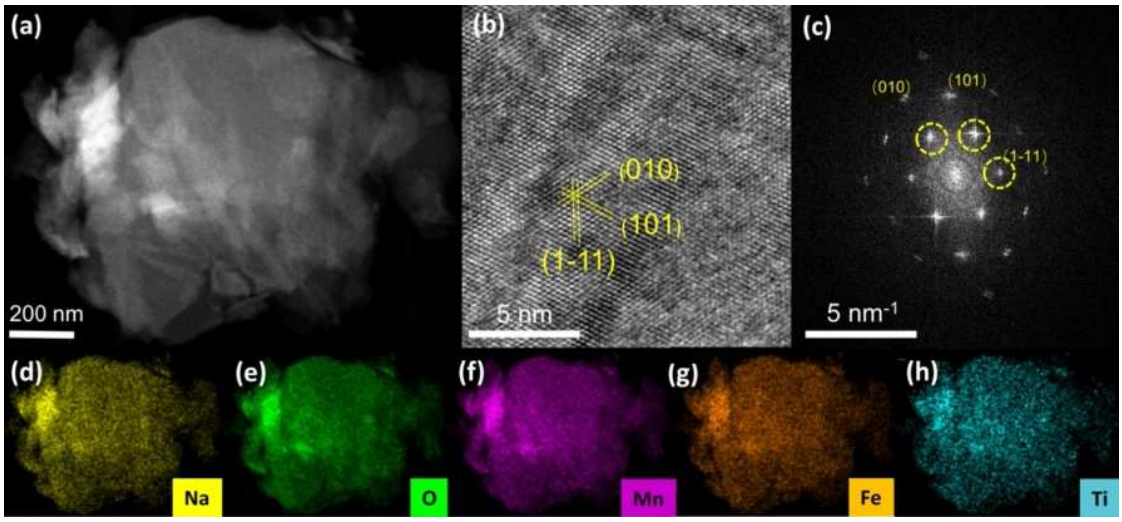

Figure 4.17. Morphology of pristine P2-NMFTO. (a) HAADF-STEM image. (b) HRTEM image, and (c) corresponding FFT pattern. (d-h) HAADF-STEM-EDX elemental mapping.

Figure 4.18 displays the results of electrochemical cycling for both cathodes against Na metal counter electrodes. The rate capability at rates between 0.05 C and 2 C are shown for P2-NMFO and P2-NMFTO in Figures 4.18a and 4.18b, respectively. In comparison to the slower cycling at 0.05 C (in the voltage range 1.5-4.3 V, NMFO delivers approximately 19% of specific

capacity for fast cycling at 2 C, while it is 42% for P2-NMFTO. This confirms the high stability of the substituted material. The charge/discharge curves at different rates show that the capacity is reduced and the polarization is increased with increasing current density. However, the effects for the substituted NMFTO are far less pronounced than those for unsubstituted NMFO. As shown in Figure 4.18c and 4.18d, compared to NMFO, the curves of NMFTO show much smaller polarization during cycling, which confirms the faster Na diffusion and thus high cycling stability of the substituted material.

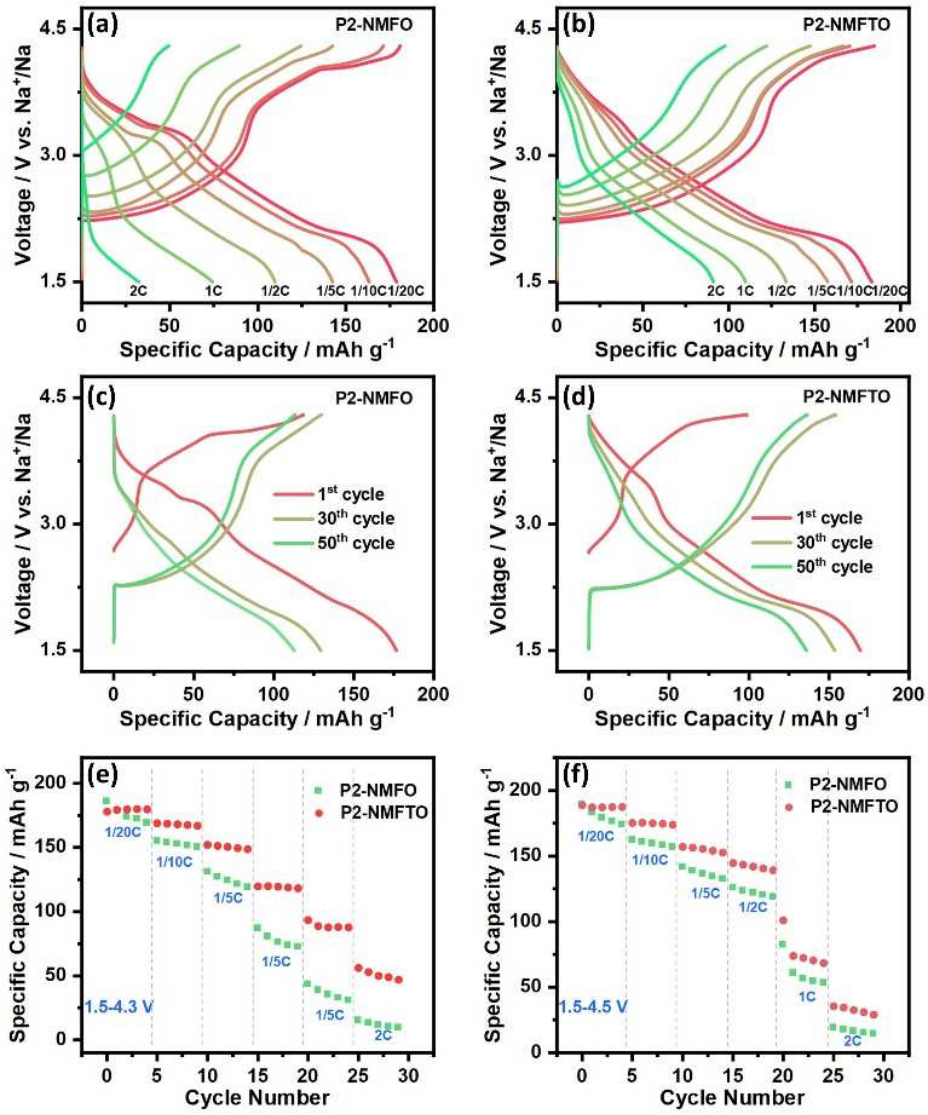

Figure 4.18. The charge/discharge curves at rates between 0.05 C and 2 C of (a) NMFO and (b) NMFTO; cell voltage as a function of specific capacity of (c) NMFO and (d) NMFTO for the 1st, 30th and 50th cycles at 0.1 C;

rate capability of NMFO and NMFTO at rates between 0.05 C and 2 C in the voltage window of (e) 1.5-4.3 V and (f) 1.5-4.5 V.

Moreover, the performance of both cathodes at different rates has been compared in Figures 4.18e (voltage window: 1.5-4.3 V) and 4.16f (voltage window: 1.5-4.5 V). The capacities of NMFTO are 180 mAh g^{-1}, 169 mAh g^{-1}, 152 mAh g^{-1}, 120 mAh g^{-1}, 93 mAh g^{-1}, and 56 mAh g^{-1} at 0.05 C, 0.1 C, 0.2 C, 0.5 C, 1 C, and 2 C, respectively, in the voltage range of 1.5-4.3 V. However, for NMFO, only 15.3 mA h^{-1} is obtained at 2 C. Figure 4.18f shows the capacities of both materials at different rates in the voltage range of 1.5-4.5 V, which reveals that the substituted NMFTO has higher capacities and better stability than the unsubstituted material, even in this larger voltage window.

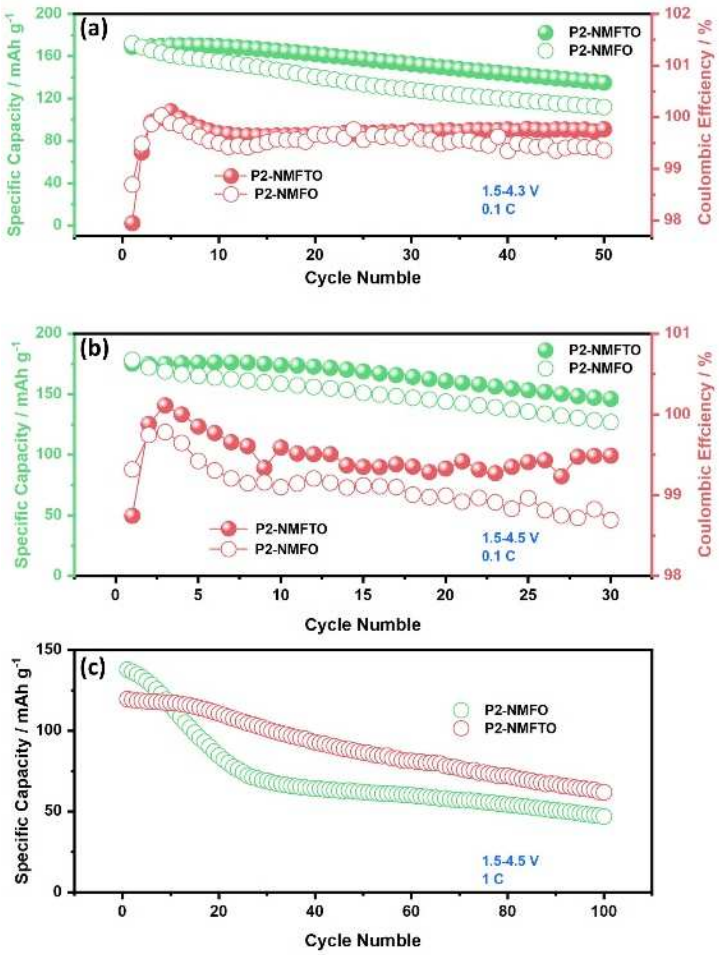

Figure 4.19. Cycling performance of NMFO and NMFTO at 0.1 C in the voltage window (a) 1.5-4.3V and (b) 1.5-4.5V; Cycling performance of NMFO and NMFTO at 1 C in the voltage window 1.5-4.5V.

The cycling performance of NMFO and NMFTO in the voltage range of 1.5-4.3 V at 0.1 C are compared in Figure 4.19a. NMFTO has a significantly improved cycling stability with an initial discharge capacity of 168 mAh g^{-1} at 0.1 C and a capacity retention of 80% after 50 cycles, while the capacity retention of NMFO is just 65%. The cycling performance is also tested in the voltage range of 1.5-4.5 V to compare the stability of both materials at higher working voltages, as shown in Figure 4.19b. The capacity retention of NMFTO is 83% after 30 cycles, and it is only 71% for NMFO. For NMFO, the Coulombic efficiency also drops below 99% after about 20 cycles. The electrochemical performance comparison of reported iron- and manganese-based cathodes and materials is summarized in Table 4.4, which shows that Ti substituted P2-NMFTO has better cycling stability than most iron- and manganese- based cathodes due to the single-phase reaction of NMFTO observed during cycling. The cycling performance of NMFO and NMFTO at 1 C in the voltage window of 1.5-4.5 V is displayed in Figure 4.19c. The results reveal that substituted NMFTO has a better cycling stability even in the higher potential range and at a higher scan rate.

Table 4.4. The electrochemical performance comparison of reported iron- and manganese- based cathodes and materials in this paper.

	1st discharge capacity (mAh g^{-1})	Working voltage	Cycle number and capacity retention
P2-$Na_{0.66}Mn_{2/3}Fe_{1/3}O_2$	**180 (C/20)**	**1.5-4.3 V**	**50/66%** [128]
P2-$Na_{0.62}Mn_{1/2}Fe_{1/2}O_2$	**184 (C/20)**	**1.5-4.3 V**	**50/64%** [128]
P2-$Na_{2/3}Fe_{2/3}Mn_{1/3}O_2$	**151 (C/10)**	**1.5-4.2 V**	**10/81%** [129]
O3-$NaFe_{1/2}Mn_{1/2}O_2$	**170 (C/20)**	**1.5-4.3 V**	**50/73%** [130]
O3-$Na_{5/6}Fe_{1/2}Mn_{1/2}O_2$	**193 (C/20)**	**1.5-4.3 V**	**50/69%** [103]
P2-$Na_{2/3}Mn_{1/2}Fe_{1/2}O_2$	**160 (C/10)**	**1.5-4.3 V**	**50/70%**
	178 (C/10)	**1.5-4.5 V**	**30/71%**
P2-$Na_{0.67}Mn_{0.475}Fe_{0.475}Ti_{0.05}O_2$	**192 (C/20)**	**1.5-4.2 V**	**50/63%** [131]

P2-$Na_{0.6}Li_{0.11}Fe_{0.27}Mn_{0.62}O_2$	**195 (C/10)**	**1.5-4.5 V**	**80/52%** [132]
O3-$Na_{5/6}Fe_{1/3}Mn_{1/2}Cu_{1/6}O_2$	**176 (C/20)**	**1.5-4.3 V**	**50/79%** [103]
O3-$Na_{5/6}Fe_{1/3}Mn_{1/2}Mg_{1/6}O_2$	**196 (C/20)**	**1.5-4.3 V**	**50/63%** [103]
P2-$Na_{0.7}Fe_{0.4}Mn_{0.4}Co_{0.2}O_2$	**188 (C/20)**	**1.5-4.5 V**	**60/61%** [133]
P2-$Na_{2/3}Mn_{7/12}Fe_{1/3}Ti_{1/12}O_2$	**170 (C/10)**	**1.5-4.3 V**	**50/80%**
	175 (C/10)	**1.5-4.5 V**	**30/83%**

Figure 4.20a shows the first five cyclic voltammogram (CV) curves of NMFO and NMFTO at a scan rate of 0.1 mV s^{-1}. For NMFO, the reduction in peak intensity involving O oxidation at about 4.25 V after 5 cycles is larger than for NMFTO. The loss of O in NMFO at high voltages results in a rapid decrease of O-redox activity in the following cycles. The oxidation and reduction peaks of NMFTO show very small polarization after cycling, which reveals the improved stability, lower polarization, and more reversible cationic redox activity of the substituted materials[134]. The first five CV cycles of NMFO (Figure 4.20b) and NMFTO (Figure 4.20c) at 0.1 mV s^{-1} in the voltage window of 1.5-4.5 V show that the oxidation and reduction peaks of NMFTO after cycling in a larger voltage window show again a smaller polarization than for the unsubstituted material, especially for the Fe reduction peaks observed at 2.8 V. Figure 4.20d presents the dQ/dV result of NMFO and NMFTO in the potential range of 1.5-4.3 V. The Mn oxidation and reduction peaks for NMFO are observed at around 2.6 V and 2.0 V. The Mn oxidation peak for NMFTO is located at around 2.75 V, which reveals that the oxidation of Mn occurs a little bit later than for NMFO. The peak belonging to Fe reduction occurs around 3.25 V. However, the Fe reduction peak of NMFO is more pronounced than that of NMFTO. Oxide oxidation occurs at the end of charging and the reaction in NMFO occurs earlier than in NMFTO. The dQ/dV curves of NMFO and NMFTO at a scan rate of 0.1 mV s^{-1} in the voltage ranges of 1.5-4.3 V and 1.5-4.5 V has also been measured. For NMFO (Figure 4.20e), when the cathode is charged to higher voltages, the Fe reduction peak shows a drastic change, while the

corresponding peaks of NMFTO (Figure 4.20f) are very stable, which indicates the better structural stability of the substituted material even in the wider potential window.

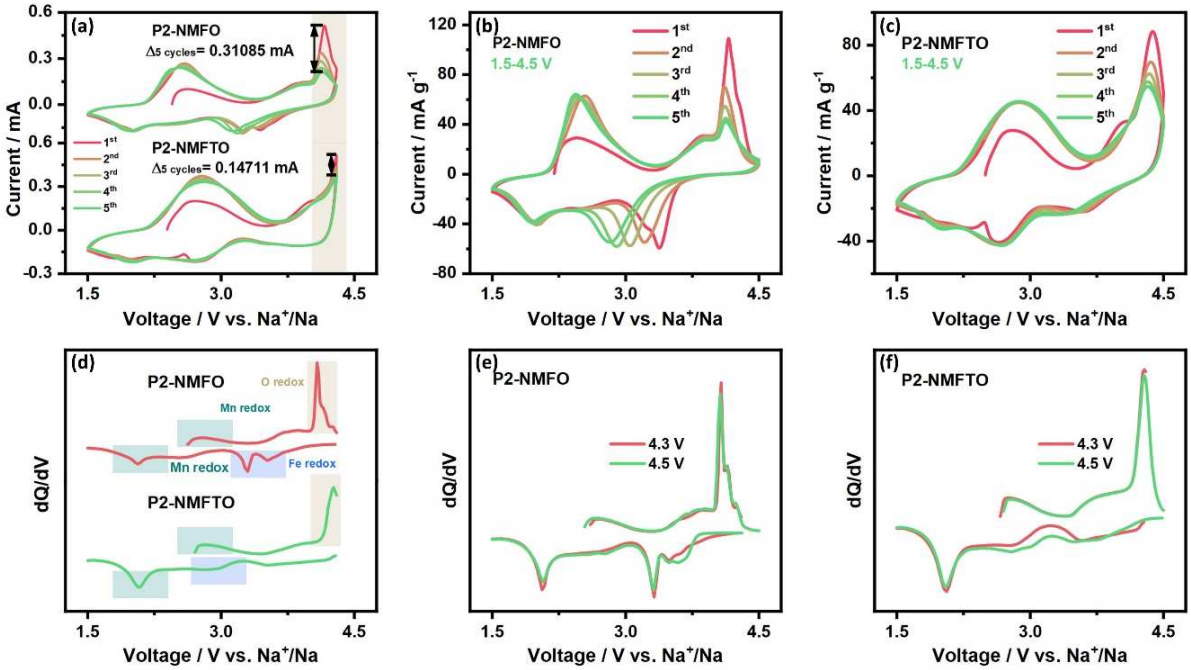

Figure 4.20 (a) First five CV curves of NMFO and NMFTO at 0.1 mV/s in the voltage range of 1.5-4.3 V; First five CV cycles of (b) NMFO and (c) NMFTO at 0.1 mV/s in the voltage range 1.5-4.5 V; (d) dQ/dV curves of NMFO and NMFTO at 0.1 C; dQ/dV curves of (e) NMFO and (f) NMFTO at 0.1 C in the voltage ranges 1.5-4.3 V and 1.5-4.5 V.

To explain the better performance of substituted NMFTO, *in situ* and *ex situ* measurements were performed to explore the overall reaction mechanism. The structural evolution of NMFO was displayed in Figure 4.5. The structural evolution of NMFTO during Na^+ deintercalation/reintercalation was investigated by *in situ* SRD measurements at 0.1 C rate in the voltage range 1.5-4.3 V, as shown in Figure 4.21. In stark contrast to NMFO, the contour maps of NMFTO (Figure 4.21a) demonstrate that all reflections show only shifts and no new reflections appear during the whole charging/discharging process, implying a solid-solution behavior upon Na^+ deintercalation/reintercalation. During the charging process of NMFTO, the 002, 004, and 106 reflections are shifted to lower angles and they are shifted back to higher angles during the discharging process, again revealing the changes of the interlayer spacings

(Figure 4.21b). Meanwhile, the 100, 102, 110, and 112 reflections are shifted towards higher angles showing a gradual contraction of the intralayer spacing during the charging process and they are shifted back to lower angles during the discharging process (Figure 4.21c). As reported in earlier work[77], no P2→Z phase change occurs for $Na_{2/3}Mn_{2/3}Fe_{1/3}O_2$ at highly charged states, i.e. Mn substitution can suppress sliding of the TMO_2 slabs. At the same time, Ti substitution in NMFO can suppress the formation of the P2' phase in deeply discharged states, thus improving the capacity retention during cycling.

The XRD diffraction patterns of NMFO and NMFTO are shown in Figures 4.22a and 4.22b for the pristine state, after one full cycle, and after two full cycles in two different voltage ranges at 1.5-4.3 V and 1.5-4.5 V, respectively. For the smaller voltage range 1.5-4.3 V, the XRD patterns obtained for the pristine electrode and after one or two cycles do not show significant changes for both materials. However, when the cathodes are charged to 4.5 V, the patterns for NMFTO in the discharged state after one and two cycles show higher stability than the unsubstituted NMFO material. These results reveal that Mn^{4+}/Ti^{4+} substitution can increase the stability of such materials towards higher voltages.

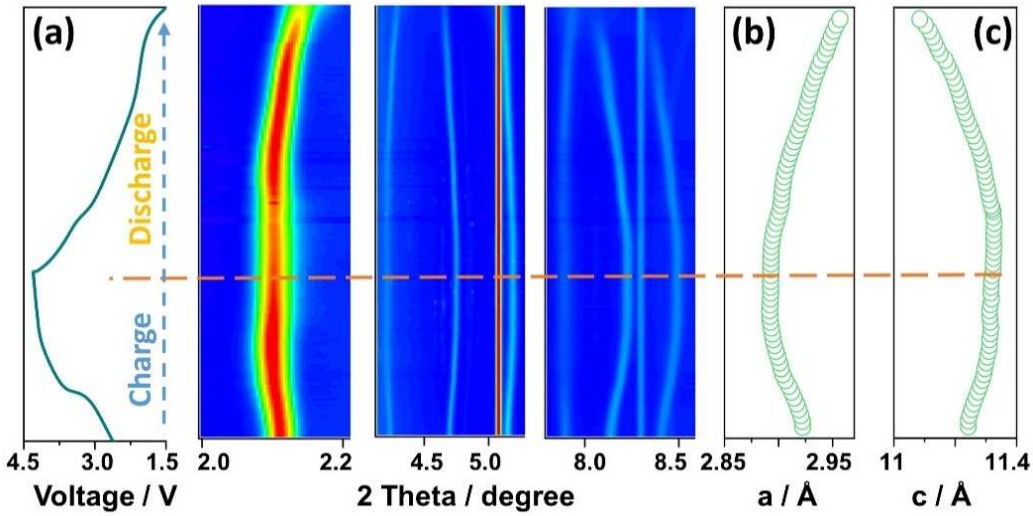

Figure 4.21. Contour maps (a) of *in situ* synchrotron diffraction data collected during the first charge/discharge process and the corresponding voltage profiles on the left side and the changes of the lattice parameters on the right side (b, c) for NMFTO at 0.1 C rate and over the voltage range 1.5-4.3 V.

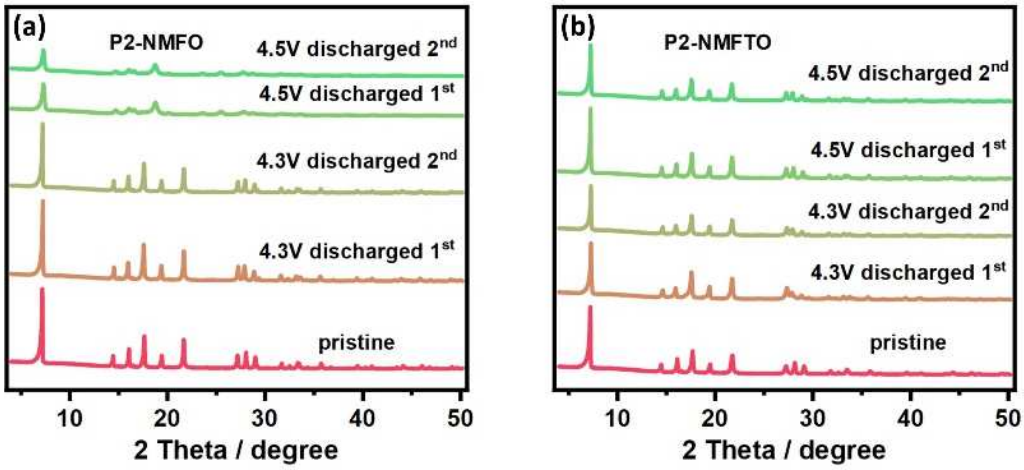

Figure 4.22. XRD diffraction patterns of (a) NMFO and (b) NMFTO in the pristine state, after one full cycle, and two full cycles for two different voltage ranges, 1.5-4.3 V and 1.5-4.5 V.

To investigate the local structural changes in more detail, *ex situ* ^{23}Na MAS NMR measurements were performed on as-synthesized NMFO and NMFTO cathodes and on electrodes extracted from cells after charging/discharging to different voltages during the first cycle (Figures 4.23a-4.23d). The spectrum of pristine NMFO (Figure 4.23b) shows a major resonance at ca. 1850 ppm. A much narrower signal close to 0 ppm indicates the presence of diamagnetic impurities such as NaOH/Na_2CO_3 or residues of the electrolyte salt or the solid-electrolyte interphase. For the spectrum of pristine NMFTO (Figure 4.23d), the major resonance is located at around 1500 ppm. The comparison of the spectra of pristine NMFO and pristine NMFTO is shown in Figure 4.24. The decrease of the ^{23}Na NMR shift in NMFTO compared to NMFO is caused by the substitution of diamagnetic Ti^{4+} for highly paramagnetic Mn^{4+} centers with large magnetic moments in the environment around Na[80, 135]. According to the elemental composition, the average oxidation state of Mn in pristine NMFO is +3.66 and +3.43 in NMFTO (as shown below with Mössbauer spectroscopy, the oxidation state of Fe is 3+ in the pristine state for both materials). After charging to 3.85 V, the ^{23}Na shift decreases to 1650 ppm. This shift to lower ppm values is caused by the oxidation of high-spin Fe^{3+} (electronic configuration $3d^5$) to Fe^{4+} ($3d^4$) resulting in less unpaired electronic spins. When NMFO is further charged to 4.1 V, the NMR shift is a little bit higher (1612 ppm) than the value obtained at 3.85 V revealing

that now the oxidation of low-spin Mn^{3+} ($3d^4$) to Mn^{4+} ($3d^3$) is dominating. During the whole charging process, a clear decrease in the intensity of this major resonance is observed since more and more Na is removed from the material and finally, at 4.3 V, the signal completely disappeared, revealing that Na is almost completely removed from the structure. During discharging, the ^{23}Na resonance shifts back to higher ppm values due to the reduction of Fe^{4+} to Fe^{3+}. When NMFO is further discharged to 1.9 V, the ^{23}Na signal becomes very broad and almost invisible. As shown above via *in situ* SRD, the P2' phase starts to appear at around 1.9 V, which means that local distortions around Mn occur which can reduce the mobility of Na^+. The evolution of the ^{23}Na NMR spectra during this complete cycle clearly shows that after the full discharge the cathode material is reduced to a state beyond the pristine state, as also expected from the voltage profile, i.e. after the reversible changes observed in the spectra, an additional reduction of the material is observed associated with a sodiation above the initial Na content of 0.67.

For NMFTO (Figure 4.23d), during the charging period, the main resonance is shifted to lower values due to the oxidation of Fe. Even in the fully charged state, some residual intensity is observed for the broad main resonance, in contrast to NMFO. This residual intensity reveals that NMFTO is not completely desodiated by charging to 4.3 V. The residual Na content observed at 4.3 V explains why the capacity of NMFTO can be further increased by cycling in the larger voltage window 1.5-4.5 V. During the discharging period, the resonance shifts back to higher values due to the reduction of Fe. When the cathode is further discharged to 2.0 V, the signal becomes very broad and again is difficult to be detected. Also, for this material, the overall evolution of the spectra shows that after one complete cycle the material is reduced to a state beyond the initial state, i. e. sodiated to a Na content higher than in the pristine material.

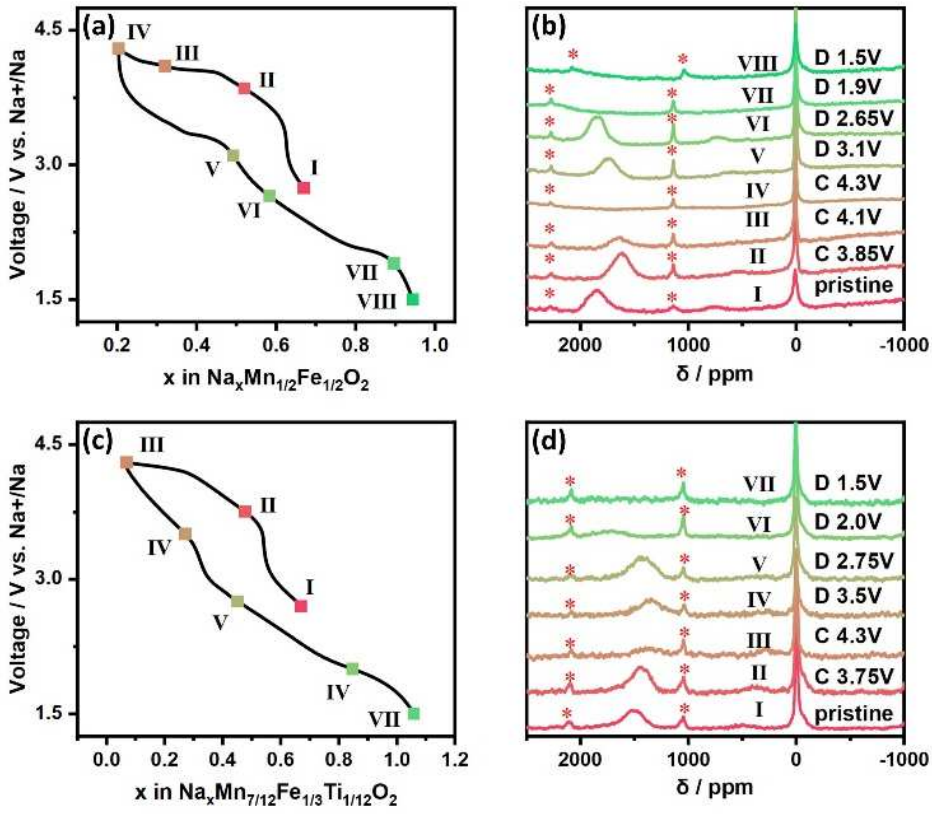

Figure 4.23. Cell voltage as a function of the state of charge and discharge for the first galvanostatic cycle of (a) NMFO and (c) NMFTO cells; marked points indicate voltages where cells were disassembled for solid-state NMR measurements. ^{23}Na MAS NMR spectra of (b) NMFO and (d) NMFTO cathode samples. Spinning sidebands are denoted with "*".

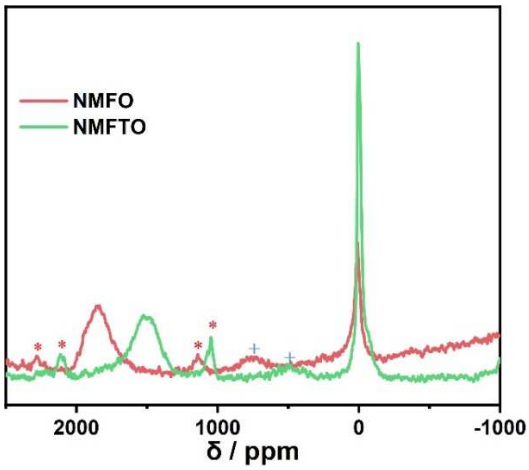

Figure 4.24. ^{23}Na MAS NMR spectra of pristine NMFO and NMFTO cathodes. Spinning sidebands are denoted with "*", "+".

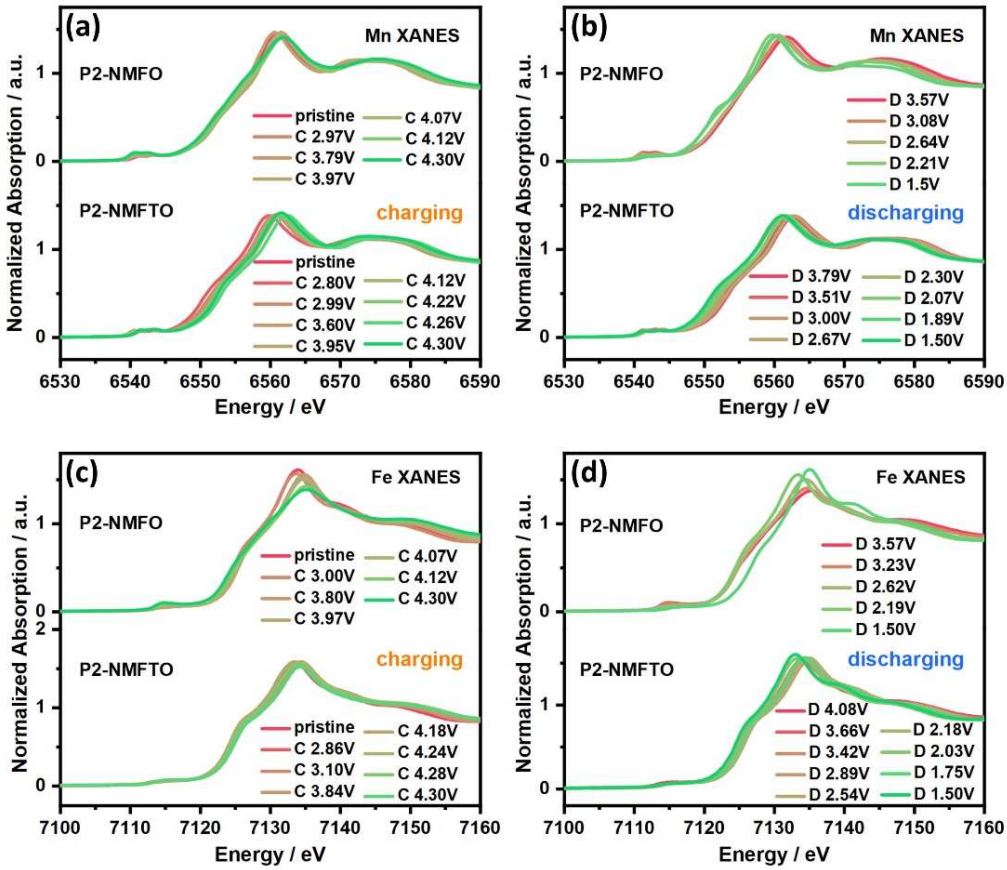

Figure 4.25. XANES spectra at Mn K-edge during charging (a) and discharging (b). XANES spectra at Fe K-edge during charging (c) and discharging (d).

The changes in the electronic structure and local environments of manganese and iron in NMFO and NMFTO during the first cycle are studied by *in situ* XAS. As described above, the average valence of Mn is +3.66 in pristine NMFO and +3.43 in NMFTO. For both materials, the Mn K-edge shifts to higher energies upon charging (Figure 4.25a) and shifts back to lower energies throughout the whole discharging process (Figure 4.25b), indicating the continuous oxidation and reduction of Mn during charging/discharging. Figure 4.27e shows the linear combination fitting for the variations of Mn^{3+}/Mn^{4+} contents during cycling which corresponds to the XANES data described above. As seen from this figure, Mn is almost completely oxidized to Mn^{4+} at the end of charge and reduced to Mn^{3+}/Mn^{4+} with a ratio of about 1:1 at the end of discharge. However, for NMFTO, Mn is not fully oxidized to Mn^{4+} at the end of charging and reduced to Mn^{3+}/Mn^{4+} with a ratio of about 0.7:0.3 at the end of discharging, which contributes to the better electrochemical performance of the substituted NMFTO material. This is consistent

with *in situ* Mn K-edge XANES results of both materials in the pristine, fully charged, and fully discharged state (Figure 4.27a). The Fe K-edge for both materials also shifts to higher energies upon charging (Figure 4.25c) and shifts back to lower energies upon discharging (Figure 4.25d), again revealing the reversible oxidation and reduction of Fe. *In situ* XANES spectra in the pristine, fully charged, and fully discharged state confirm this tendency (Figure 4.27b).

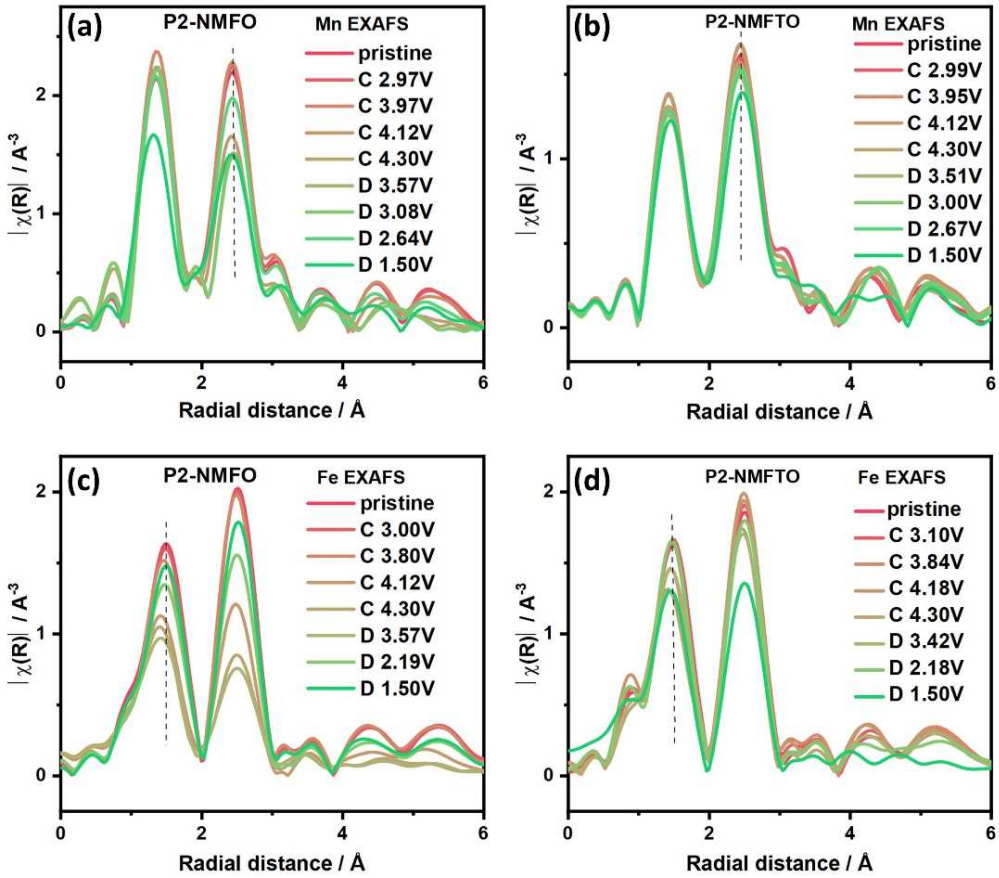

Figure 4.26. (a) Fourier transforms (k^3-weighted) of Mn K-edge EXAFS spectra of NMFO. (b) Fourier transforms (k^3-weighted) of Mn K-edge EXAFS spectra of NMFTO. (c) Fourier transforms (k^3-weighted) of Fe K-edge EXAFS spectra of NMFO. (d) Fourier transforms (k^3-weighted) of Fe K-edge EXAFS spectra of NMFTO.

The Mn K-edge and Fe K-edge Fourier-transformed (k^3-weighted) EXAFS (FT-EXAFS) spectra acquired during charging/discharging are shown in Figure 4.26 (a-b: Mn K-edge; c-d: Fe K-edge). There are two peaks at about 1.3 and 2.3 Å in the radial distributions, corresponding to the TM-O distance and the TM-TM/Na distance, respectively. For NMFO, the amplitude of the Mn-O peak is higher than that of the Mn-TM peak, while the opposite behavior is observed

for NMFTO. During the first charging process, the intensity of the Mn-O peak slightly decreases due to the oxygen redox process. The change of this Mn-O peak during discharging is very weak for NMFTO, while for NMFO a strong decrease in intensity occurs in the voltage range from 2.21 V to 1.5 V. This strong change can be ascribed to the local Jahn-Teller distortions around Mn^{3+} and also the phase change observed via XRD in the highly discharged states. The shift of the second Mn-TM peak to a larger value, observed for NMFO and NMFTO, indicates the increase of the Mn-TM distance. This is consistent with the changes in the *a* lattice constant observed by SRD, as described above. For NMFTO, the Mn-O and Mn-TM bond length variations are fully reversible as observed in the subsequent discharging process, and the interatomic distances return to their initial values. For NMFO, a clear decrease in the intensity of the Mn-O peak at the very end of discharging (Figure 4.26a and 4.27c) is observed. This strong decrease in intensity is not observed for NMFTO, which indicates that the Ti substitution can mitigate the Jahn-Teller distortion. The intensities of the Fe-O peak are lower than that of the Fe-TM peak for both materials. The variations in the Fe-O and Fe-TM bond lengths of both materials are not completely reversible, as shown in Figure 4.27d. When comparing the spectrum in the pristine state with that in the fully charged state, the radial distribution of NMFO shows a decrease in the Fe-O distance and a reduced intensity of the Fe-TM peak during charging. Meanwhile, the increase in the intensity of the pre-edge peak in the Fe K-edge XANES spectra indicates the migration of a small fraction of Fe ions into interlayer P2-tetrahedral sites at voltages higher than 4.1 V[122].

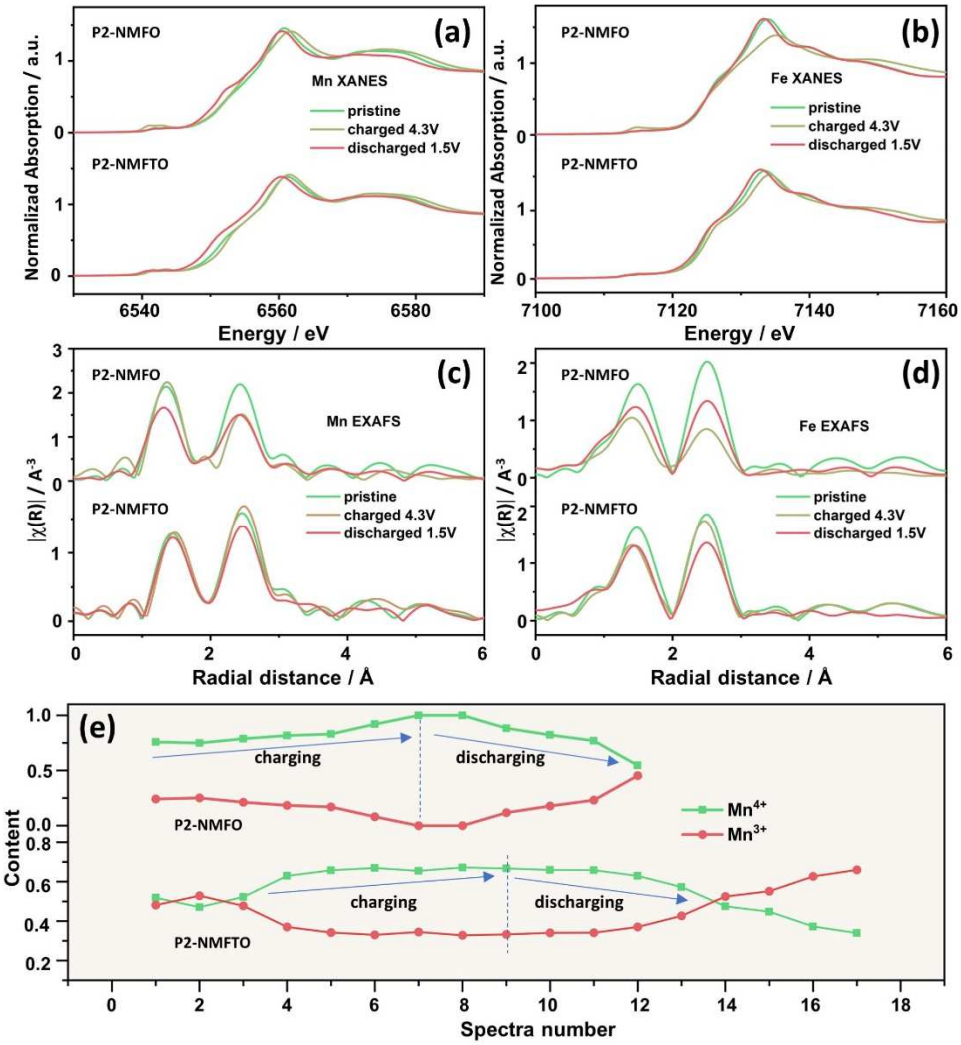

Figure 4.27. Fe K-edge and Mn K-edge XAS spectra of NMFO and NMFTO at different charge states (a) XANES spectra at Mn K-edge. (b) XANES spectra at Fe K-edge. (c) Fourier transforms (k^3-weighted) of Mn K-edge EXAFS spectra. (d) Fourier transforms (k^3-weighted) of Fe K-edge EXAFS spectra. (e) Linear combination fitting of *in situ* Mn K-edge XAS.

In situ ^{57}Fe Mössbauer spectroscopy on complete cells during cycling was performed to investigate the change of Fe oxidation state as displayed in Figure 4.28. Cycling of the cells was evaluated in the voltage range of 1.5-4.3 V, and one Mössbauer spectrum was acquired every 2 h. The voltage profiles and contour plots of *in situ* ^{57}Fe Mössbauer spectroscopy during the first cycle are shown in Figure 4.28a (NMFO) and 4.28b (NMFTO). For both cathodes, the contour plots clearly show the reversible partial conversion of Fe^{3+} to Fe^{4+} and back to Fe^{3+}

during the cycling. The detailed parameters resulting from fitting all ^{57}Fe Mössbauer spectra are shown in Figure 4.29.

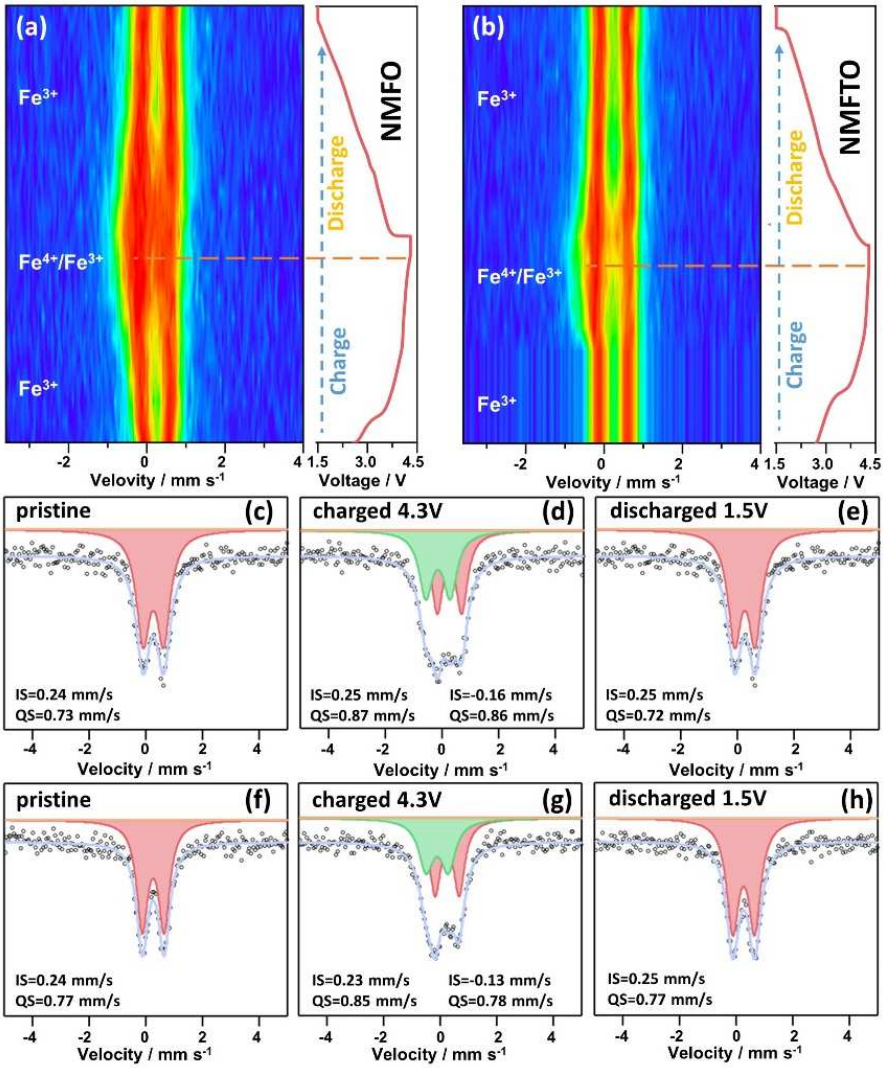

Figure 4.28. Voltage profiles and contour plots of *in situ* ^{57}Fe Mössbauer spectroscopy on (a) NMFO and (b) NMFTO during cycling between 1.5-4.3 V at a rate of 0.05 C. ^{57}Fe Mössbauer spectra of NMFO in different states: (c) pristine, (d) charged to 4.3V and (e) discharged to 1.5 V. ^{57}Fe Mössbauer spectra of NMFTO: (f) pristine, (g) charged to 4.3V and (h) discharged to 1.5 V. The experimental spectra are shown as black spheres, the fitting as purple lines. Fe^{3+} and Fe^{4+} contributions are shown as red and green doublets, respectively.

As shown in Figure 4.28c and 4.28f, the spectra for both pristine materials exhibit a single sharp doublet with an isomer shift (IS) around ~0.24 mm s^{-1} consistent with Fe^{3+} in high-spin state and in an octahedral environment of oxygen[136]. The quadrupolar splitting (QS) of NMFTO is around 0.77 mm s^{-1} and larger than that of unsubstituted NMFO (0.73 mm s^{-1}), revealing a less

symmetric environment. As can be seen from the contour plots, a new component appears in the spectra with negative isomer shift that can be assigned to Fe^{4+} [137]. A higher amount of Fe^{4+} is observed for NMFO at the end of charging in comparison to NMFTO (Figure 4.29). This might be related to the larger overall Fe content in NMFO where a larger fraction of the specific capacity is based on Fe^{3+}/Fe^{4+} redox activity. This in turn can contribute to the better cycling stability of NMFTO where the specific capacity is more based on Mn^{3+}/Mn^{4+} activity. The spectra of NMFO and NMFTO in the fully discharged state (Figure 4.28e and 4.28h) are very similar to those of the pristine materials with almost identical IS and QS values, demonstrating the complete reduction back to Fe^{3+} and thus the high reversibility of this redox process. The spectra of the charged materials (Figure 4.28d and 4.28g) were fitted using two doublets. The first component is ascribed to $Fe^{3+}O_6$ in an octahedral environment with isomer shift IS very similar to that of the pristine material while the quadrupole splitting QS is larger compared to the pristine materials, revealing local distortions of the octahedral environment around Fe. The second doublet with negative isomer shift clearly reveals the existence of Fe^{4+}, and all Fe^{4+} is reduced back to Fe^{3+} during discharging. The Fe^{4+} doublet observed in the charged state of NMFO shows a larger isomer shift and a larger quadrupole splitting than that of NMFTO, revealing stronger local distortions.

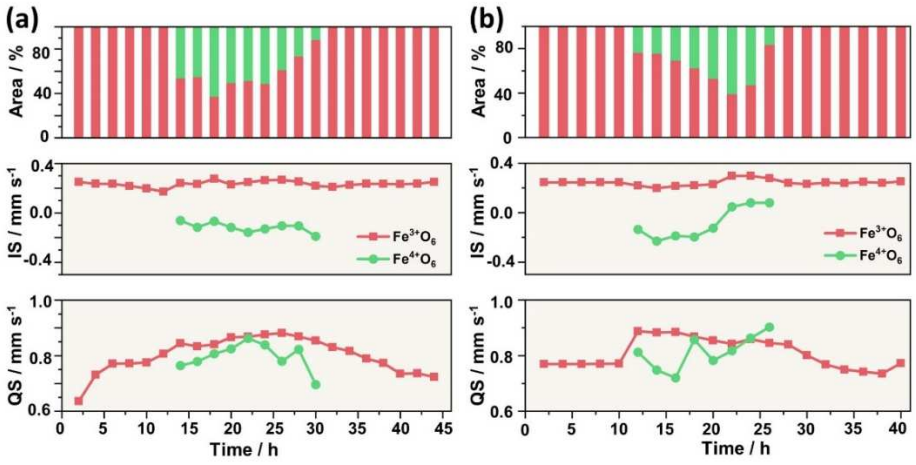

Figure 4.29. Parameters resulting from fitting of *in situ* ^{57}Fe Mössbauer spectra of (a) NMFO and (b) NMFTO.

Ex situ soft XAS measurements were performed on NMFO and NMFTO cathodes extracted from cells at different voltages during the first cycle (Figure 4.30a and 4.30e) to probe changes in the oxidation states and chemical environments. The Mn L-edge XAS spectra acquired in the inverse fluorescence yield (iFY) mode are shown in Figures 4.30b and 4.30f. The peak at 642 eV is ascribed to Mn^{3+} and the peaks at 641 eV and 643 eV correspond to Mn^{4+}[138]. The spectra for both cathodes obtained in the pristine state demonstrate that Mn exists in a mixed oxidation state Mn^{3+}/Mn^{4+}, which is in good agreement with the results on the Mn K-edge described above. The spectra show no pronounced change in the fully charged state. However, during discharging, when the potential reaches 2.65 V, the spectra of both materials show predominantly the Mn^{3+} peak. The L_3-edge (observed at 643 eV) of both materials shows almost no change when going from 2.65 V to 1.5 V. However, for the L_2-edge (observed at 653.6 eV), the spectra of NMFTO have clearer features of Mn^{3+}, which indicates that Mn in NMFTO can be reduced to lower valence states, in agreement with the result obtained by linear combination fitting of *in situ* XAS Mn K-edge data (Figure 4.27e). The Fe L-edge XAS spectra in the iFY mode for these samples are shown in Figure 4.30c and 4.30g. The Fe L-edge spectra of both pristine materials show obvious features of Fe^{3+}[139], in good agreement with the Mössbauer results. However, no big changes can be observed during charging. We ascribe this to the fact that these measurements are performed *ex situ* and the stability of Fe^{4+} seems to be limited outside the batteries. The changes of the Fe oxidation state during cycling can thus be much better observed by the *in situ* Mössbauer measurements.

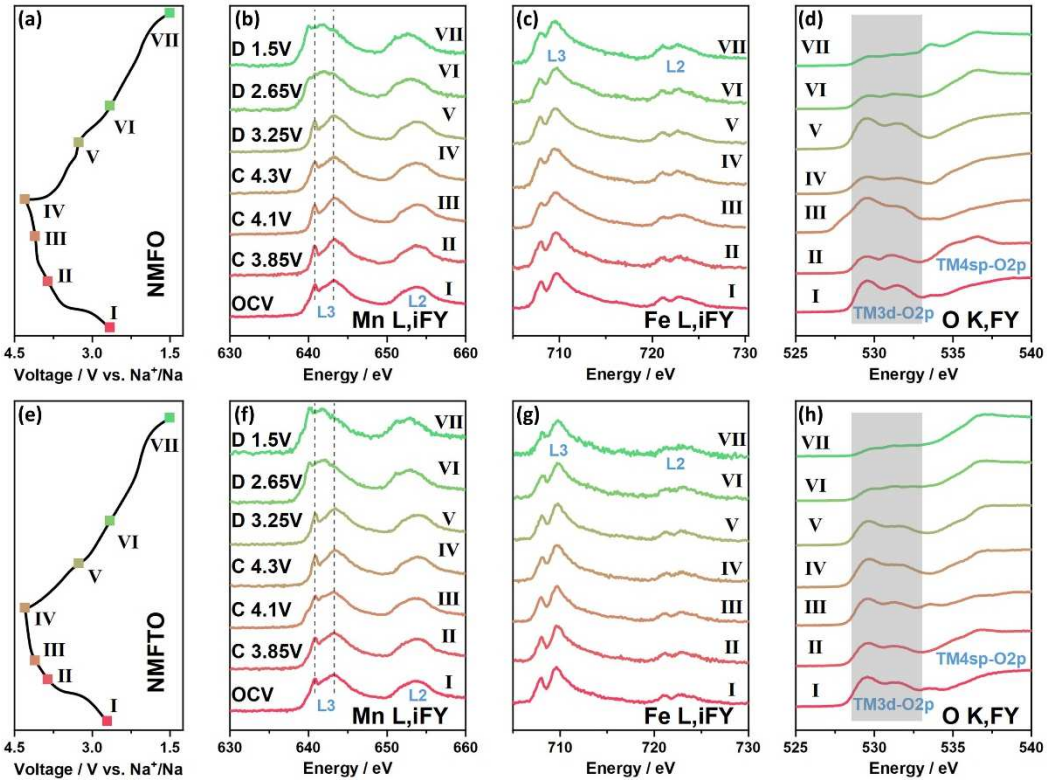

Figure 4.30. Cell voltage as a function of state of charge and discharge for the first galvanostatic cycle of (a) NMFO and (e) NMFTO cells; marked points indicate voltages where cells were disassembled for soft XAS measurements. Mn $L_{2,3}$ (b), Fe $L_{2,3}$ (c) and O K (d) NEXAFS spectra of NMFO at different voltages. Mn $L_{2,3}$ (f), Fe $L_{2,3}$ (g) and O K (h) NEXAFS spectra of NMFTO at different voltages.

The O K-edge XAS spectra are shown in Figure 4.30d and 4.30h. They can be used to explain the interplay between cationic TM redox and anionic oxygen redox activity. For the O K-edge, the pre-edge peaks below 535 eV are related to the hybridization of O 2p-TM 3d orbitals, while the broad peak above 535 eV is related to O 2p-TM 4sp hybridized states. The peaks around 529.4 eV and 531.3 eV correspond to contributions from the t_{2g} band and the e_g band, respectively. Because the density of the empty bound state in the molecular energy level is related to the hybridization of metal 3d-O 2p orbitals, the variation of integrated pre-edge intensity (shadow region in Figure 4.30d and 4.30h) can show the hole state distribution and the effective charge on the oxygen atom[140]. The integrated intensity which reflects the changes in the density of empty states was calculated and displayed in Figure 4.31. For NMFO, the intensity of the integrated pre-edge (Figure 4.31a) shows irregular changes during the charging

and discharging process, which are caused by gliding of TMO_2 slabs during phase change processes. However, for NMFTO, the intensity of integrated pre-edge (Figure 4.31b) shows regular changes during the electrochemical cycling, which is relevant to electron removal from oxygen and the consequently generated holes in O 2p orbitals[141]. The changes in O K-edge confirm that the substituted NMFTO is more stable compared to NMFO.

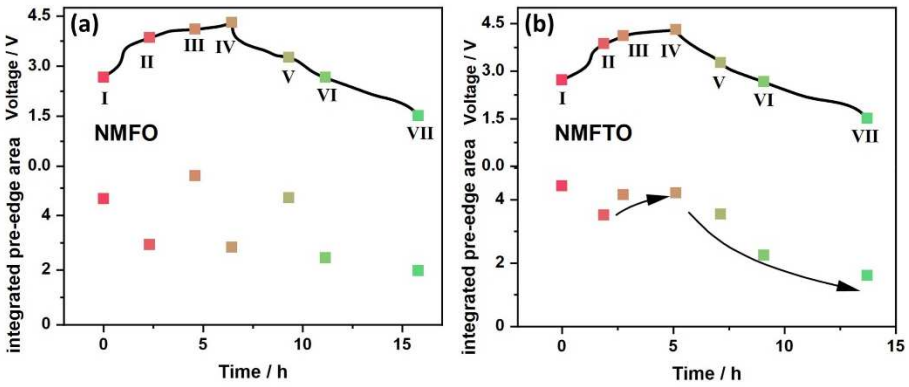

Figure 4.31. The variation of the integrated intensity of (a) NMFO (the shadow region of Figure 4.30d) and (b) NMFTO (the shadow region of Figure 4.30h).

Galvanostatic intermittent titration technique (GITT) is used to estimate the diffusion coefficient of Na^+ and thus to verify the fact that Ti substitution enhances the transport channels. Figures 4.32a and 4.32b show the details of the GITT measurement during charging and discharging of NMFO. GITT tests are performed with a 0.5 h current pulse at C/20 followed by 5 h relaxation for every step and the results are shown in Figures 4.32c (NMFO) and 4.32d (NMFTO). The overall charge/discharge capacities obtained during this GITT measurements show no big differences between the two samples. However, the voltage plateau of NMFTO is suppressed, which can be explained by Mn/Ti-substitution delaying the phase transition. The normalized quantity $D_s S^2/V_m^2$ was used to represent the change in Na mobility because it is challenging to get the exact values for the molar volume and the active surface area, as shown in Figures 4.32e (charging) and 4.32f (discharging). Compared with NMFO, the substituted NMFTO shows higher $D_s S^2/V_m^2$ values both during charging and discharging, which indicates a higher Na^+ mobility induced by Mn/Ti substitution[142].

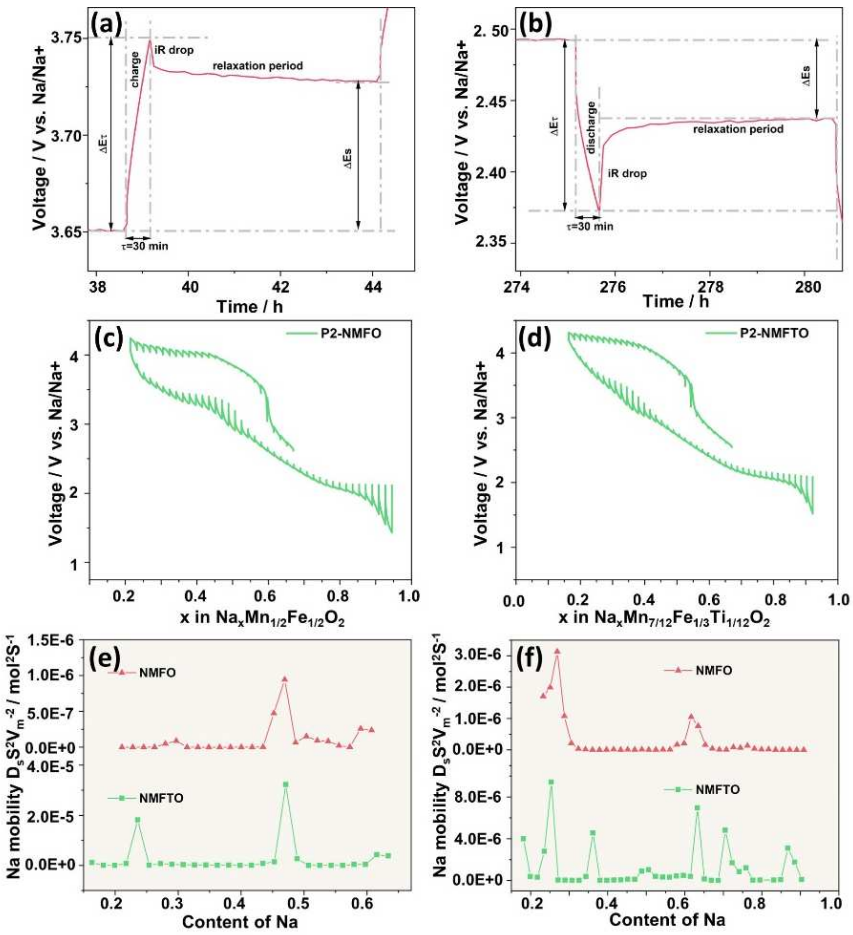

Figure 4.32. GITT measurement during (a) charging and (b) discharging of NMFO. GITT curves of P2-type cathode materials (c) NMFO and (d) NMFTO. The calculated diffusion coefficient of Na^+ at different voltages during (e) charging and (f) discharging.

4.2.3. Conclusion

In summary, we have investigated the redox reactions of transition metals and oxygen to explain the mechanism of the electrochemical performance of P2-type Mn/Fe based layered cathodes. We introduce P2-NMFTO as the cathode to overcome short cycle life and poor rate capability caused by the phase changes at high potentials and the Jahn-Teller effect at low potentials, which are both related to Mn oxidation/reduction. The partial substitution of Fe by Mn and Ti has been done to explore and optimize the mechanism of redox activity of these P2-type Mn/Fe based layered cathodes without phase changes. The Mn substitution suppresses the phase transition from P2-type to Z-type at high voltages. At the same time, Ti substitution in NMFO

can suppress the formation of the P2' phase at low voltages, thus improving the capacity retention during cycling and increasing the structural stability in the wider voltage window from 1.5 to 4.5 V.

4.3 Insights into different structure types of iron- and manganese-based layered sodium cathodes

4.3.1 Introduction

Sodium-ion batteries (SIB) are an emerging secondary battery technology for grid-scale energy storage owing to the natural-abundant sodium resources and similar working principle to the lithium-ion batteries (LIBs) during cycling[16, 143]. To meet the large demand for electricity generated from Na-ion batteries, it is necessary to develop suitable cathodes with high reversibility and rate capability. Layered transition metal oxides Na_xTMO_2 (TM = 3d transition metals) are attractive due to their promising electrochemical properties, high average working voltage and facile processability[12]. According to the coordination environment of Na cations, Na_xTMO_2 can be classified to P type which represents trigonal prismatic sites of sodium ions and O type which represents octahedral sites of sodium ions. Depending on the stacking order of oxygen layers (ABCABC, ABAB, ABBCCA), the layered oxides are mainly categorized into O3, P2, P3[144, 145]. The number following the sodium coordination environment means the number of TMO_2 layers in the unit cell. Compared with the O3-type structure, the Na ions deficiency in P-type cathodes results in fast Na^+ migration and higher sodium intercalation voltage due to the lower diffusion barriers associated with prismatic sites of Na ions. In terms of P-type materials, different calcination temperature leads to the generation of various layered structures. A low temperature (around 700 ^oC)[146] favors the formation of the P3 structure, whereas the P2 structure is synthesized by high-temperature calcination (around 900 °C), revealing that less energy consumed for the synthesis of the P3-type cathode. The P3-type compounds initially demonstrate a high capacity similar to that of the P2-type products. However, the long-term capacity retention of P3-type compounds is consistently lower than that of P2-type compounds, primarily attributed to their lower crystallinity[147].

P3-type compounds experience phase transitions from the P3 phase to either the O3 phase or the P3' phase, both of which exhibit an octahedral environment in the Na layers[148, 149]. The presence of structural disorder results in limited cycling stability and rate performance due to a significant reduction in interlayer spacing and the accumulation of carbonate species on the cathode surface[149]. Co-free P3-$Na_{0.67}Mn_{0.67}Ni_{0.33}O_2$ delivers a high initial discharge capacity of 233 mAh g^{-1} in the voltage window 1.5-4.5 V, while the capacity drops fast during cycling which was ascribed to the ordered arrangement of TM ions[150]. Despite the challenges mentioned earlier, the initial high capacity exhibited by P3-type compounds remains enticing. Therefore, further efforts are necessary to enhance the electrode performance by addressing the aforementioned issues. In chapter 2, we described the electrochemical mechanism of the layered cathode material P2-NMFTO by exploring the redox processes of transition metal cations and oxygen anions upon cycling with single-phase reaction. Herein, we synthesized P2-, P2/P3-, and P3-type NMFTO successfully by a solid-state method using same precursors for all three samples. By comparing the electrochemical performance of these three types of materials, P3-NMFTO has better retention at higher rate and in a large potential range, and it delivers 181 mAh g^{-1} at 0.1 C rate and a capacity retention of 85% after 50 cycles in the voltage window of 1.5-4.3 V, and 186 mAh g^{-1} at 0.1 C rate and a capacity retention of 82% after 30 cycles in the voltage window of 1.5-4.5 V. Moreover, the capacity retention of P3-NMFTO at faster cycling with 1 C rate is 77% after 300 cycles.

We explore the electrochemical mechanism of redox activity of P3-type NMFTO to explain the better electrochemical performance. The pair distribution function (PDF) patterns obtained from X-ray scatting are used to determine the interatomic distances, atomic coordination number, and scattering power of elements of P2- and P3-type NMFTO. *In situ* synchrotron radiation diffraction (SRD) reveals the phase transitions P3 → O3 for P3-NMFTO during cycling, while P2-NMFTO exhibits a single-phase reaction during cycling. *Ex situ* ^{23}Na nuclear

magnetic resonance (NMR) spectroscopy of P3-NMFTO acquired after charging/discharging to different voltages during the first cycle were performed to investigate the changes in the Na environments. *Ex situ* ^{23}Na NMR spectroscopy of P2-, P2/P3- and P3-NMFTO were also performed at pristine state, fully charged state at 4.5 V and fully discharged state at 1.5 V to investigate the electronic structure difference of different types of materials at high voltages. *In situ* ^{57}Fe Mössbauer spectroscopy and *in situ* X-ray absorption spectroscopy (XAS) of P3-NMFTO are used to characterize the reversible oxidation of Fe^{3+} to Fe^{4+} in the voltage window of 1.5-4.3 V. The oxidation of Mn is also observed by *in situ* XAS. To further explore the redox activity of Fe and Mn of different types of materials, *ex situ* XAS was performed in the pristine state, fully charged state at 4.5 V and fully discharged state at 1.5. *Ex situ* soft XAS of P3-type are performed to investigate the participation of oxygen anions during electrochemical cycling in the voltage windows of 1.5-4.3 V and 1.5-4.5 V.

4.3.2 Results and discussion

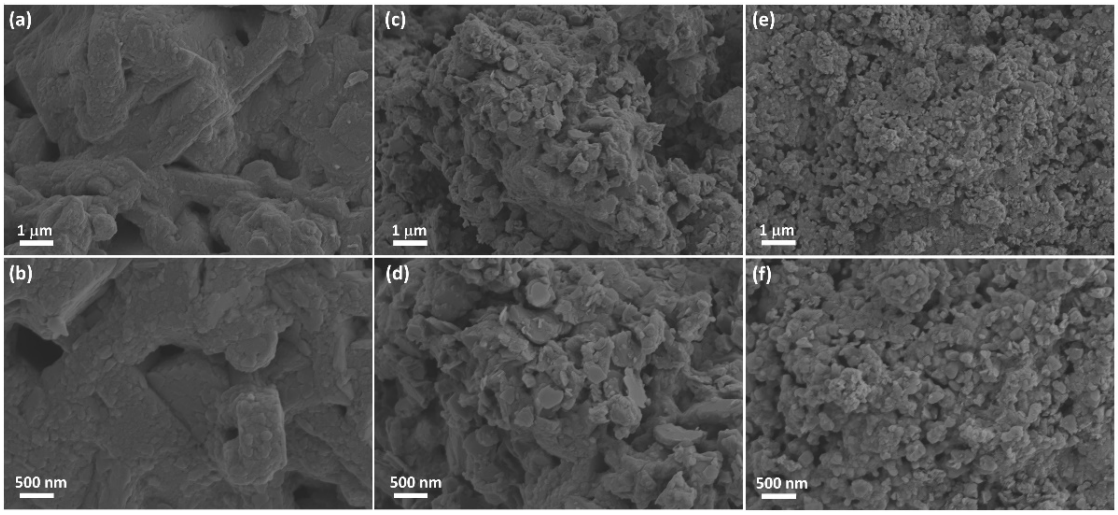

Figure 4.33. SEM images of pristine (a-b) P2-type NMFTO; (c-d) P2/P3-type NMFTO; (e-f) P3-type NMFTO.

Different types of NMFTO were successfully synthesized by solid-state reaction at different temperatures. Figure 4.33 shows the scanning electron microscopy (SEM) images of three materials which were synthesized at different temperatures. P2-NMFTO (Figure 4.33a-b) has the largest particle size and large agglomerates, while P3-NMFTO (Figure 4.33e-f) has the

smallest size of 200 nm. The particle size of P2/P3-NMFTO (Figure 4.33c-d) is around 400-500 nm, which is between those of P2- and P3-NMFTO. The size changes observed for the different types of materials illustrate that the temperature has an effect on the morphologies of these materials.

As shown in Figure 4.34a and 4.34b, the refinements against the XRD patterns of P2-type and P2/P3-type NMFTO fit very well to the observed data. For P2-NMFTO, the unit cell parameters are a = b = 2.9230(1) Å, c = 11.2289(9) Å and V = 83.109(8) $Å^3$. In the case of P2/P3-NMFTO, the lattice parameters of the P2 phase are a = b = 2.8927(0) Å, c = 11.1709(33) Å and V=80.935(23) $Å^3$ and those of the P3 phase are a = b = 2.9053(0) Å, c = 16.7748(6) Å and V=122.623(89) $Å^3$. The XRD pattern of P3-type NMFTO (Figure 4.34c) shows that all reflections are indexed to a rhombohedral lattice with space group $R3m$[110, 151]. For P3-NMFTO, the unit cell parameters are a = b = 2.9089(1) Å, c = 16.8860(29) Å and V=123.738(24) $Å^3$. The received crystallographic characteristics for these three materials are given in Tables 4.5-4.7.

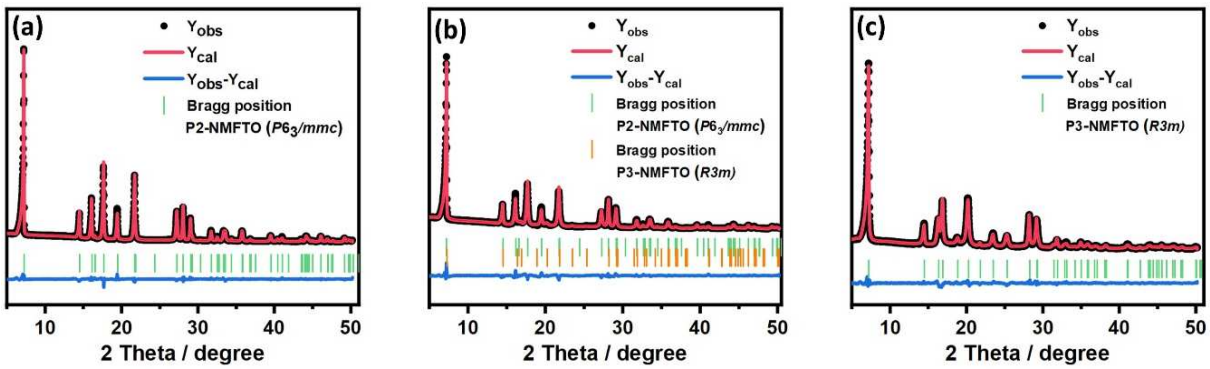

Figure 4.34. Rietveld refinement based on XRD diffraction of (a) P2-type NMFTO, (b) P2/P3-type NMFTO, and (c) P3-type NMFTO cathode materials.

Table 4.5 Detailed structural information of P2-NMFTO

NMFTO space group: *P6₃/mmc*			**R_p= 4.40%**		**R_{wp}=5.65%**	
a = b = 2.9230(1) (Å)			**c = 11.2289(9) (Å)**		**V=83.109(8) ($Å^3$)**	
Atom	**Wyckoff position**	**x**	**y**	**z**	**Occupancy**	**U**

Na1	**2b**	**0.00000**	**0.00000**	**0.25000**	**0.250**	**0.047**
Na2	**2d**	**0.33333**	**0.66667**	**0.75000**	**0.420**	**0.058**
Mn	**2a**	**0.00000**	**0.00000**	**0.00000**	**0.583**	**0.008**
Fe	**2a**	**0.00000**	**0.00000**	**0.00000**	**0.333**	**0.008**
Ti	**2a**	**0.00000**	**0.00000**	**0.00000**	**0.083**	**0.008**
O	**4f**	**0.33333**	**0.66667**	**0.08910**	**1.000**	**0.006**

Table 4.6 Detailed structural information of P2/P3-NMFTO (P2:92%; P3:8%)

NMFTO space group: *P6$_3$/mmc*			**R_p= 4.22%**		**R_{wp}=5.74%**	
a = b = 2.8927(0) (Å)			**c = 11.1709(33) (Å)**		**V=80.935(23) (Å^3)**	
Atom	**Wyckoff position**	**x**	**y**	**z**	**Occupancy**	**U**
Na1	**2b**	**0.00000**	**0.00000**	**0.25000**	**0.250**	**0.035**
Na2	**2d**	**0.33333**	**0.66667**	**0.75000**	**0.420**	**0.070**
Mn	**2a**	**0.00000**	**0.00000**	**0.00000**	**0.583**	**0.008**
Fe	**2a**	**0.00000**	**0.00000**	**0.00000**	**0.333**	**0.008**
Ti	**2a**	**0.00000**	**0.00000**	**0.00000**	**0.083**	**0.008**
O	**4f**	**0.33333**	**0.66667**	**0.08720**	**1.000**	**0.004**

NMFTO space group: *R3m*			**R_p= 4.22%**		**R_{wp}=5.74%**	
a = b = 2.9053(0) (Å)			**c = 16.7748(6) (Å)**		**V=122.623(89) (Å^3)**	
Atom	**Wyckoff position**	**x**	**y**	**z**	**Occupancy**	**U**
O1	**3a**	**0.00000**	**0.00000**	**0.39431**	**1.000**	**0.011**
Na2	**3a**	**0.00000**	**0.00000**	**0.81899**	**0.420**	**0.011**
Mn	**3a**	**0.00000**	**0.00000**	**0.00000**	**0.583**	**0.011**
Fe	**3a**	**0.00000**	**0.00000**	**0.00000**	**0.333**	**0.011**
Ti	**3a**	**0.00000**	**0.00000**	**0.00000**	**0.083**	**0.011**

Na1	**3a**	**0.00000**	**0.00000**	**0.10777**	**0.250**	**0.011**
O2	**3a**	**0.00000**	**0.00000**	**0.06472**	**1.000**	**0.011**

Table 4.7 Detailed structural information of P3-NMFTO

NMFTO space group: *R3m*		**R_p= 3.82%**		**R_{wp}=5.10%**		
a = b = 2.9089(1) (Å)		**c = 16.8860(29) (Å)**		**V=123.738(24) (Å^3)**		
Atom	**Wyckoff position**	**x**	**y**	**z**	**Occupancy**	**U**
O1	**3a**	**0.00000**	**0.00000**	**0.40135**	**1.000**	**0.011**
Na2	**3a**	**0.00000**	**0.00000**	**0.81801**	**0.420**	**0.011**
Mn	**3a**	**0.00000**	**0.00000**	**0.00000**	**0.583**	**0.011**
Fe	**3a**	**0.00000**	**0.00000**	**0.00000**	**0.333**	**0.011**
Ti	**3a**	**0.00000**	**0.00000**	**0.00000**	**0.083**	**0.011**
Na1	**3a**	**0.00000**	**0.00000**	**0.10968**	**0.250**	**0.011**
O2	**3a**	**0.00000**	**0.00000**	**0.062350**	**1.000**	**0.011**

A pair distribution function (PDF) analysis[152] was conducted via X-ray scattering data to further figure out the differences in local structure between P2 and P3-type NMFTO (Figure 4.35a). The peak positions in the PDF patterns show the interatomic distances in the layered structure. The intensity of the PDF peaks illustrates atomic coordination number, scattering power of elements. Compared to P2-NMFTO, the interatomic distances associated with TM-O correlations (d1 and d3) in P3-NMFTO are smaller. Furthermore, the peak intensities of d1 of P3-NMFTO is higher than that of P2-NMFTO. Moreover, the interatomic distance of TM-TM correlations (d2 and d4) of P3-NMFTO are also smaller than those in P2-NMFTO. Meanwhile, the peak intensity of the nearest (d2) TM-TM correlation of P3-NMFTO is higher than that of P2-NMFTO. However, the biggest difference in the patterns of P2- and P3-NMFTO is the correlation peak representing the Na-O distance. For P2-NMFTO, the Na-O correlation peak

(d6) shows as Na_f-O. When it comes to P3-NMFTO, both Na_f-O and Na_e-O are both shown in the PDF pattern[153]. The intensity of Na-O correlation of P2-NMFTO is much higher than that of P3-NMFTO, which is also confirmed by the theoretical PDF fitting patterns of P2 and P3 materials (Figures 4.35b and 4.35c)[154]. The structural information of P2- and P3-NMFTO has been illustrated in Figure 4.35d and 4.35e.

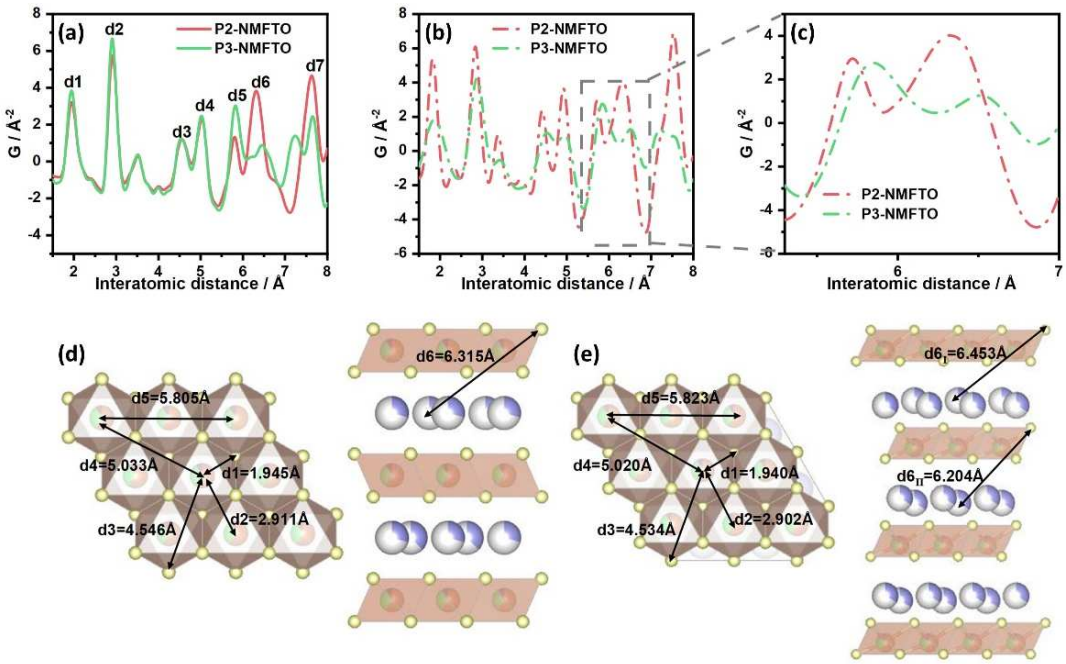

Figure 4.35. (a) PDF patterns of P2- and P3-type NMFTO; (b) PDF fitting patterns of P2- and P3-type NMFTO; (c) enlarged view of PDF fitting patterns of P2- and P3-type NMFTO. Schematic illustration of (e) P2-type NMFTO and (f) P3-type NMFTO.

The rate capability at rates between 0.05 C and 2 C of P2-, P2/P3- and P3-NMFTO are shown in Figure 4.36a, 4.36b and 4.36c. The charge/discharge curves at different rates show the capacity reduced and the polarization increased during the increasing of current density. At 2 C rate, P2-NMFTO delivers approximately 44% of its initial capacity and the discharge curves show the most obvious polarization. For P2/P3-NMFTO, the reversible capacity at 2 C rate is 48%. However, P3-NMFTO delivers 62% of the reversible capacity at 2 C rate, which confirms the high stability of P3-NMFTO.

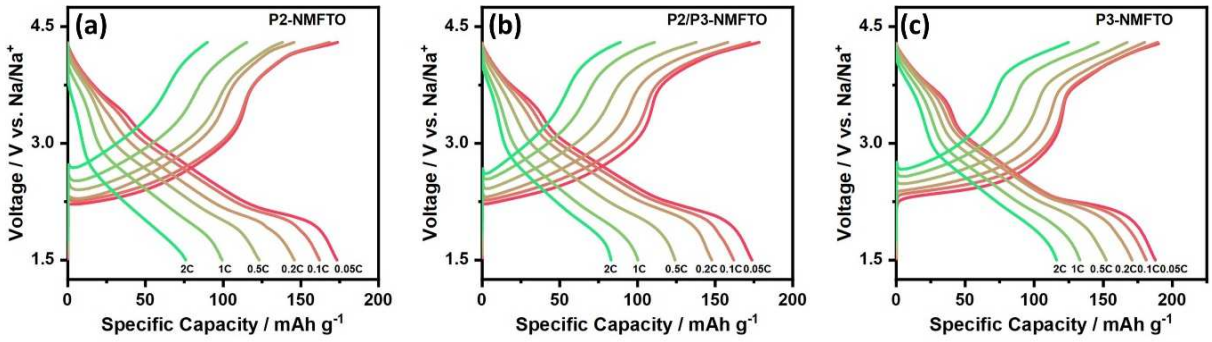

Figure 4.36 The charge/discharge curves at rates between 0.05 and 2 C of (a) P2-type, (b) P2/P3-type and (c) P3-type NMFTO.

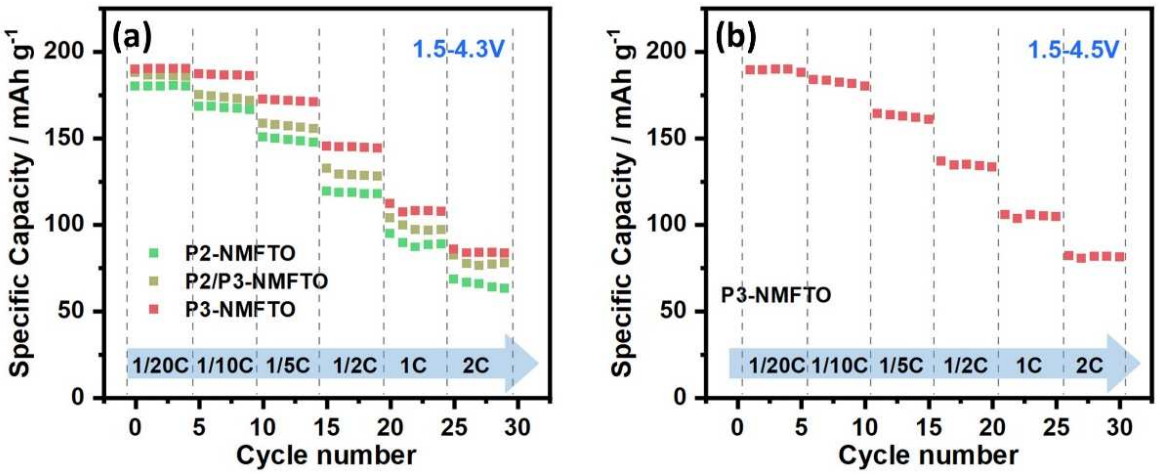

Figure 4.37 (a) Rate capability of different types NMFTO at rates between 0.05 and 2 C in the voltage window of 1.5-4.3V; (b) Rate capability of P3-NMFTO at rates between 0.05 and 2 C in the voltage window of 1.5-4.5V.

Rate capabilities of different types of NMFTO cathodes in the voltage window of 1.5-4.3 V have been examined and compared in Figure 4.37a. The capacities of P3-NMFTO are 188 mAh g^{-1}, 181 mAh g^{-1}, 171 mAh g^{-1}, 152 mAh g^{-1}, 133 mAh g^{-1} and 116 mAh g^{-1} at 0.05 C, 0.1 C, 0.2 C, 0.5 C, 1 C and 2 C. The capacity of P2/P3-NMFTO at 0.05 C is 174 mAh g^{-1} and 83 mAh g^{-1} at 2 C. For P2-NMFTO, only 76 mAh g^{-1} is maintained at 2 C, which is 66% compared to P3-NMFTO at the same rate. The change of capacity confirms that the P3-type cathode shows an attractive rate performance. The rate capabilities of P3-NMFTO cathode have also been examined (Figure 4.37b). The capacities are 190 mAh g^{-1}, 186 mAh g^{-1}, 172 mAh g^{-1}, 145 mAh g^{-1}, 116 mAh g^{-1} and 86 mAh g^{-1} at 0.05 C, 0.1 C, 0.2 C, 0.5 C, 1 C, and 2 C in the voltage

window of 1.5-4.5 V, which confirms the good rate performance of P3-NMFTO in the larger voltage window.

The cycling performance at 0.1 C in the voltage window of 1.5-4.3 V was studied to access the reversibility of the sodium storage of these three different types of cathodes, as illustrated in Figure 4.38a. The capacity retentions obtained for P2-NMFTO and P2/P3-NMFTO cathodes are 80% and 71% after 50 cycles at 0.1 C, in contrast to 84% observed for the P3-NMFTO cathode. The charge/discharge curves of the three compounds in the 1st, 30th, and 50th cycle are shown in Figures 4.39a-4.39c. The curves of P3-NMFTO show smaller polarization and high-capacity retention. The XRD patterns of the three compounds acquired after 50 cycles are shown in Figures 4.39d-4.39f. They reveal that all materials still contain the layered structure. The cycling performance was also tested in the potential range of 1.5-4.5 V to compare the stability of three materials at higher working potential, as shown in the Figure 4.38b. P3-NMFTO exhibits superior cycling stability and rate capability, with a retention of 82 % after 30 cycles. The charge/discharge curves of the three compounds in the 1st, 10th, 20th, and 30th cycle are shown in Figures 4.40a-4.40c. The curves of P3-NMFTO show smaller polarization and good capacity retention. The XRD patterns of the three compounds acquired after 30 cycles in the larger voltage window are shown in Figures 4.40d-4.40f. They reveal that all materials still contain the layered structure. The cycling performance of P3-NMFTO at 1 C in the voltage window of 1.5-4.3 V and 1.5-4.5 V is displayed in Figure 4.38c. The capacity retention of P3-NMFTO at 1 C in the voltage window of 1.5-4.3 V is 66% after 100 cycles, and 72% at 1 C in the larger voltage window of 1.5-4.5 V. This shows that P3-NMFTO has a better retention at higher rate and large potential range. The cycling performance of P3-NMFTO at 1 C in the voltage window of 2.2-4.3 V is 77% after 300 cycles (Figure 4.38d), which illustrates the good retention of P3-NMFTO during extensive cycling.

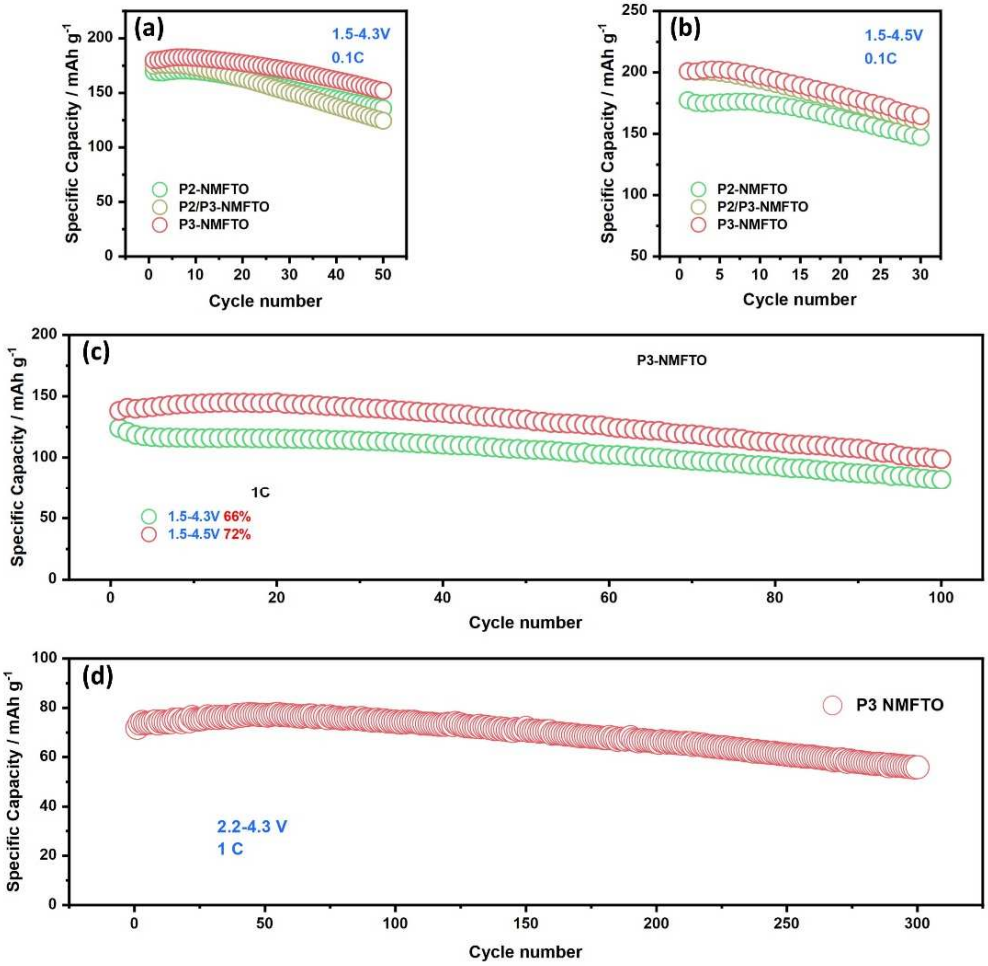

Figure 4.38 (a) Cycling performance of the three types of NMFTO at 0.1 C in the voltage window of 1.5-4.3 V; (b) cycling performance of the different types of NMFTO cathodes at 0.1 C in the voltage window of 1.5-4.5 V; (c) cycling performance of P3-type NMFTO cathode at 1 C in the voltage windows of 1.5-4.3 V and 1.5-4.5 V; (d) cycling performance of P3-type NMFTO cathode at 1 C in the voltage window of 2.2-4.3 V.

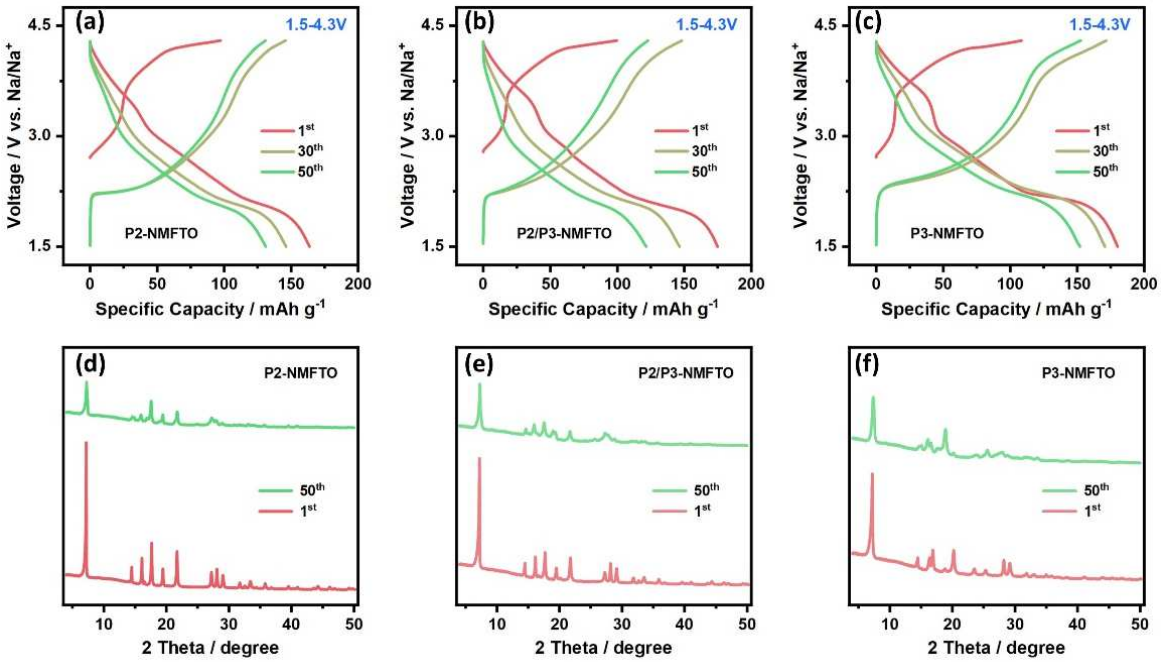

Figure 4.39 Cell voltage as a function of specific capacity of (a) P2-NMFTO, (b) P2/P3-NMFTO and (c) P3-NMFTO for the 1st, 30th, and 50th cycle at 0.1 C in the voltage window of 1.5-4.3 V; XRD patterns of (d) P2-NMFTO, (e) P2/P3-NMFTO and (f) P3-NMFTO acquired after the 1st and 50th cycle at 0.1 C in the voltage window of 1.5-4.3 V.

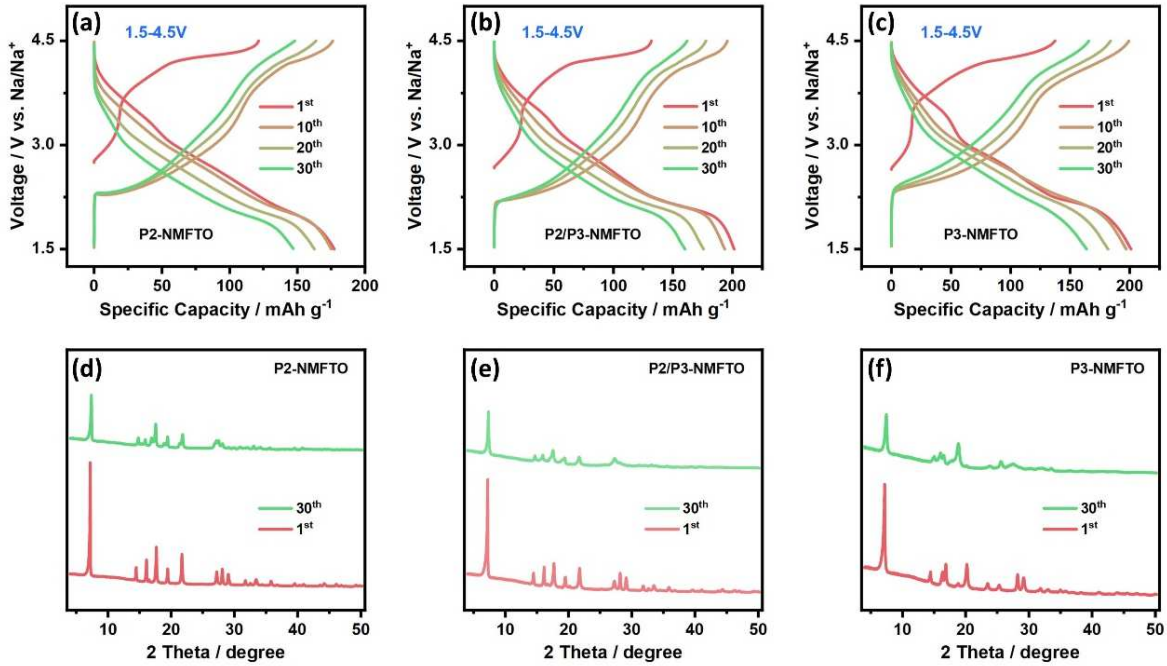

Figure 4.40 Cell voltage as a function of specific capacity of (a) P2-NMFTO, (b) P2/P3-NMFTO and (c) P3-NMFTO for the 1st, 10th, 20th, and 30th cycle at 0.1 C in the voltage window of 1.5-4.5 V; XRD patterns of (d) P2-NMFTO, (e) P2/P3-NMFTO and (f) P3-NMFTO acquires after the 1st and 30th cycles at 0.1 C in the voltage window of 1.5-4.5 V.

Figure 4.41 presents the d*Q*/d*V* result of P3-NMFTO in the potential ranges of 1.5-4.3 V and 1.5-4.5 V at a scan rate of 0.1 C. The Mn oxidation and reduction peaks are observed at around 2.8 V and 2.2 V. When the cathode is charged to higher voltages, the Fe reduction peak shows a small change (from 2.9 V to 2.8 V). Oxygen oxidation occurs at the end of the charge and the reaction at both potential ranges shows no shifts, which indicates the structural stability of P3-NMFTO even in the wider voltage window.

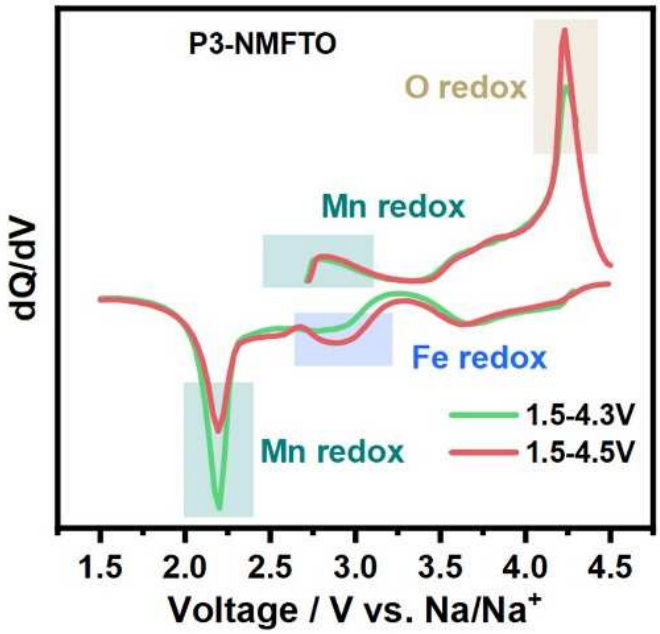

Figure 4.41 dQ/dV curves of P3-type NMFTO cathodes at 0.1 C rate in the voltage windows of 1.5-4.3 V and 1.5-4.5 V.

To explain the superior performance of P3-NMFTO, several *in situ* and *ex situ* measurements were performed to elucidate the reaction mechanism. To further explore the structural evolution of P3-NMFTO during Na^+ intercalation/deintercalation, *in situ* SRD was applied at 0.1 C rate in the cell voltage range of 1.5-4.3V, as shown in Figure 4.40a. From the open circuit voltage (OCV) to 4.17 V, the 003 and 006 reflections shift to lower angles reflecting a gradual expansion of interlayer spacing (Figure 4.42c). Meanwhile, the 101, 012, 015,110 and 113 reflections shift towards larger angles, which reveals a contraction of the spacing within the layer (Figure 4.42b). From 4.17 V to 4.3 V, the angles of all reflections show no obvious shift.

The Rietveld refinement against the XRD pattern of this cathode acquired after full charge position is shown in Figure 4.43. It illustrated that all reflections can be indexed with rhombohedral lattice with space group *R*3*m*. In the following discharging to 2.2 V, the 003 and 006 reflections shift back to higher angles, while the 101, 012, 015,110 and 113 reflections shifted towards lower angles and a new O3 phase starts to appear at the very end of discharge which can be clearly observed by the *in-situ* SRD patterns (Figure 4.42c).

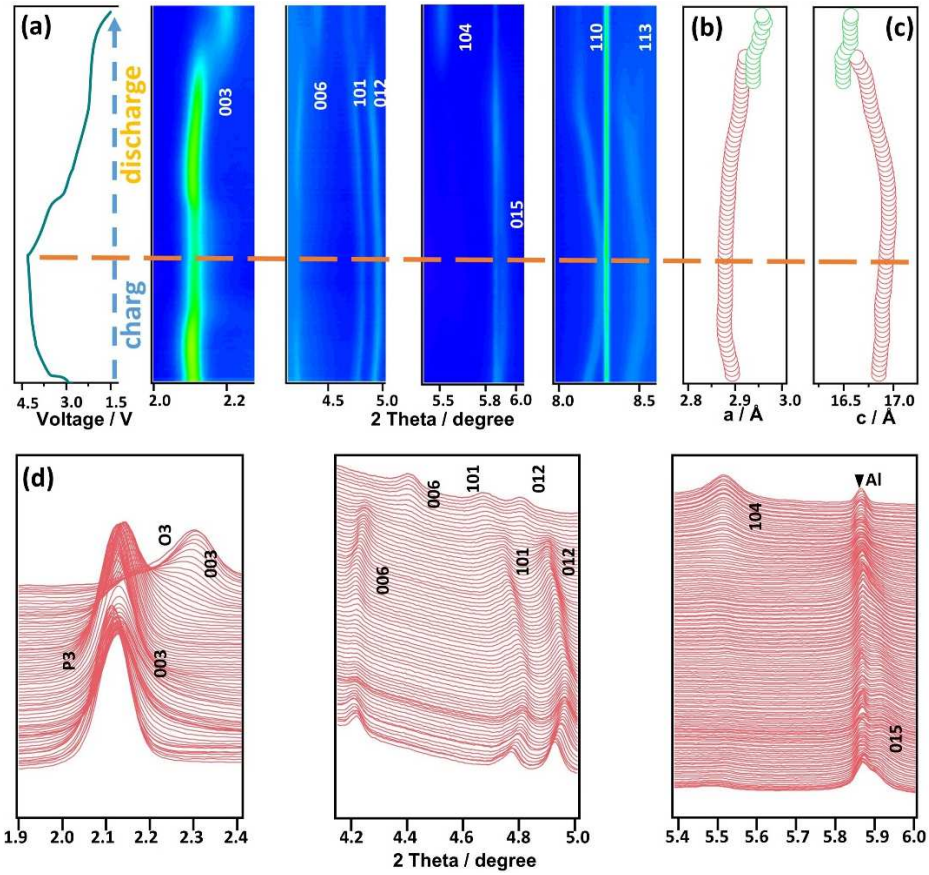

Figure 4.42 (a) Contour maps of *in situ* synchrotron diffraction of P3-NMFTO collected during the first charge/discharge process and (b, c) the corresponding lattice constants profiles at 0.1 C rate in the cell voltage range of 1.5-4.3 V; (d) *In situ* SRD patterns collected during the first charge-discharge of P3-NMFTO at 0.1 C rate in the cell voltage range of 1.5-4.3 V.

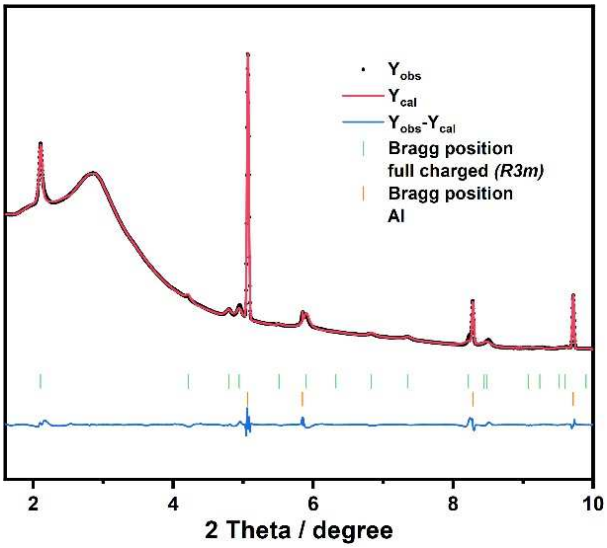

Figure 4.43 Rietveld refinement based on *in situ* SRD diffraction of P3-NMFTO cathode after full charge to 4.3 V.

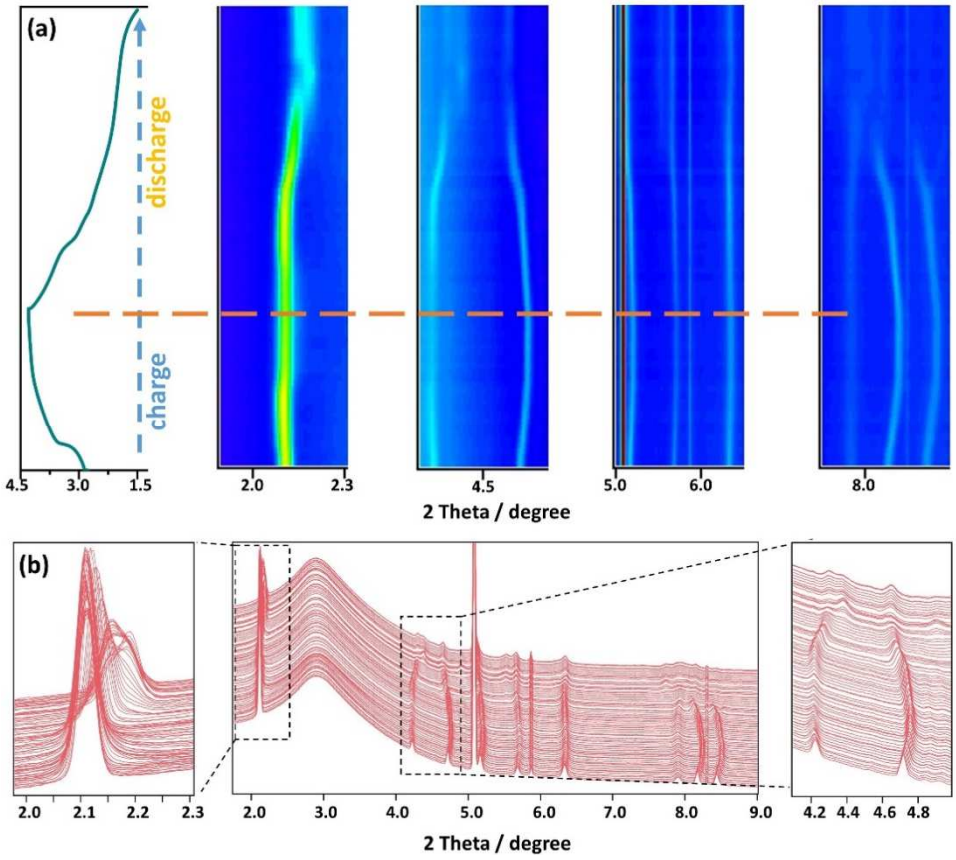

Figure 4.44. (a) Contour maps of *in situ* synchrotron diffraction of P2/P3-NMFTO collected during the first charge/discharge process. (b) *In situ* SRD patterns collected during the first charge-discharge of P3-NMFTO at 0.1 C rate in the cell voltage range 1.5-4.3 V.

As describes in chapter 4.2 (Figure 4.21), there is no phase change in P2-NMFTO during charging/discharging. *In situ* SRD measurements on P2/P3-NMFTO were applied at 0.1 C in the cell voltage range of 1.5-4.3 V as shown in Figure 4.44, and obviously a phase change can be observed at 2.25 V during the discharging period, due to the coexistence of P3-type and P2-type NMFTO cathode which exists phase change at discharging period.

To investigate the changes in local structure, *ex situ* ^{23}Na MAS NMR measurements were performed on the pristine P3-NMFTO cathode and on electrodes extracted from cells after charging/discharging to different voltages during the first cycle (Figure 4.45a). The narrow ≈ 0 ppm signal originates from diamagnetic impurities (such as Na_2CO_3 and NaF)[155-157]. A comparison of the spectra of pristine P2, P2/P3, and P3-NMFTO cathode is shown in (Figure 4.46a) revealing only one dominant resonance, and the peak positions are 1500 ppm, 1500 ppm and 1450 ppm, respectively. The spectrum of P2/P3-NMFTO is very similar to that of P2-NMFTO because of the high content of P2 phase in the pristine P2/P3 cathode. When the P3-NMFTO cathode was charged from OCV to 3.65 V, there is no obvious shift of the main resonance. After further charging to 4.3 V, the main resonance is shifted to lower values (1275 ppm) which is caused by the oxidation of high-spin Fe^{3+} (electronic configuration $3d^5$) to Fe^{4+} ($3d^4$) resulting in less unpaired electronic spins. Some residual intensity can also be observed in the fully charge state revealing that the P3-NMFTO is not completely desodiated by charging to 4.3 V. Therefore, the ^{23}Na NMR measurements were also performed on the different types of NMFTO cathodes after charging to 4.5 (Figure 4.46b). As can be seen in the spectra, the main resonance can only be observed in P3-NMFTO. P3-NMFTO is not fully desodiated and can be charged to a higher voltage in comparison to P2- and P2/P3-NMFTO. During discharging, the main ^{23}Na resonance of P3-NMFTO shifts back to higher ppm values due to the reduction of Mn^{4+} ($3d^3$) to low-spin Mn^{3+} ($3d^4$) (Figure 4.45b). When P3-NMFTO is further discharged to 2.2 V, the ^{23}Na signal becomes very broad and almost invisible. As shown above via *in situ* SRD, the O3 phase starts to appear at around 2.2 V, which means that local distortions

around Mn occur which can reduce the mobility of Na^+ but can also result in strong broadening of the NMR signal beyond detectability. The evolution of the ^{23}Na NMR spectra during this complete cycle clearly shows that after the full discharge the cathode material is reduced to a state beyond the pristine state, as also expected from the voltage profile, i.e., after the reversible changes observed in the spectra, an additional reduction of the material is observed associated with a sodiation above the initial Na content of 0.67. The ^{23}Na NMR measurements of three types NMFTO were also performed at the fully discharged state after cycling in the larger voltage window 1.5-4.5 V. The signals in the fully discharged state (Figure 4.46c) are very broad and not detectable.

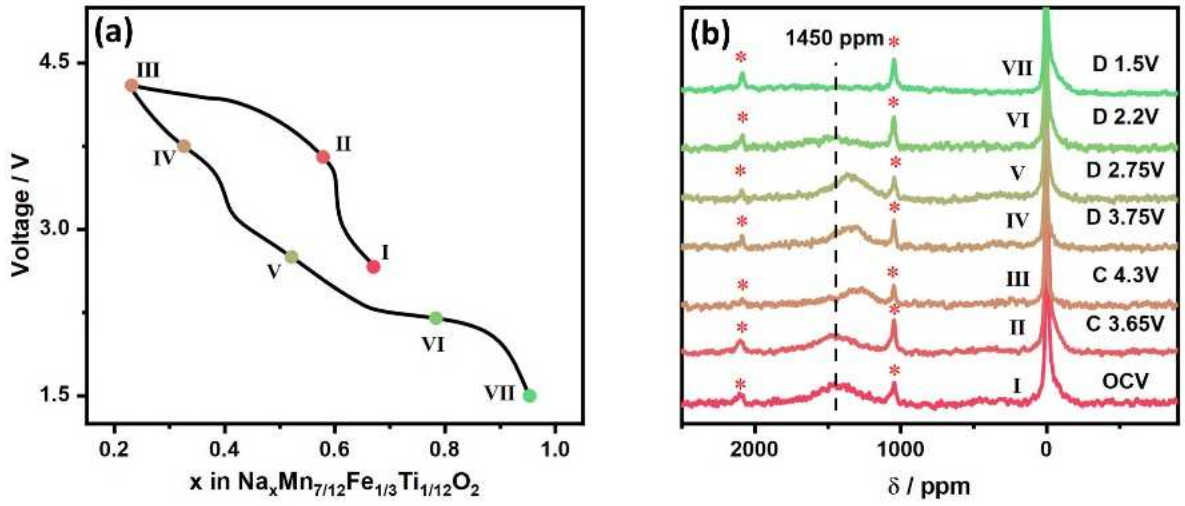

Figure 4.45 (a) Cell voltage as a function of state of charge and discharge for the first galvanostatic cycle of P3-NMFTO cells. Marked points indicate voltages where cells were disassembled for solid-state NMR measurements; (b) ^{23}Na MAS NMR spectra of P3-NMFTO cathode samples. Spinning sidebands are denoted with "*".

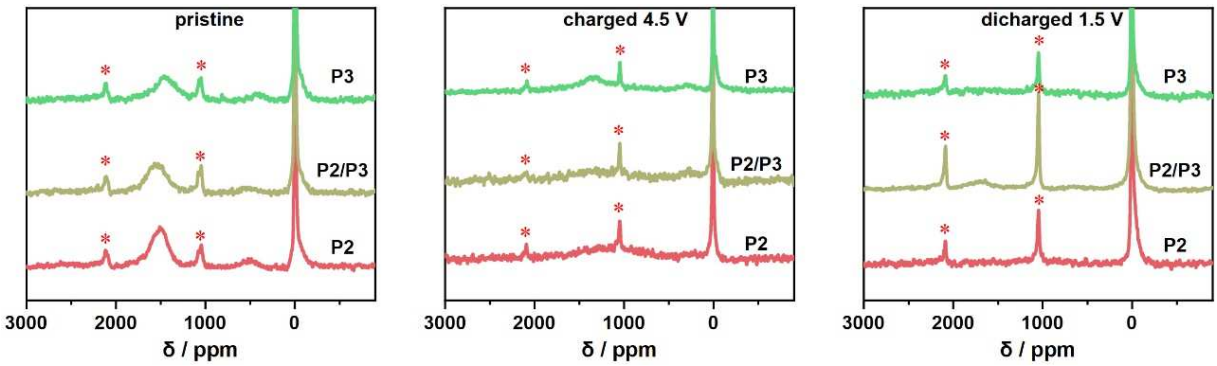

Figure 4.46 ^{23}Na MAS NMR spectra of P2-, P2/P3-, and P3-NMFTO cathode samples at different voltages (a) pristine; (b) fully charged to 4.5 V; (c) fully discharged to 1.5 V. Spinning sidebands are denoted with "*".

The change of Fe oxidation state during the cycling of P3-NMFTO was investigated by *in situ* ^{57}Fe Mössbauer spectroscopy as shown in Figure 4.47. The voltage profiles in the voltage range of 1.5-4.3 V and contour plots of *in situ* ^{57}Fe Mössbauer spectra acquired every 2 h are shown in Figure 4.47a. As can be seen from the contour plots, a new component appears in the spectra with negative isomer shift that can be assigned to Fe^{4+} [137]. The spectrum of the pristine material (Figure 4.45b) exhibits a single sharp doublet with an isomer shift (IS) around ~0.24 mm s^{-1} consistent with Fe^{3+} in high-spin state and in an octahedral environment of oxygen. The quadrupolar splitting (QS) of P3-NMFTO is around 0.81 mm s^{-1}, which is larger than that of P2-NMFTO (see section chapter 4.2), revealing a less symmetric environment. The spectra in the fully charged state at 4.3 V (Figure 4.47c) were fitted using two doublets. The first component is ascribed to Fe^{3+} in an octahedral environment with isomer shift IS very similar to that of the pristine material while the quadrupole splitting QS is larger compared to the pristine material, revealing local distortions of the octahedral environment around Fe. The second doublet with negative isomer shifts clearly reveals the existence of Fe^{4+}, which can also be seen from the negative isomer shift observed in the contour plot. All Fe^{4+} is reduced back to Fe^{3+} during discharging which is confirmed by the spectra in the discharged state (Figure 4.47d). The IS and QS values after one fully cycle are almost the same as those of the pristine material.

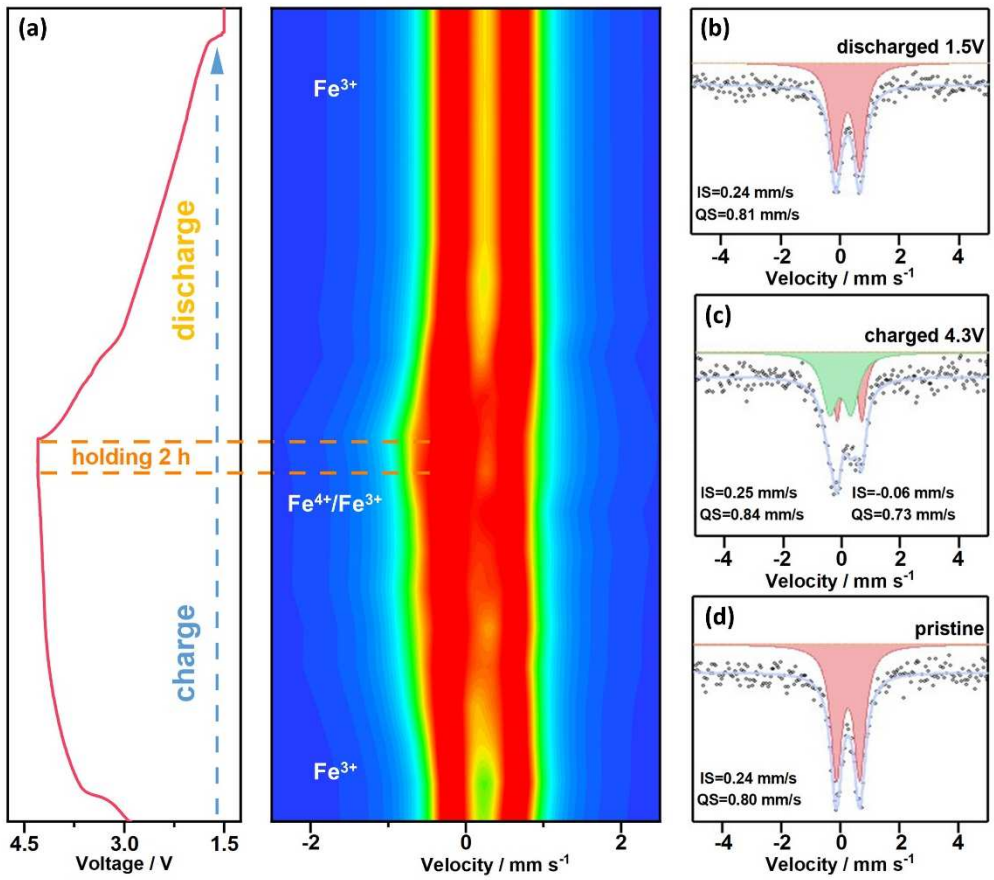

Figure 4.47 Voltage profiles and contour plots of *in situ* ^{57}Fe Mössbauer spectroscopy on P3- NMFTO during cycling between 1.5-4.3 V at a rate of 0.05 C. ^{57}Fe Mössbauer spectra of P3-NMFTO (b) in the pristine state, (c) after charging to 4.3 V, and (e) after discharging to 1.5V. The experimental data points are shown as black spheres, the overall fit as purple line. Fe^{3+} and Fe^{4+} subspectra are shown as red and green doublets, respectively.

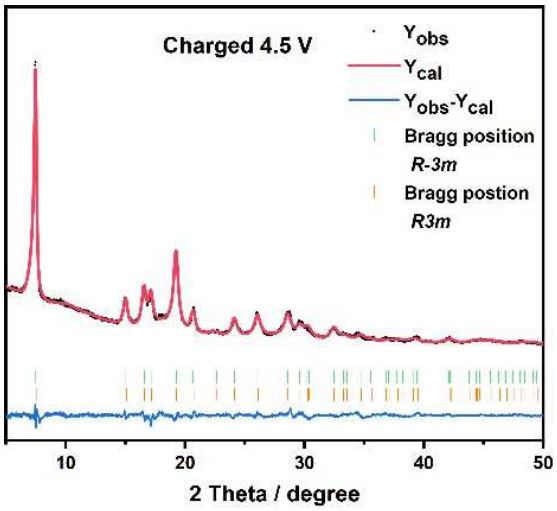

Figure 4.48 Rietveld refinement based on the XRD pattern of a P3-NMFTO cathode charged to 4.5 V.

As mentioned in Figure 4.43, the XRD pattern of the cathode acquired after full charge to 4.3 V can be indexed with rhombohedral lattice with space group *R*3*m* and the Mössbauer spectrum of the fully charged material at 4.3 V (Figure 4.47c) was fitted using two doublets. The Rietveld refinement against the XRD pattern of the cathode acquired after charging to 4.5 V is shown in Figure 4.48. All diffractions can be indexed to space group *R*-3*m* and *R*3*m*. The spectrum of the material charged to 4.5 V (Figure 4.49) was fitted using three doublets. The fitting parameters are listed in Table 4.8. The first component is ascribed to Fe^{3+}(1) with an isomer shift of 0.24 mm s^{-1} and a large quadrupolar splitting of 1.15 mm s^{-1}. This component is assigned to the appearing of O3 phase. The second component is Fe^{3+}(2) with an isomer shift of 0.23 mm s^{-1} and a small quadrupolar splitting of 0.66 mm s^{-1}. Compared to the spectrum obtained in the fully charged state at 4.3 V, the spectrum in the fully charged state at 4.5 V contains two Fe^{3+} components because of the existence of biphasic O3/P3 NMFTO. The third component with a negative isomer shift of -0.2 mm s^{-1} and a quadrupolar splitting of 0.85 mm s^{-1} is consistent with $Fe^{4+}O_6$ in layered sodium oxides[158]. The fraction of Fe^{4+} at 4.5 V is smaller than the fraction at 4.3 V, which means that Fe starts to reduce beyond 4.3 V.

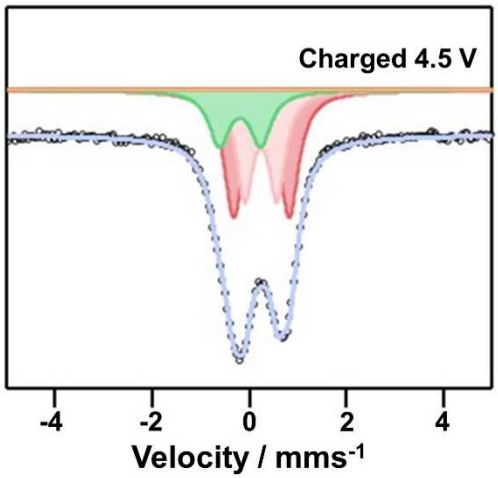

Figure 4.49 ^{57}Fe Mössbauer spectroscopy of P3-NMFTO after charging to 4.5 V. The experimental data points are shown as black spheres and the overall fit as purple line. Fe^{3+} are shown as red and light pink, Fe^{4+} as green doublet.

Table 4.8 Parameters from fitting of ^{57}Fe Mössbauer spectroscopy of P3-NMFTO cathode charged at 4.5 V.

Component	IS / mm s^{-1}	QS / mm s^{-1}	Area fraction/%
Fe^{3+}(1)	0.24	1.15	45.2
Fe^{3+}(2)	0.23	0.66	33.5
Fe^{4+}	-0.20	0.85	21.3

In situ XAS was performed to explore the electronic structure and local environments of manganese and iron in P3-NMFTO during the first cycle in the voltage window of 1.5-4.3 V. As has been shown via Mössbauer spectroscopy (Figure 4.47b), the oxidation state of Fe in the pristine state is 3+. The Fe K absorption edge shifts towards higher energy throughout the whole charging process, revealing the steady electron removal continuously from Fe^{3+} to Fe^{4+} (Figure 4.50a) and shifts back to lower energy during the discharge process (Figure 4.50b) which is in good agreement with the results from *in situ* ^{57}Fe Mössbauer spectroscopy described above (Figure 4.47a). *Ex situ* Fe K-edge XANES spectra of P2-, P2/P3- and P3-NMFTO at 4.3 V and 4.5 V are shown in Figures 4.51a-c. For P2-NMFTO, some additional shift is observed in the spectrum at 4.5V in comparison to that measured at 4.3 V, which might hit at further Fe oxidation above 4.3 V. For P3-NMFTO, the top part of the edge shows some left shift at 4.5 V in comparison to the spectrum measured at 4.3 V, again revealing changes in the electronic structure, in agreement with the Mössbauer spectra (Figure 4.49). The Fourier transform (FT) (k^3-weighted) of Fe K-edge EXAFS spectra of P3-NMFTO during cycling are shown in Figures 4.50c and 4.50d. Two coordination spheres exhibit prominent signals, with the first sphere depicting the coordination of Fe and neighboring O atoms. The second coordination sphere represented by the peak near 2.5 Å is mainly due to Fe-TM single scattering contributions within the TMO_2 slabs. During charging to 4.3 V, the Fe-O distance decreases continuously from 1.48 Å to 1.38 Å indicating oxidation of Fe^{3+} to higher oxidation states (ionic radius of Fe^{3+} in high-spin state in octahedral environment: 0.645 Å; Fe^{4+}: 0.585 Å), which can be observed in Figure 4.52a. When the electrode is then further charged to 4.5 V (Figure 4.52b), the distance increases

from 1.38 Å to 1.43 Å indicating the higher oxidation state at 4.3 V compared to 4.5 V[105]. No obvious shift can be observed for the Fe-TM peak. The Fe-O distance increases again for both samples in different voltage windows during discharging. The Fe-TM distance undergoes a slight shift from 2.50 Å to 2.47 Å upon Na extraction and returns to its initial state after discharging in the voltage window of 1.5-4.3 V. However, in the large voltage window of 1.5-4.5 V, the Fe-TM distance shows no overall shift when comparing the pristine and the fully charged state, and this peak then shows a shift from 2.50 Å to 2.56 Å during discharging.

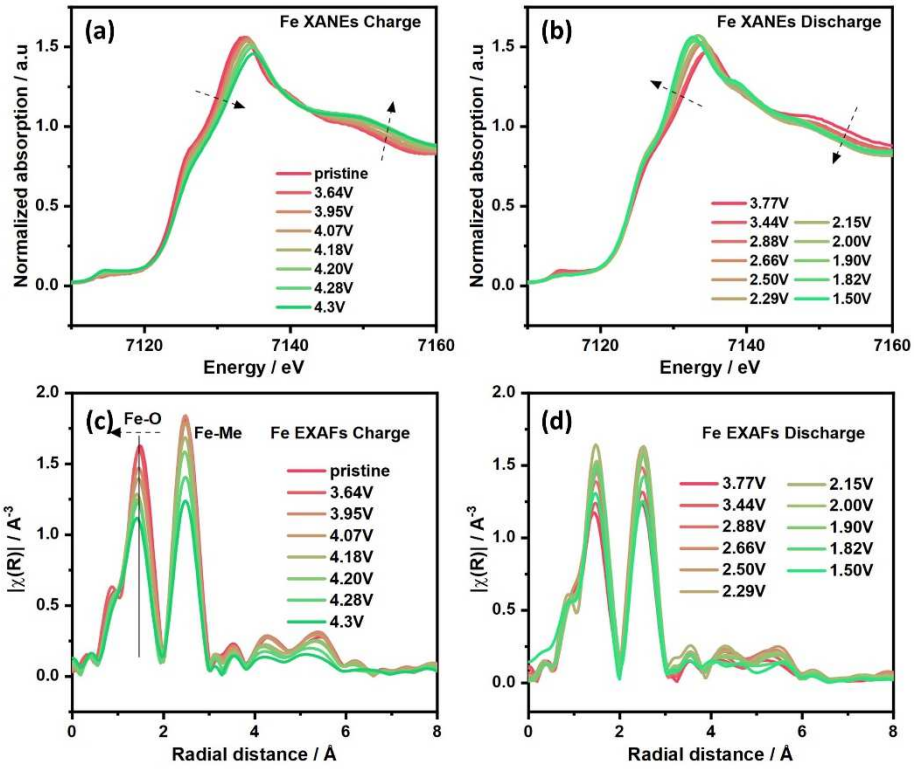

Figure 4.50. XANES spectra at Fe K-edge of P3-NMFTO acquired during charging (a) and discharging (b); Fourier transforms (k^3-weighted) of Fe K-edge EXAFS spectra of P3-NMFTO acquired during charging (c) and discharging (d).

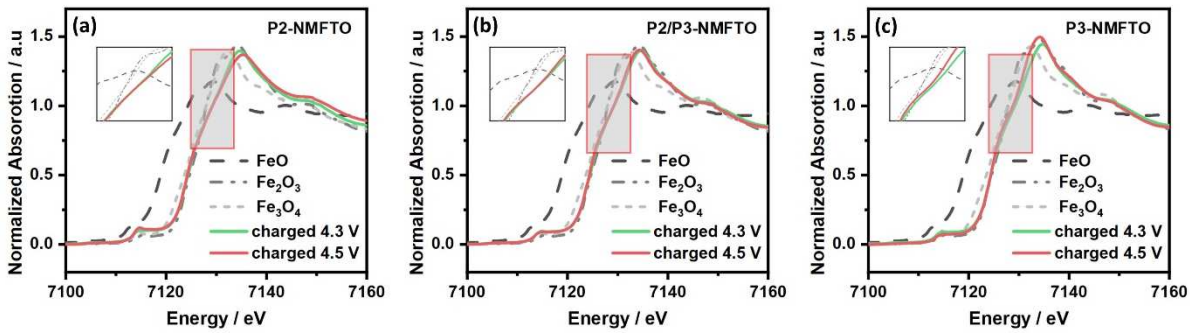

Figure 4.51 *Ex situ* Fe K-edge XANES spectra of (a) P2-, (b) P2/P3- and (c) P3-NMFTO at 4.3 V and 4.5 V.

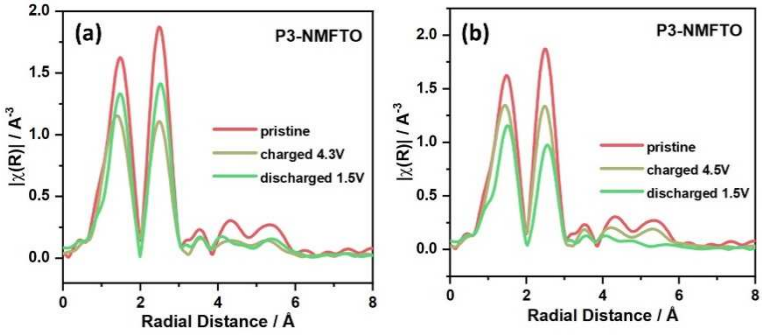

Figure 4.52 *Ex situ* Fourier transforms (k^3-weighted) of Fe K-edge EXAFS spectra of P3-NMFTO at different charge states (a)pristine, fully charged 4.3 V, and fully discharged; (b) pristine, fully charged 4.5 V, and fully discharged.

The calculated average oxidation state of Mn in pristine P3-NMFTO is +3.43. During the charge process, the Mn K-edge shows a small shift towards higher energy (Figure 4.53a), revealing some degree of oxidization of Mn. This effect is much less pronounced than that observed for Fe. However, the Mn K-edge shows a strong shift to lower energy during the whole discharge process (Figure 4.53b), revealing the continuous reduction of Mn^{4+}, clearly beyond the initial oxidation state of the pristine material. Mn K-edge XANES spectra of P2-, P2/P3- and P3-NMFTO at 4.3 V and 4.5 V are shown in Figures 4.54a-4.54c. No obvious edge shift can be observed for P2/P3-NMFTO between 4.3 V and 4.5 V. For P2-NMFTO, the edge shows a small shift to lower energy at 4.5 V. On the contrary, for P3-NNMFTO, the edge shows a small shift to higher energy at 4.5 V compared to the spectrum at 4.3 V, which illustrates that Mn is oxidized to Mn^{4+} during charging from 4.3 V to 4.5 V. Comparing the Fe and Mn K-edge XANES spectra, Fe^{3+} undergoes oxidation from OCV (open-circuit voltage) to 4.3 V, while the

reduction of Fe^{4+} starts after reaching 4.3 V. In contrast, Mn does not show redox activity before 4.3 V, and it then shows clear oxidation from 4.3 V to 4.5 V.

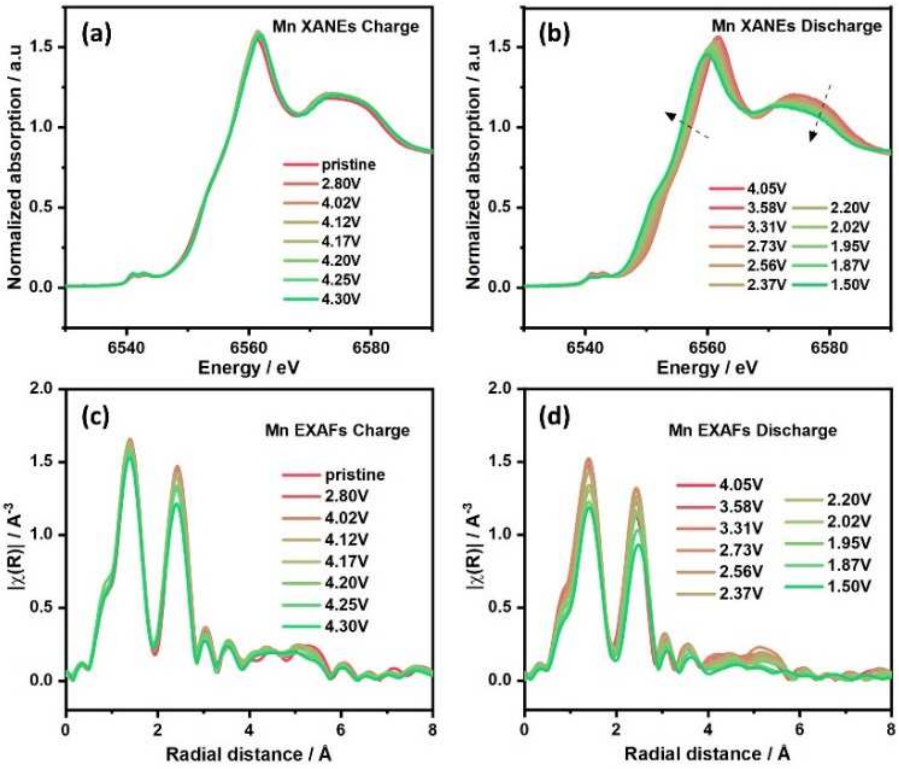

Figure 4.53 XANES spectra at Mn K-edge during charging (a) and discharging (b); Fourier transforms (k^3-weighted) of Mn K-edge EXAFS spectra of P3-NMFTO during charging (c) and discharging (d).

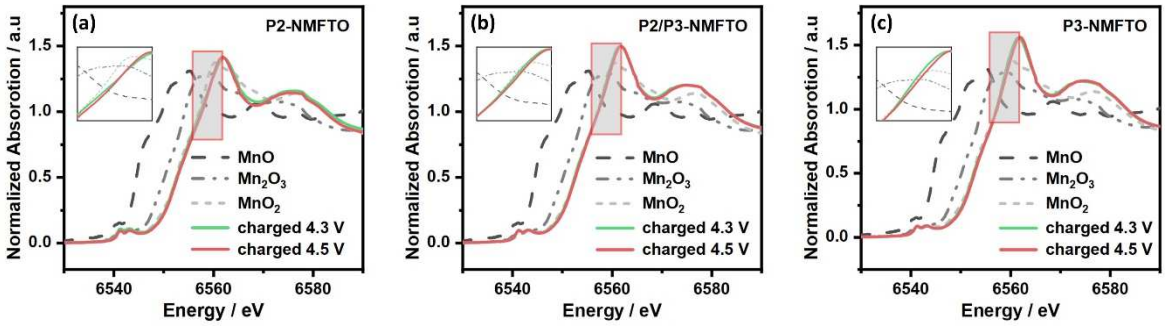

Figure 4.54 *Ex situ* Mn K-edge XANES spectra of (a) P2-, (b) P2/P3- and (c) P3-NMFTO at 4.3 V and 4.5 V.

The Fourier transforms (FT) (k^3-weighted) of Mn K-edge EXAFS spectra of P3-NMFTO during cycling are shown in Figures 4.53c and 4.53d. The radial distributions exhibit two peaks at about 1.45 and 2.45 Å, corresponding to the Mn-O distance and Mn-TM/Na distance. During the first charging to 4.3 V, the intensity of the Mn-O peak slightly decreases due to the oxygen redox process. No obvious distance shift of Mn-TM peak can be observed during the charging

period. For the first discharging period, an obvious intensity decrease of the Mn-O peak can be observed because of the reduction of Mn^{4+} to Mn^{3+} accompanied with Jahn-Teller distortions. The shift of the second Mn-TM peak to larger values indicates the increase of the Mn-TM distance. Comparing the fully charged state after cycling in the voltage windows 1.5-4.3 V or 1.5-4.3 V, which is shown in Figure 4.55, the decrease in the intensity of the Mn-O peak is more pronounced in the voltage window 1.5-4.5 V. The stronger changes of the Mn-O peak intensity indicate that more Mn is reduced to Mn^{3+} during the discharging period in the voltage window 1.5-4.5 V. This result is also in good agreement with the *ex situ* Mn K-edge XANES spectra of P3-NMFTO in fully discharged state after cycling in the voltage windows 1.5-4.3 V or 1.5-4.5 V (Figure 4.56). The spectrum in the discharged state after cycling in the voltage window 1.5-4.5 V shifts to lower energy compared to that in the discharged state after cycling in the voltage window 1.5-4.3 V, which means that more Mn^{3+} is obtained in the fully discharged state after cycling in the larger voltage window.

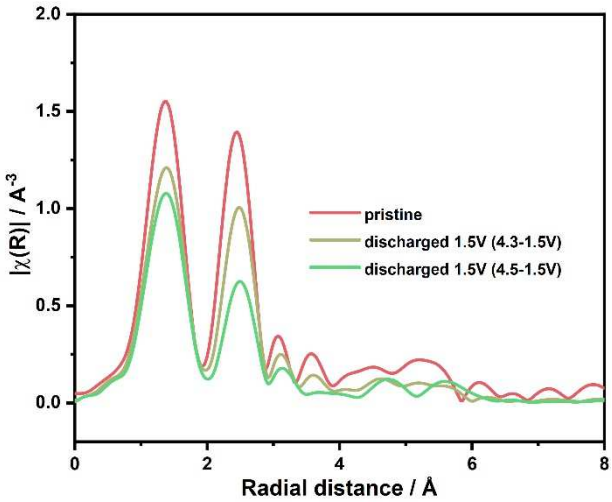

Figure 4.55 *Ex situ* Fourier transforms (k^3-weighted) of Fe K-edge EXAFS spectra of P3-NMFTO in the fully discharged state after cycling in the voltage windows 1.5-4.3 V or 1.5-4.5 V.

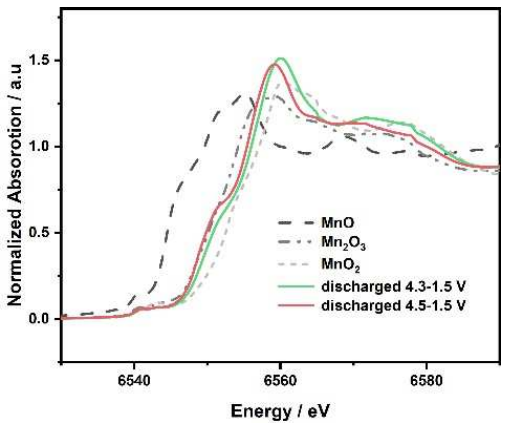

Figure 4.56 *Ex situ* Mn K-edge XANES spectra of P3-NMFTO in the fully discharged state after cycling in the voltage windows 1.5-4.3 V or 1.5-4.5 V.

Ex situ soft XAS measurements were performed on P3-NMFTO cathodes extracted from cells at different voltages during the first cycle (Figure 4.57a) to probe changes in the oxidation states and chemical environments. The O K-edge XAS spectra acquired in the fluorescence yield (FY) mode are shown in Figures 4.57b, which can be used to explain the interplay between cationic TM redox and anionic oxygen redox activity. The density of the empty bound state in the molecular energy level is related to the hybridization of metal 3d-O 2p orbitals (the pre-edge peaks below 535 eV), the variation of integrated pre-edge intensity (shadow region in Figure 4.57b) can show the hole state distribution and the effective charge on the oxygen atom[140]. The integrated intensity which reflects the changes in the density of empty states was calculated and displayed in Figure 4.57c. The result shows regular changes during the electrochemical cycling, which is relevant to electron removal from oxygen and the consequently generated holes in O 2p orbitals[141], while the jump at 2.2 V is caused by the phase change.

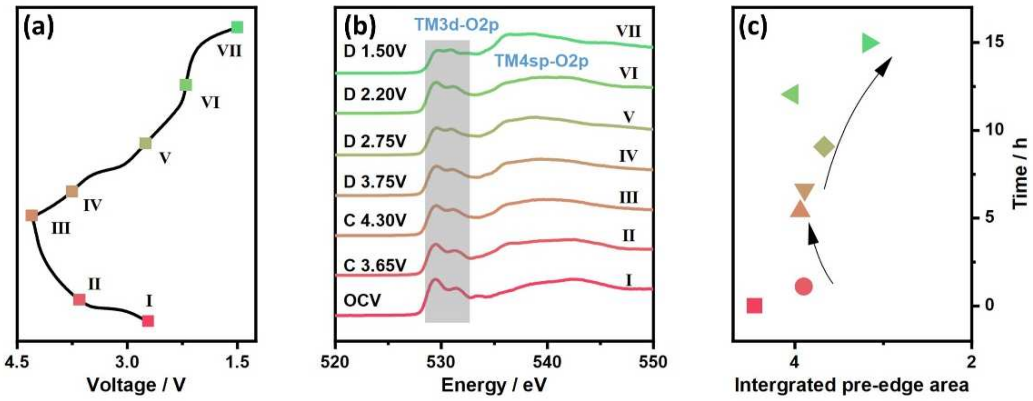

Figure 4.57 Cell voltage as a function of state of charge and discharge for the first galvanostatic cycle of (a) P3-NMFTO cells; marked points indicate voltages where cells were disassembled for soft XAS measurements; (b) O K-NEXAFS spectra of NMFO at different voltage; (c) The variation of the integrated intensity of P3-NMFTO.

4.3.3 Conclusion

We synthesized three different types of NMFTO cathodes and compared the electrochemical performance of them. The P3-NMFTO cathode delivers 190 mAh g^{-1} and 77% capacity retention after 300 cycles. We investigated the redox reactions of transition metals and oxygen to explain the mechanism of the better electrochemical performance of P3-type Mn/Fe based layered cathodes. We introduce P3-NMFTO as the cathode to overcome short cycle life and poor rate capability caused by the phase changes at high potentials and the Jahn-Teller effect occurring at low potentials, which are both related to Mn oxidation/reduction. From OCV to 4.3 V, Fe^{3+} undergoes oxidation, while the Mn oxidation occurs from 4.3 V to 4.5 V which promotes a higher charging capacity than P2- and P2/P3-NMFTO. P3-NMFTO promotes more discharging capacity in the large working voltage window and with better capacity retention at higher rate although the phase change and the Jahn-Teller distortion can be observed more clearly, which can be ascribed to the formation of robust Mn-O-Ti-O-Fe bonds within the transition metal (TM) layers in P3-NMFTO, significantly improving the stability of the overall structure. This work sheds light on how the structure affects the charging/discharging curves and electrochemical performance. These results could thus provide a reference for designing highly stable cathode materials.

Chapter 5 Conclusion and Outlook

In the present thesis, I mainly focused on the electrochemical reaction mechanism of manganese- and iron-based layered cathode material for sodium batteries with classic and well-established techniques. In the first part, *in situ* SRPD is applied to investigate the structural changes occurring during cycling of single phase P2-NMFO and O3-$NaMn_{1/2}Fe_{1/2}O_2$ which were synthesized by solid-state method. The P2-NMFO cathode exhibits subsequent phase transitions P2 → P2/Z → Z → Z/P2 → P2 → P2' during cycling, while the phase change sequence of O3-$NaMn_{1/2}Fe_{1/2}O_2$ is O3 → O3+P3 → "X" → O3+P3 → O3. The complex phase changes of P2-NMFO and O3-$NaMn_{1/2}Fe_{1/2}O_2$ have an effect on electrochemical performance, i.e. cycling stability. To improve the electrochemical performance of Mn- and Fe-based layered sodium oxides, we substituted Ti into the TM layer to form robust Mn-O-Ti-O-Fe bonds which is important to improve the stability of the overall structure. We explored the structure and electrochemical properties of layered cathode materials with different Fe, Mn, and Ti ratios in TM layers. Compared to P2-NMFO, reducing Mn content is more inclined to produce a biphasic P2/O3 material, while in most cases inactive Ti reduces the capacity of the cathode material. A Mn and Ti co-substituted P2-NMFTO material has the best electrochemical performance among all synthesized materials.

Based on the improvement of electrochemical performance of P2-NMFTO, further studies on the electrochemical reaction mechanism of the layered cathode material P2-NMFTO are performed. The partial substitution of Fe by Mn and Ti has been done to explore and optimize the mechanism of redox activity of these P2-type Mn/Fe based layered cathodes without phase changes during cycling as revealed by *in situ* SPRD. The Mn substitution suppresses the phase transition from P2-type to Z-type at high voltages. At the same time, Ti substitution in NMFO can suppress the formation of the P2' phase at low voltages, thus improving the capacity retention during cycling and increasing the structural stability in the wider voltage range from

1.5 to 4.5 V. *In situ* ^{57}Fe Mössbauer spectroscopy and *in situ* XAS are used to characterize the reversible oxidation of Fe^{3+} to Fe^{4+}. The oxidation of Mn is also observed by *in situ* XAS. Moreover, *ex situ* ^{23}Na MAS NMR spectroscopy and *ex situ* soft XAS are performed to investigate the changes in the Na environments and the participation of oxygen anions during electrochemical cycling, respectively.

Regarding the second part, P2-, P2/P3- and P3-type NMFTO three different types of cathodes were synthesized. When comparing the electrochemical performance of three types of cathodes, P3-NMFTO cathode delivers 190 mAh g^{-1} and 77% capacity retention after 300 cycles. PDF patterns show the interatomic distances, atomic coordination numbers, and scattering power of P2- and P3-type NMFTO. *In situ* SRD reveals the phase transitions P3 $\rightarrow$ O3 of P3-NMFTO during cycling. *In situ* XAS illustrates that the Fe^{3+} undergoes oxidation from OCV to 4.3V, while the Mn oxidation occurs from 4.3V to 4.5V. This promotes higher more charging capacity for P3- than for P2- and P2/P3-NMFTO. P3-NMFTO promotes higher discharging capacity in the large working voltage window (1.5-4.5 V) and with better capacity retention at higher rate although the phase change and Jahn-Teller distortion are more obviously, which can be ascribed to the formation of robust Mn-O-Ti-O-Fe bonds within the transition metal (TM) layers in P3-NMFTO, significantly improving the stability of the overall structure.

The understanding of the electrochemical reaction mechanism of Mn- and Fe-based layered cathode materials for sodium-ion batteries, especially P-type materials, provided here sheds light on how the structure affects the charging/discharging behavior and electrochemical performance. These results could provide a reference for designing highly stable cathode materials.

Acknowledgement

It was since 10/2020 when I officially started my PhD work at the Department of Chemistry and Biosciences (Karlsruhe Institute of Technology, KIT), Institute for Applied Materials - Energy Storage Systems (IAM-ESS). It's a great pleasure to thank the financial support from China Scholarship Council (CSC, No. 202008320372). Many thanks go to people who kept offering me help and conduct.

First of all, I would like to thank my supervisor Prof. Dr. Helmut Ehrenberg, who gave me the chance to do research work at IAM-ESS. I am grateful for his great support, value guidance and comments.

Next, I want to express my sincere profound thanks to my co-supervisor Dr. Sylvio Indris. I really learn a lot when we performed measurements and analyzed data together. From his understanding, encouragement, suggestion, guidance, and constant support, I gain insights and learn rich scientific knowledge.

I am grateful to Dr. Angelina Sarapulova, who contributed constructive suggestion, and feedback on my XAS experiments, and for her incredible patience and thoughtful discussion of my paper. I would also like to thank Dr. Qiang Fu, who generously took time to help me and advise me on my paper writing with high-skilled scientific suggestions. Many thanks are also given to Dr. Hang Li who helped me to perform the NMR measurement and the data analyzing and always give me suggestion. I also want to thank Dr. Weibo Hua for his beamtime. I want to thank Liuda Mereacre for providing essential support in the lab.

I would like to express thankfulness to Dr. Michael Knapp and Dr. Oleksandr Dolotko for their help and useful comments on XRD measurements and analyzing. The help from my colleagues at IAM-ESS, Dr. Xinyang Liu-Théato, Dr. Tianzhu Liu, Bijian Deng, Hao Liu, Mrs. Almut Kriese (administrative support), Mr. Udo Geckle (SEM training), Mr. Heinz-Robert Goebel

(equipment support), Mr. Luis Martin Sanchez Neudeck (IT support) are gratefully acknowledged. All colleagues working on this topic in IAM-ESS are gratefully acknowledged for their support and help during this research. In addition, I would like to thank Dr. Edmund Welter (P65 beamline at PETRA III, Hamburg) for the XAS measurements; Dr. Volodymyr Baran (P02.1 beamline at PETRA III, Hamburg) for the XRD measurements; Dr. Peter Nagel, Dr. Stefan Schuppler, Dr. Michael Merz (beamline of the KIT Light Source) for the soft XAS measurements.

Finally, my most profound gratitude goes to my parents and my brother. Their selfless and endless love give me courage and confidence to challenge and overcome all difficulties. They gave me the support and understanding to pursue my dreams. With them, my existence is valuable.

I would like to draw a full stop to my PhD journey with a Chinese slang:

“回头看，轻舟已过万重山；向前看， 前路漫漫亦灿灿”

Looking back, the light boat has passed through countless mountains. Looking forward, the road ahead is long and bright.

Reference

1. Zuo, W.; Innocenti, A.; Zarrabeitia, M.; Bresser, D.; Yang, Y.; Passerini, S., Layered Oxide Cathodes for Sodium-Ion Batteries: Storage Mechanism, Electrochemistry, and Techno-economics. *Acc. Chem. Res.* **2023,** *56* (3), 284-296.

2. Greim, P.; Solomon, A. A.; Breyer, C., Assessment of Lithium Criticality in the Global Energy Transition and Addressing Policy Gaps in Transportation. *Nat. Commun*. **2020**, 11 (1), 4570.

3. Wentker, M.; Greenwood, M.; Asaba, M. C.; Leker, J., A Raw Material Criticality and Environmental Impact Assessment of State-of-the-Art and Post-Lithium-Ion Cathode Technologies. *J. Energy Storage* **2019**, 26.

4. de la Llave, E.; Borgel, V.; Park, K. J.; Hwang, J. Y.; Sun, Y. K.; Hartmann, P.; Chesneau, F. F.; Aurbach, D., Comparison between Na-Ion and Li-Ion Cells: Understanding the Critical Role of the Cathodes Stability and the Anodes Pretreatment on the Cells Behavior. *ACS Appl. Mater. Interfaces* **2016**, 8 (3), 1867-75.

5. Rudola, A.; Rennie, A. J. R.; Heap, R.; Meysami, S. S.; Lowbridge, A.; Mazzali, F.; Sayers, R.; Wright, C. J.; Barker, J., Commercialisation of High Energy Density Sodium-Ion Batteries: Faradion's Journey and Outlook. *J. Mater. Chem. A* **2021**, 9 (13), 8279-8302.

6. Bauer, A.; Song, J.; Vail, S.; Pan, W.; Barker, J.; Lu, Y., The Scale-up and Commercialization of Nonaqueous Na-Ion Battery Technologies. *Adv. Energy Mater*. **2018**, 8 (17).

7. Liu, Q.; Hu, Z.; Chen, M.; Zou, C.; Jin, H.; Wang, S.; Chou, S. L.; Liu, Y.; Dou, S. X., The Cathode Choice for Commercialization of Sodium-Ion Batteries: Layered Transition Metal Oxides versus Prussian Blue Analogs. *Adv. Funct. Mater.* **2020,** *30* (14).

8. Liu, R.; Liang, Z.; Gong, Z.; Yang, Y., Research Progress in Multielectron Reactions in Polyanionic Materials for Sodium-Ion Batteries. *Small Methods* **2018,** *3* (4).

9. Wang, S.; Wang, L.; Zhu, Z.; Hu, Z.; Zhao, Q.; Chen, J., All Organic Sodium-Ion Batteries with $Na_4C_8H_2O_6$. *Angew. Chem. Int. Ed.* **2014,** *53* (23), 5892-6.

10. Han, M. H.; Gonzalo, E.; Singh, G.; Rojo, T., A Comprehensive Review of Sodium Layered Oxides: Powerful Cathodes for Na-Ion Batteries. *Energy & Environ. Sci.* **2015,** *8* (1), 81-102.

11. Kundu, D.; Talaie, E.; Duffort, V.; Nazar, L. F., The Emerging Chemistry of Sodium Ion Batteries for Electrochemical Energy Storage. *Angew. Chem. Int. Ed.* **2015,** *54* (11), 3431-48.

12. Sathiya, M.; Hemalatha, K.; Ramesha, K.; Tarascon, J. M.; Prakash, A. S., Synthesis, Structure, and Electrochemical Properties of the Layered Sodium Insertion Cathode Material: $NaNi_{1/3}Mn_{1/3}Co_{1/3}O_2$. *Chem. Mater.* **2012,** *24* (10), 1846-1853.

13. Delmas, C.; Fouassier, C.; Hagenmuller, P., Structural Classification and Properties of the Layered Oxides. *Physica B+C* **1980,** *99* (1-4), 81-85.

14. Delmas, C.; Braconnier, J.; Fouassier, C.; Hagenmuller, P., Electrochemical Intercalation of Sodium in Na_xCoO_2 Bronzes. *Solid State Ionics* **1981,** *3-4*, 165-169.

15. Goodenough, J. B.; Park, K. S., The Li-ion Rechargeable Battery: a Perspective. *J. Am. Chem. Soc.* **2013,** *135* (4), 1167-76.

16. Yabuuchi, N.; Kubota, K.; Dahbi, M.; Komaba, S., Research Development on Sodium-Ion Batteries. *Chem. Rev.* **2014,** *114* (23), 11636-82.

17. Hwang, J. Y.; Myung, S. T.; Sun, Y. K., Sodium-Ion Batteries: Present and Future. *Chem. Soc. Rev.* **2017,** *46* (12), 3529-3614.

18. Perveen, T.; Siddiq, M.; Shahzad, N.; Ihsan, R.; Ahmad, A.; Shahzad, M. I., Prospects in Anode Materials for Sodium Ion Batteries - A Review. *Renewable and Sustainable Energy Rev.* **2020,** *119*.

19. Balogun, M.-S.; Luo, Y.; Qiu, W.; Liu, P.; Tong, Y., A Review of Carbon Materials and Their Composites with Aloy Metals for Sodium Ion Battery Anodes. *Carbon* **2016,** *98*, 162-178.

20. Stevens, D. A.; Dahn, J. R., High Capacity Anode Materials for Rechargeable Sodium-Ion Batteries. *J. Electrochem. Soc.* **2000,** *147* (4).

21. Irisarri, E.; Ponrouch, A.; Palacin, M. R., Review-Hard Carbon Negative Electrode Materials for Sodium-Ion Batteries. *J. Electrochem. Soc.* **2015,** *162* (14), A2476-A2482.

22. Su, D.; Dou, S.; Wang, G., Anatase TiO_2: Better Anode Material Than Amorphous and Rutile Phases of TiO_2 for Na-Ion Batteries. *Chem. Mater.* **2015,** *27* (17), 6022-6029.

23. Lunell, S.; Stashans, A.; Ojamäe, L.; Lindström, H.; Hagfeldt, A., Li and Na Diffusion in TiO_2 from Quantum Chemical Theory versus Electrochemical Experiment. *J. Am. Chem. Soc.* **1997,** *119* (31), 7374-7380.

24. Wu, L.; Bresser, D.; Buchholz, D.; Giffin, G. A.; Castro, C. R.; Ochel, A.; Passerini, S., Unfolding the Mechanism of Sodium Insertion in Anatase TiO_2 Nanoparticles. *Adv. Energy Mater.* **2015,** *5* (2).

25. Jung, H.-G.; Myung, S.-T.; Yoon, C. S.; Son, S.-B.; Oh, K. H.; Amine, K.; Scrosati, B.; Sun, Y.-K., Microscale Spherical Carbon-Coated $Li_4Ti_5O_{12}$ as Ultra High Power Anode Material for Lithium Batteries. *Energy & Environ. Sci.* **2011,** *4* (4).

26. Sun, Y.; Zhao, L.; Pan, H.; Lu, X.; Gu, L.; Hu, Y. S.; Li, H.; Armand, M.; Ikuhara, Y.; Chen, L.; Huang, X., Direct Atomic-Scale Confirmation of Three-Phase Storage Mechanism in $Li_4Ti_5O_{12}$ Anodes for Room-Temperature Sodium-Ion Batteries. *Nat. Commun.* **2013,** *4*, 1870.

27. Rudola, A.; Saravanan, K.; Mason, C. W.; Balaya, P., $Na_2Ti_3O_7$: An Intercalation Based Anode for Sodium-Ion Battery Applications. *J. Mater. Chem. A* **2013,** *1* (7).

28. Pan, H.; Lu, X.; Yu, X.; Hu, Y.-S.; Li, H.; Yang, X.-Q.; Chen, L., Sodium Storage and Transport Properties in Layered $Na_2Ti_3O_7$ for Room-Temperature Sodium-Ion Batteries. *Adv. Energy Mater.* **2013,** *3* (9), 1186-1194.

29. Wu, D.; Li, X.; Xu, B.; Twu, N.; Liu, L.; Ceder, G., $NaTiO_2$: A Layered Anode Material for Sodium-Ion Batteries. *Energy & Environ. Sci.* **2015,** *8* (1), 195-202.

30. Aravindan, V.; Lee, Y.-S.; Yazami, R.; Madhavi, S., TiO_2 Polymorphs in 'Rocking-Chair' Li-Ion Batteries. *Mater. Today* **2015,** *18* (6), 345-351.

31. Guo, S.; Yi, J.; Sun, Y.; Zhou, H., Recent Advances in Titanium-Based Electrode Materials

for Stationary Sodium-Ion Batteries. *Energy & Environ. Sci.* **2016,** *9* (10), 2978-3006.

32. Chevrier, V. L.; Ceder, G., Challenges for Na-Ion Negative Electrodes. *J. Electrochem. Soc.* **2011,** *158* (9).

33. Lao, M.; Zhang, Y.; Luo, W.; Yan, Q.; Sun, W.; Dou, S. X., Alloy-Based Anode Materials toward Advanced Sodium-Ion Batteries. *Adv. Mater.* **2017,** *29* (48).

34. Mortazavi, M.; Ye, Q.; Birbilis, N.; Medhekar, N. V., High Capacity Group-15 Alloy Anodes for Na-Ion Batteries: Electrochemical and Mechanical Insights. *J. Power Sources* **2015,** *285*, 29-36.

35. Zou, F.; Chen, Y. M.; Liu, K.; Yu, Z.; Liang, W.; Bhaway, S. M.; Gao, M.; Zhu, Y., Metal Organic Frameworks Derived Hierarchical Hollow NiO/Ni/Graphene Composites for Lithium and Sodium Storage. *ACS Nano* **2016,** *10* (1), 377-86.

36. Peng, S.; Han, X.; Li, L.; Zhu, Z.; Cheng, F.; Srinivansan, M.; Adams, S.; Ramakrishna, S., Unique Cobalt Sulfide/Reduced Graphene Oxide Composite as an Anode for Sodium-Ion Batteries with Superior Rate Capability and Long Cycling Stability. *Small* **2016,** *12* (10), 1359-68.

37. Fan, M.; Chen, Y.; Xie, Y.; Yang, T.; Shen, X.; Xu, N.; Yu, H.; Yan, C., Half-Cell and Full-Cell Applications of Highly Stable and Binder-Free Sodium Ion Batteries Based on Cu_3P Nanowire Anodes. *Adv. Funct. Mater.* **2016,** *26* (28), 5019-5027.

38. Douglas, A.; Carter, R.; Oakes, L.; Share, K.; Cohn, A. P.; Pint, C. L., Ultrafine Iron Pyrite (FeS_2) Nanocrystals Improve Sodium-Sulfur and Lithium-Sulfur Conversion Reactions for Efficient Batteries. *ACS Nano* **2015,** *9* (11), 11156-65.

39. Klein, F.; Jache, B.; Bhide, A.; Adelhelm, P., Conversion Reactions for Sodium-Ion Batteries. *Phys. Chem. Chem. Phys.* **2013,** *15* (38), 15876-87.

40. Makhlooghiazad, F; Gonzalo, C; Johansson. P; Forsyth, M. Electrolytes for Sodium Batteries. DOI: 10.1002/9781119818069.ch5

41. Xu, K., Nonaqueous Liquid Electrolytes for Lithium-Based Rechargeable Batteries. *Chem.*

Rev. **2004,** *104* (10), 4303-417.

42. Aurbach, D.; Talyosef, Y.; Markovsky, B.; Markevich, E.; Zinigrad, E.; Asraf, L.; Gnanaraj, J. S.; Kim, H.-J., Design of Electrolyte Solutions for Li and Li-Ion Batteries: A Review. *Electrochim. Acta* **2004,** *50* (2-3), 247-254.

43. Ponrouch, A.; Monti, D.; Boschin, A.; Steen, B.; Johansson, P.; Palacín, M. R., Non-Aqueous Electrolytes for Sodium-Ion Batteries. *J. Mater. Chem. A* **2015,** *3* (1), 22-42.

44. Bommier, C.; Ji, X., Electrolytes, SEI Formation, and Binders: A Review of Nonelectrode Factors for Sodium-Ion Battery Anodes. *Small* **2018,** *14* (16), e1703576.

45. Eshetu, G. G.; Grugeon, S.; Kim, H.; Jeong, S.; Wu, L.; Gachot, G.; Laruelle, S.; Armand, M.; Passerini, S., Comprehensive Insights into the Reactivity of Electrolytes Based on Sodium Ions. *ChemSusChem* **2016,** *9* (5), 462-71.

46. Xu, K., Electrolytes and Interphases in Li-Ion Batteries and Beyond. *Chem. Rev.* **2014,** *114* (23), 11503-618.

47. Komaba, S.; Murata, W.; Ishikawa, T.; Yabuuchi, N.; Ozeki, T.; Nakayama, T.; Ogata, A.; Gotoh, K.; Fujiwara, K., Electrochemical Na Insertion and Solid Electrolyte Interphase for Hard-Carbon Electrodes and Application to Na-Ion Batteries. *Adv. Funct. Mater.* **2011,** *21* (20), 3859-3867.

48. Braconnier, J.-J.; Delmas, C.; Fouassier, C.; Hagenmuller, P., Comportement Electrochimique Des Phases Na_xCoO_2. *Mater. Research Bulletin* **1980,** *15* (12), 1797-1804.

49. Mendiboure, A.; Delmas, C.; Hagenmuller, P., Electrochemical Intercalation and Deintercalation of Na_xMnO_2 Bronzes. *J. Solid State Chem.* **1985,** *57* (3), 323-331.

50. Nguyen, N.-A.; Kim, K.; Choi, K. H.; Jeon, H.; Lee, K.; Ryou, M.-H.; Lee, Y. M., Effect of Calcination Temperature on a P-type $Na_{0.6}Mn_{0.65}Ni_{0.25}Co_{0.10}O_2$ Cathode Material for Sodium-Ion Batteries. *J. Electrochem. Soc.* **2016,** *164* (1), A6308-A6314.

51. Kumakura, S.; Tahara, Y.; Kubota, K.; Chihara, K.; Komaba, S., Sodium and Manganese Stoichiometry of P2-Type $Na_{2/3}MnO_2$. *Angew. Chem. Int. Ed.* **2016,** *55* (41), 12760-3.

52. Lu, Z.; Dahn, J. R., In Situ X-Ray Diffraction Study of P2-$Na_{2/3}Ni_{1/3}Mn_{2/3}O_2$. *J. Electrochem. Soc.* **2001,** *148* (11).

53. Yamada, A., Iron-based Materials Strategies. *MRS Bulletin* **2014,** *39* (5), 423-428.

54. Famery, R.; Bassoul, P.; Queyroux, F., Structure and Morphology Study of the Metastable Q2 Form in $LiFeO_2$ Ferrite by X-Ray Diffraction and Transmission Electron Microscopy. *J. Solid State Chem.* **1985,** *57* (2), 178-190.

55. Kikkawa, S.; Ohkura, H.; Koizumi, M., Ion Exchange of Layered α-$NaFeO_2$. *Mater. Chem. and Phys.* **1987,** *18* (4), 375-380.

56. Hirayama, M.; Tomita, H.; Kubota, K.; Kanno, R., Structure and Electrode Reactions of Layered Rocksalt $LiFeO_2$ Nanoparticles for Lithium Battery Cathode. *J. Power Sources* **2011,** *196* (16), 6809-6814.

57. Takeda, Y.; Nakahara, K.; Nishijima, M.; Imanishi, N.; Yamamoto, O.; Takano, M.; Kanno, R., Sodium Deintercalation from Sodium Iron Oxide. *Mater. Research Bulletin* **1994,** *29* (6), 659-666.

58. McLaren, V. L.; West, A. R.; Tabuchi, M.; Nakashima, A.; Takahara, H.; Kobayashi, H.; Sakaebe, H.; Kageyama, H.; Hirano, A.; Takeda, Y., Study of the Capacity Fading Mechanism for Fe-Substituted $LiCoO_2$ Positive Electrode. *J. Electrochem. Society* **2004,** *151* (5).

59. Lee, E.; Brown, D. E.; Alp, E. E.; Ren, Y.; Lu, J.; Woo, J.-J.; Johnson, C. S., New Insights into the Performance Degradation of Fe-Based Layered Oxides in Sodium-Ion Batteries: Instability of Fe^{3+}/Fe^{4+} Redox in α-$NaFeO_2$. *Chem. Mater.* **2015,** *27* (19), 6755-6764.

60. Takeda, Y.; Akagi, J.; Edagawa, A.; Inagaki, M.; Naka, S., A Preparation and Polymorphic Relations of Sodium Iron Oxide ($NaFeO_2$). *Mater. Research Bulletin* **1980,** *15* (8), 1167-1172.

61. Yabuuchi, N.; Yoshida, H.; Komaba, S., Crystal Structures and Electrode Performance of Alpha-$NaFeO_2$ for Rechargeable Sodium Batteries. *Electrochem.* **2012,** *80* (10), 716-719.

62. Velikokhatnyi, O. I.; Chang, C. C.; Kumta, P. N., Phase Stability and Electronic Structure of $NaMnO_2$. *J. Electrochem. Soc.* **2003,** *150* (9).

63. Parant, J.-P.; Olazcuaga, R.; Devalette, M.; Fouassier, C.; Hagenmuller, P., Sur Quelques Nouvelles Phases de Formule Na_xMnO_2 ($x \leqslant 1$). *J. Solid State Chem.* **1971,** *3* (1), 1-11.

64. Hoppe, R.; Brachtel, G.; Jansen, M., Zur Kenntnis der Oxomanganate(III):, Über $LiMnO_2$ und β-$NaMnO_2$. *J. Inorg. General Chem.* **1975,** *417* (1), 1-10.

65. Clément, R. J.; Middlemiss, D. S.; Seymour, I. D.; Ilott, A. J.; Grey, C. P., Insights into the Nature and Evolution upon Electrochemical Cycling of Planar Defects in the β-$NaMnO_2$ Na-Ion Battery Cathode: An NMR and First-Principles Density Functional Theory Approach. *Chem. Mater.* **2016,** *28* (22), 8228-8239.

66. Ma, X.; Chen, H.; Ceder, G., Electrochemical Properties of Monoclinic $NaMnO_2$. *J. Electrochem. Soc.* **2011,** *158* (12).

67. Bianchini, M.; Wang, J.; Clement, R. J.; Ouyang, B.; Xiao, P.; Kitchaev, D.; Shi, T.; Zhang, Y.; Wang, Y.; Kim, H.; Zhang, M.; Bai, J.; Wang, F.; Sun, W.; Ceder, G., The Interplay between Thermodynamics and Kinetics in the Solid-State Synthesis of Layered Oxides. *Nat. Mater.* **2020,** *19* (10), 1088-1095.

68. Billaud, J.; Clement, R. J.; Armstrong, A. R.; Canales-Vazquez, J.; Rozier, P.; Grey, C. P.; Bruce, P. G., beta-$NaMnO_2$: A High-Performance Cathode for Sodium-Ion Batteries. *J. Am. Chem. Soc.* **2014,** *136* (49), 17243-8.

69. Bordet-Le Guenne, L.; Deniard, P.; Biensan, P.; Siret, C.; Brec, R., Structural Study of Two Layered Phases in the $Na_xMn_yO_2$ System. Electrochemical Behavior of their Lithium Substituted Derivatives. *J. Mater. Chem.* **2000,** *10* (9), 2201-2206.

70. Paulsen, J. M.; Dahn, J. R., Studies of the Layered Manganese Bronzes, $Na_{2/3}[Mn_{1-x}M_x]O_2$ with M=Co, Ni, Li, and $Li_{2/3}[Mn_{1-x}M_x]O_2$ Prepared by Ion-Exchange. *Solid State Ionics* **1999,** *126* (1-2), 3-24.

71. Stoyanova, R.; Carlier, D.; Sendova-Vassileva, M.; Yoncheva, M.; Zhecheva, E.; Nihtianova, D.; Delmas, C., Stabilization of Over-Stoichiometric Mn^{4+} in Layered $Na_{2/3}MnO_2$. *J. Solid State Chem.* **2010,** *183* (6), 1372-1379.

72. de la Llave, E.; Talaie, E.; Levi, E.; Nayak, P. K.; Dixit, M.; Rao, P. T.; Hartmann, P.; Chesneau, F.; Major, D. T.; Greenstein, M.; Aurbach, D.; Nazar, L. F., Improving Energy Density and Structural Stability of Manganese Oxide Cathodes for Na-Ion Batteries by Structural Lithium Substitution. *Chem. Mater.* **2016,** *28* (24), 9064-9076.

73. Yabuuchi, N.; Kajiyama, M.; Iwatate, J.; Nishikawa, H.; Hitomi, S.; Okuyama, R.; Usui, R.; Yamada, Y.; Komaba, S., P2-type $Na_x[Fe_{1/2}Mn_{1/2}]O_2$ Made from Earth-Abundant Elements for Rechargeable Na Batteries. *Nat. Mater.* **2012,** *11* (6), 512-7.

74. Katcho, N. A.; Carrasco, J.; Saurel, D.; Gonzalo, E.; Han, M.; Aguesse, F.; Rojo, T., Origins of Bistability and Na Ion Mobility Difference in P2- and O3-$Na_{2/3}Fe_{2/3}Mn_{1/3}O_2$ Cathode Polymorphs. *Adv. Energy Mater.* **2017,** *7* (1).

75. Pang, W. K.; Kalluri, S.; Peterson, V. K.; Sharma, N.; Kimpton, J.; Johannessen, B.; Liu, H. K.; Dou, S. X.; Guo, Z., Interplay between Electrochemistry and Phase Evolution of the P2-type $Na_x(Fe_{1/2}Mn_{1/2})O_2$ Cathode for Use in Sodium-Ion Batteries. *Chem. Mater.* **2015,** *27* (8), 3150-3158.

76. Dose, W. M.; Sharma, N.; Pramudita, J. C.; Kimpton, J. A.; Gonzalo, E.; Han, M. H.; Rojo, T., Crystallographic Evolution of P2 $Na_{2/3}Fe_{0.4}Mn_{0.6}O_2$ Electrodes during Electrochemical Cycling. *Chem. Mater.* **2016,** *28* (17), 6342-6354.

77. Yang, T.; Huang, Y.; Zhang, J.; Zhu, H.; Ren, J.; Li, T.; Gallington, L. C.; Lan, S.; Yang, L.; Liu, Q., Insights into Ti Doping for Stabilizing the $Na_{2/3}Fe_{1/3}Mn_{2/3}O_2$ Cathode in Sodium Ion Battery. *J. Energy Chem.* **2022,** *73*, 542-548.

78. Shin, H.-J.; Jung, Y. H.; Kim, M.; Kim, N.; Wang, J. E., X-Ray Absorption Spectromicroscopy of $Na_{0.67}Fe_{0.25}Mn_{0.75}O_2$ and $Na_{0.67}Li_{0.2}Fe_{0.2}Mn_{0.6}O_2$ Primary Particles for Na-Ion Batteries. *J. Phys. Chem. Solids* **2023,** *177*.

79. Zhou, D.; Huang, W.; Lv, X.; Zhao, F., A Novel P2/O3 Biphase $Na_{0.67}Fe_{0.425}Mn_{0.425}Mg_{0.15}O_2$ as Cathode for High-Performance Sodium-Ion Batteries. *J.Power Sources* **2019,** *421*, 147-155.

80. Han, M. H.; Gonzalo, E.; Sharma, N.; López del Amo, J. M.; Armand, M.; Avdeev, M.; Saiz Garitaonandia, J. J.; Rojo, T., High-Performance P2-Phase $Na_{2/3}Mn_{0.8}Fe_{0.1}Ti_{0.1}O_2$ Cathode Material for Ambient-Temperature Sodium-Ion Batteries. *Chem. Mater.* **2015,** *28* (1), 106-116.

81. Shacklette, L. W.; Jow, T. R.; Townsend, L., Rechargeable Electrodes from Sodium Cobalt Bronzes. *J. Electrochem. Soc.* **2019,** *135* (11), 2669-2674.

82. Han, S. C.; Lim, H.; Jeong, J.; Ahn, D.; Park, W. B.; Sohn, K.-S.; Pyo, M., Ca-Doped Na_x CoO_2 for Improved Cyclability in Sodium Ion Batteries. *J. Power Sources* **2015,** *277*, 9-16.

83. Wang, P.-F.; You, Y.; Yin, Y.-X.; Guo, Y.-G., Layered Oxide Cathodes for Sodium-Ion Batteries: Phase Transition, Air Stability, and Performance. *Adv. Energy Mater.* **2018,** *8* (8).

84. Vassilaras, P.; Ma, X.; Li, X.; Ceder, G., Electrochemical Properties of Monoclinic $NaNiO_2$. *J. Electrochem. Soc.* **2012,** *160* (2), A207-A211.

85. Nanba, Y.; Iwao, T.; Boisse, B. M. d.; Zhao, W.; Hosono, E.; Asakura, D.; Niwa, H.; Kiuchi, H.; Miyawaki, J.; Harada, Y.; Okubo, M.; Yamada, A., Redox Potential Paradox in $NaxMO_2$ for Sodium-Ion Battery Cathodes. *Chem.Mater.* **2016,** *28* (4), 1058-1065.

86. Yuan, D. D.; Wang, Y. X.; Cao, Y. L.; Ai, X. P.; Yang, H. X., Improved Electrochemical Performance of Fe-Substituted $NaNi_{0.5}Mn_{0.5}O_2$ Cathode Materials for Sodium-Ion Batteries. *ACS Appl. Mater. Interfaces* **2015,** *7* (16), 8585-91.

87. Hwang, J. Y.; Oh, S. M.; Myung, S. T.; Chung, K. Y.; Belharouak, I.; Sun, Y. K., Radially Aligned Hierarchical Columnar Structure as a Cathode Material for High Energy Density Sodium-Ion Batteries. *Nat. Commun.* **2015,** *6*, 6865.

88. Qian, J.; Wu, C.; Cao, Y.; Ma, Z.; Huang, Y.; Ai, X.; Yang, H., Prussian Blue Cathode Materials for Sodium-Ion Batteries and Other Ion Batteries. *Adv. Energy Mater.* **2018,** *8* (17).

89. Neff, V. D., Electrochemical Oxidation and Reduction of Thin Films of Prussian Blue. *J. Electrochem. Soc.* **2019,** *125* (6), 886-887.

90. Zhang, H.; Tan, X.; Li, H.; Passerini, S.; Huang, W., Assessment and Progress of Polyanionic Cathodes in Aqueous Sodium Batteries. *Energy & Environ. Sci.* **2021,** *14* (11),

5788-5800.

91. Moreau, P.; Guyomard, D.; Gaubicher, J.; Boucher, F., Structure and Stability of Sodium Intercalated Phases in Olivine $FePO_4$. *Chem. Mater.* **2010,** *22* (14), 4126-4128.

92. Kim, H.; Shakoor, R. A.; Park, C.; Lim, S. Y.; Kim, J.-S.; Jo, Y. N.; Cho, W.; Miyasaka, K.; Kahraman, R.; Jung, Y.; Choi, J. W., $Na_2FeP_2O_7$ as a Promising Iron-Based Pyrophosphate Cathode for Sodium Rechargeable Batteries: A Combined Experimental and Theoretical Study. *Adv. Funct. Mater.* **2013,** *23* (9), 1147-1155.

93. Qiu, S.; Wu, X.; Wang, M.; Lucero, M.; Wang, Y.; Wang, J.; Yang, Z.; Xu, W.; Wang, Q.; Gu, M.; Wen, J.; Huang, Y.; Xu, Z. J.; Feng, Z., NASICON-Type $Na_3Fe_2(PO_4)_3$ as a Low-Cost and High-Rate Anode Material for Aqueous Sodium-Ion Batteries. *Nano Energy* **2019,** *64*.

94. Kim, H.; Park, I.; Lee, S.; Kim, H.; Park, K.-Y.; Park, Y.-U.; Kim, H.; Kim, J.; Lim, H.-D.; Yoon, W.-S.; Kang, K., Understanding the Electrochemical Mechanism of the New Iron-Based Mixed-Phosphate $Na_4Fe_3(PO_4)_2(P_2O_7)$ in a Na Rechargeable Battery. *Chem. Mater.* **2013,** *25* (18), 3614-3622.

95. Jin, T.; Li, H.; Zhu, K.; Wang, P. F.; Liu, P.; Jiao, L., Polyanion-Type Cathode Materials for Sodium-Ion Batteries. *Chem. Soc. Rev.* **2020,** *49* (8), 2342-2377.

96. Kang, H.-C.; Jun, D.-K.; Jin, B.; Jin, E. M.; Park, K.-H.; Gu, H.-B.; Kim, K.-W., Optimized Solid-State Synthesis of $LiFePO_4$ Cathode Materials using Ball-Milling. *J. Power Sources* **2008,** *179* (1), 340-346.

97. Rodríguez-Carvajal, J., Recent Advances in Magnetic Structure Determination by Neutron Powder Diffraction. *Phys. B: Condensed Matter* **1993,** *192* (1-2), 55-69.

98. Dippel, A. C.; Liermann, H. P.; Delitz, J. T.; Walter, P.; Schulte-Schrepping, H.; Seeck, O. H.; Franz, H., Beamline P02.1 at PETRA III for High-Resolution and High-Energy Powder Diffraction. *J. Synchr. Radiat* **2015,** *22* (3), 675-87.

99. Filik, J.; Ashton, A. W.; Chang, P. C. Y.; Chater, P. A.; Day, S. J.; Drakopoulos, M.; Gerring, M. W.; Hart, M. L.; Magdysyuk, O. V.; Michalik, S.; Smith, A.; Tang, C. C.; Terrill,

N. J.; Wharmby, M. T.; Wilhelm, H., Processing Two-Dimensional X-Ray Diffraction and Small-Angle Scattering Data in DAWN 2. *J. Appl. Crystallogr.* **2017,** *50* (Pt 3), 959-966.

100. Momma, K.; Izumi, F., VESTA 3 for Three-Dimensional Visualization of Crystal, Volumetric and Morphology Data. *J. Appl. Crystallogr.* **2011,** *44* (6), 1272-1276.

101. Ravel, B.; Newville, M., ATHENA and ARTEMIS Interactive Graphical Data Analysisusing IFEFFIT. *Phys. Scr.* **2005**.

102. Verma, A.; Smith, K.; Santhanagopalan, S.; Abraham, D.; Yao, K. P.; Mukherjee, P. P., Galvanostatic Intermittent Titration and Performance Based Analysis of $LiNi_{0.5}Co_{0.2}Mn_{0.3}O_2$ Cathode. *J. Electrochem. Soc.* **2017,** *164* (13), A3380-A3392.

103. Yoda, Y.; Kubota, K.; Kuroki, K.; Suzuki, S.; Yamanaka, K.; Yaji, T.; Amagasa, S.; Yamada, Y.; Ohta, T.; Komaba, S., Elucidating Influence of Mg- and Cu-Doping on Electrochemical Properties of O3-Nax[Fe,Mn]O_2 for Na-Ion Batteries. *Small* **2020,** *16* (50), e2006483.

104. Mortemard de Boisse, B.; Carlier, D.; Guignard, M.; Delmas, C., Structural and Electrochemical Characterizations of P2 and New O3-$Na_xMn_{1-y}Fe_yO_2$ Phases Prepared by Auto-Combustion Synthesis for Na-Ion Batteries. *J. Electrochem. Soc.* **2013,** *160* (4), A569-A574.

105. Yang, L.; Amo, J. M. L.; Shadike, Z.; Bak, S. M.; Bonilla, F.; Galceran, M.; Nayak, P. K.; Buchheim, J. R.; Yang, X. Q.; Rojo, T.; Adelhelm, P., A Co- and Ni-Free P2/O3 Biphasic Lithium Stabilized Layered Oxide for Sodium-Ion Batteries and its Cycling Behavior. *Adv. Funct. Mater.* **2020,** *30* (42).

106. Zhou, D.; Zeng, C.; Ling, D.; Wang, T.; Gao, Z.; Li, J.; Tian, L.; Wang, Y.; Huang, W., Sustainable Alternative Cathodes of Sodium-Ion Batteries using Hybrid P2/O3 Phase $Na_{0.67}Fe_{0.5}Mn_{0.5-x}Mg_xO_2$. *J. Alloys Compd.* **2023,** *931*.

107. Chen, C.; Huang, W.; Li, Y.; Zhang, M.; Nie, K.; Wang, J.; Zhao, W.; Qi, R.; Zuo, C.; Li, Z.; Yi, H.; Pan, F., P2/O3 Biphasic Fe/Mn-Based Layered Oxide Cathode with Ultrahigh

Capacity and Great Cyclability for Sodium Ion Bbatteries. *Nano Energy* **2021,** *90*.

108. Park, Y. J.; Choi, J. U.; Jo, J. H.; Jo, C. H.; Kim, J.; Myung, S. T., A New Strategy to Build a High-Performance P'2-Type Cathode Material through Titanium Doping for Sodium-Ion Batteries. *Adv. Funct. Mater.* **2019,** *29* (28).

109. Mortemard de Boisse, B.; Carlier, D.; Guignard, M.; Bourgeois, L.; Delmas, C., P2-$Na_xMn_{1/2}Fe_{1/2}O_2$ Phase Used as Positive Electrode in Na Batteries: Structural Changes Induced by the Electrochemical (De)intercalation Process. *Inorg. Chem.* **2014,** *53* (20), 11197-205.

110. Risthaus, T.; Chen, L.; Wang, J.; Li, J.; Zhou, D.; Zhang, L.; Ning, D.; Cao, X.; Zhang, X.; Schumacher, G.; Winter, M.; Paillard, E.; Li, J., P3 $Na_{0.9}Ni_{0.5}Mn_{0.5}O_2$ Cathode Material for Sodium Ion Batteries. *Chem. Mater.* **2019,** *31* (15), 5376-5383.

111. Talaie, E.; Duffort, V.; Smith, H. L.; Fultz, B.; Nazar, L. F., Structure of the High Voltage Phase of Layered P2-$Na_{2/3-z}[Mn_{1/2}Fe_{1/2}]O_2$ and the Positive Effect of Ni Substitution on its Stability. *Energy & Environ. Sci.* **2015,** *8* (8), 2512-2523.

112. Tarascon, J.-M., Na-Ion versus Li-Ion Batteries: Complementarity Rather than Competitiveness. *Joule* **2020,** *4* (8), 1613-1620.

113. Dunn, B.; Kamath, H.; Tarascon, J. M., Electrical Energy Storage for the Grid: A Battery of Choices. *Science* **2011,** *334* (6058), 928-35.

114. Liu, Q.; Hu, Z.; Chen, M.; Zou, C.; Jin, H.; Wang, S.; Chou, S. L.; Dou, S. X., Recent Progress of Layered Transition Metal Oxide Cathodes for Sodium-Ion Batteries. *Small* **2019,** *15* (32), e1805381.

115. Delmas, C.; Carlier, D.; Guignard, M., The Layered Oxides in Lithium and Sodium-Ion Batteries: A Solid-State Chemistry Approach. *Adv. Energy Mater.* **2020,** *11* (2).

116. Kubota, K.; Kumakura, S.; Yoda, Y.; Kuroki, K.; Komaba, S., Electrochemistry and Solid-State Chemistry of $NaMeO_2$ (Me = 3d Transition Metals). *Adv. Energy Mater.* **2018,** *8* (17).

117. Kim, D.; Kang, S.-H.; Slater, M.; Rood, S.; Vaughey, J. T.; Karan, N.; Balasubramanian,

M.; Johnson, C. S., Enabling Sodium Batteries Using Lithium-Substituted Sodium Layered Transition Metal Oxide Cathodes. *Adv. Energy Mater.* **2011,** *1* (3), 333-336.

118. Mo, Y.; Ong, S. P.; Ceder, G., Insights into Diffusion Mechanisms in P2 Layered Oxide Materials by First-Principles Calculations. *Chem. Mater.* **2014,** *26* (18), 5208-5214.

119. Lee, D. H.; Xu, J.; Meng, Y. S., An Advanced Cathode for Na-Ion Batteries with High Rate and Excellent Structural Stability. *Phys. Chem. Chem. Phys.* **2013,** *15* (9), 3304-12.

120. Darbar, D.; Reddy, M. V.; Bhattacharya, I., Understanding the Effect of Zn Doping on Stability of Cobalt-Free P2-$Na_{0.60}Fe_{0.5}Mn_{0.5}O_2$ Cathode for Sodium Ion Batteries. *Electrochem.* **2021,** *2* (2), 323-334.

121. Somerville, J. W.; Sobkowiak, A.; Tapia-Ruiz, N.; Billaud, J.; Lozano, J. G.; House, R. A.; Gallington, L. C.; Ericsson, T.; Häggström, L.; Roberts, M. R.; Maitra, U.; Bruce, P. G., Nature of the "Z"-Phase in Layered Na-Ion Battery Cathodes. *Energy & Environ. Sci.* **2019,** *12* (7), 2223-2232.

122. Talaie, E.; Kim, S. Y.; Chen, N.; Nazar, L. F., Structural Evolution and Redox Processes Involved in the Electrochemical Cycling of P2-$Na_{0.67}[Mn_{0.66}Fe_{0.20}Cu_{0.14}]O_2$. *Chem. Mater.* **2017,** *29* (16), 6684-6697.

123. Wang, H.; Gao, R.; Li, Z.; Sun, L.; Hu, Z.; Liu, X., Different Effects of Al Substitution for Mn or Fe on the Structure and Electrochemical Properties of $Na_{0.67}Mn_{0.5}Fe_{0.5}O_2$ as a Sodium Ion Battery Cathode Material. *Inorg. Chem.* **2018,** *57* (9), 5249-5257.

124. Clément, R. J.; Billaud, J.; Robert Armstrong, A.; Singh, G.; Rojo, T.; Bruce, P. G.; Grey, C. P., Structurally Stable Mg-Doped P2-$Na_{2/3}Mn_{1-y}Mg_yO_2$ Sodium-Ion Battery Cathodes with High Rate Performance: Insights from Electrochemical, NMR and Diffraction Studies. *Energy & Environ. Sci.* **2016,** *9* (10), 3240-3251.

125. Ma, C.; Alvarado, J.; Xu, J.; Clement, R. J.; Kodur, M.; Tong, W.; Grey, C. P.; Meng, Y. S., Exploring Oxygen Activity in the High Energy P2-Type $Na_{0.78}Ni_{0.23}Mn_{0.69}O_2$ Cathode Material for Na-Ion Batteries. *J. Am. Chem. Soc.* **2017,** *139* (13), 4835-4845.

126. Maitra, U.; House, R. A.; Somerville, J. W.; Tapia-Ruiz, N.; Lozano, J. G.; Guerrini, N.; Hao, R.; Luo, K.; Jin, L.; Perez-Osorio, M. A.; Massel, F.; Pickup, D. M.; Ramos, S.; Lu, X.; McNally, D. E.; Chadwick, A. V.; Giustino, F.; Schmitt, T.; Duda, L. C.; Roberts, M. R.; Bruce, P. G., Oxygen Redox Chemistry without Excess Alkali-Metal Ions in $Na_{2/3}[Mg_{0.28}Mn_{0.72}]O_2$. *Nat. Chem.* **2018,** *10* (3), 288-295.

127. Shannon, R. D., Revised Effective Ionic Radii and Systematic Studies of Interatomic Distances in Halides and Chalcogenides. *Acta Crystallogr. Sec. A* **1976,** *32* (5), 751-767.

128. Mortemard de Boisse, B.; Carlier, D.; Guignard, M.; Guerin, E.; Duttine, M.; Wattiaux, A.; Delmas, C., Influence of Mn/Fe Ratio on Electrochemical and Structural Properties of P2-$Na_xMn_{1-y}Fe_yO_2$ Phases as Positive Electrode Material for Na-Ion Batteries. *Chem. Mater.* **2018,** *30* (21), 7672-7681.

129. Gonzalo, E.; Han, M. H.; López del Amo, J. M.; Acebedo, B.; Casas-Cabanas, M.; Rojo, T., Synthesis and Characterization of Pure P2- and O3-$Na_{2/3}Fe_{2/3}Mn_{1/3}O_2$ as Cathode Materials for Na Ion Batteries. *J. Mater. Chem. A* **2014,** *2* (43), 18523-18530.

130. Mortemard de Boisse, B.; Cheng, J. H.; Carlier, D.; Guignard, M.; Pan, C. J.; Bordère, S.; Filimonov, D.; Drathen, C.; Suard, E.; Hwang, B. J.; Wattiaux, A.; Delmas, C., O3-$Na_xMn_{1/3}Fe_{2/3}O_2$ as a Positive Electrode Material for Na-Ion Batteries: Structural Evolutions and Redox Mechanisms upon Na^+ (De)intercalation. *J. Mater. Chem. A* **2015,** *3* (20), 10976-10989.

131. Darbar, D.; Muralidharan, N.; Hermann, R. P.; Nanda, J.; Bhattacharya, I., Evaluation of Electrochemical Performance and Redox Activity of Fe in Ti Doped Layered P2-$Na_{0.67}Mn_{0.5}Fe_{0.5}O_2$ Cathode for Sodium Ion Batteries. *Electrochim. Acta* **2021,** *380*.

132. Cao, M.-H.; Li, R.-Y.; Lin, S.-Y.; Zheng, S.-D.; Ma, L.; Tan, S.; Hu, E.; Shadike, Z.; Yang, X.-Q.; Fu, Z.-W., Oxygen Redox Chemistry in P2-$Na_{0.6}Li_{0.11}Fe_{0.27}Mn_{0.62}O_2$ Cathode for High-Energy Na-ion Batteries. *J. Mater. Chem. A* **2021,** *9* (48), 27651-27659.

133. Jung, Y. H.; Christiansen, A. S.; Johnsen, R. E.; Norby, P.; Kim, D. K., In Situ X-Ray

Diffraction Studies on Structural Changes of a P2 Layered Material during Electrochemical Desodiation/Sodiation. *Adv. Funct. Mater.* **2015,** *25* (21), 3227-3237.

134. Li, Z.; Kong, W.; Yu, Y.; Zhang, J.; Wong, D.; Xu, Z.; Chen, Z.; Schulz, C.; Bartkowiak, M.; Liu, X., Tuning Bulk O_2 and Nonbonding Oxygen State for Reversible Anionic Redox Chemistry in P2-Layered Cathodes. *Angew. Chem. Int. Ed.* **2022,** *61* (16), e202115552.

135. Grey, C. P.; Dupre, N., NMR Studies of Cathode Materials for Lithium-Ion Rechargeable Batteries. *Chem. Rev.* **2004,** *104* (10), 4493-512.

136. Menil, F., Systematic Trends of the ^{57}Fe Mössbauer Isomer Shifts in (FeO_n) and (FeF_n) Polyhedra. Evidence of a New Correlation between the Isomer Shift and the Inductive Effect of the Competing Bond T-X (→ Fe) (Where X is O or F and T Any Element with a Formal Positive Charge). *J. Phys. Chem. Solids* **1985,** *46* (7), 763-789.

137. Dräger, C.; Sigel, F.; Witte, R.; Kruk, R.; Pfaffmann, L.; Mangold, S.; Mereacre, V.; Knapp, M.; Ehrenberg, H.; Indris, S., Observation of Electrochemically Active Fe^{3+}/Fe^{4+} in $LiCo_{0.8}Fe_{0.2}MnO_4$ by in situ Mössbauer Spectroscopy and X-Ray Absorption Spectroscopy. *Phys. Chem. Chem. Phys.* **2018,** *21* (1), 89-95.

138. Gilbert, B.; Frazer, B. H.; Belz, A.; Conrad, P. G.; Nealson, K. H.; Haskel, D.; Lang, J. C.; Srajer, G.; De Stasio, G., Multiple Scattering Calculations of Bonding and X-Ray Absorption Spectroscopy of Manganese Oxides. *J. Phys. Chem. A* **2003,** *107* (16), 2839-2847.

139. Kim, D. H.; Lee, H. J.; Kim, G.; Koo, Y. S.; Jung, J. H.; Shin, H. J.; Kim, J. Y.; Kang, J. S., Interface Electronic Structures of $BaTiO_3$@X Nanoparticles (X=γ-Fe_2O_3, Fe_3O_4, α-Fe_2O_3, and Fe) Investigated by XAS and XMCD. *Phys. Rev. B* **2009,** *79* (3).

140. Yoon, W. S.; Balasubramanian, M.; Chung, K. Y.; Yang, X. Q.; McBreen, J.; Grey, C. P.; Fischer, D. A., Investigation of the Charge Compensation Mechanism on the Electrochemically Li-Ion Deintercalated $Li_{1-x}Co_{1/3}Ni_{1/3}Mn_{1/3}O_2$ Electrode System by Combination of Soft and Hard X-Ray Absorption Spectroscopy. *J. Am. Chem. Soc.* **2005,** *127* (49), 17479-87.

141. Wang, Q.; Liao, Y.; Jin, X.; Cheng, C.; Chu, S.; Sheng, C.; Zhang, L.; Hu, B.; Guo, S.; Zhou, H., Dual Honeycomb-Superlattice Enables Double-High Activity and Reversibility of Anion Redox for Sodium-Ion Battery Layered Cathodes. *Angew. Chem. Int. Ed.* **2022,** *61* (33), e202206625.

142. Li, H.; Hua, Li, H.; Hua, W.; Liu-Théato, X.; Fu, Q.; Desmau, M.; Missyul, A.; Knapp, M.; Ehrenberg, H.; Indris, S., New Insights into Lithium Hopping and Ordering in $LiNiO_2$ Cathodes during Li (De)intercalation. *Chem. Mater.* **2021,** *33* (24), 9546-9559.

143. Zhao, C.; Wang, Q.; Yao, Z.; Wang, J.; Sanchez-Lengeling, B.; Ding, F.; Qi, X.; Lu, Y.; Bai, X.; Li, B.; Li, H.; Aspuru-Guzik, A.; Huang, X.; Delmas, C.; Wagemaker, M.; Chen, L.; Hu, Y. S., Rational Design of Layered Oxide Materials for Sodium-Ion Batteries. *Science* **2020,** *370* (6517), 708-711.

144. Xiao, Y.; Wang, H. R.; Hu, H. Y.; Zhu, Y. F.; Li, S.; Li, J. Y.; Wu, X. W.; Chou, S. L., Formulating High-Rate and Long-Cycle Heterostructured Layered Oxide Cathodes by Local Chemistry and Orbital Hybridization Modulation for Sodium-Ion Batteries. *Adv. Mater.* **2022,** *34* (33), e2202695.

145. Ren, H.; Li, Y.; Ni, Q.; Bai, Y.; Zhao, H.; Wu, C., Unraveling Anionic Redox for Sodium Layered Oxide Cathodes: Breakthroughs and Perspectives. *Adv. Mater.* **2022,** *34* (8), e2106171.

146. Kalapsazova, M.; Stoyanova, R.; Zhecheva, E.; Tyuliev, G.; Nihtianova, D., Sodium Deficient Nickel-Manganese Oxides as Intercalation Electrodes in Lithium Ion Batteries. *J. Mater. Chem. A* **2014,** *2* (45), 19383-19395.

147. Jo, J. H.; Kim, H. J.; Choi, J. U.; Voronina, N.; Lee, K.-S.; Ihm, K.; Lee, H.-K.; Lim, H.-D.; Kim, H.; Jung, H.-G.; Chung, K. Y.; Yashiro, H.; Myung, S.-T., Facilitating Sustainable Oxygen-Redox Chemistry for P3-type Cathode Materials for Sodium-Ion Batteries. *Energy Storage Mater.* **2022,** *46*, 329-343.

148. Kim, E. J.; Ma, L. A.; Pickup, D. M.; Chadwick, A. V.; Younesi, R.; Maughan, P.; Irvine, J. T. S.; Armstrong, A. R., Vacancy-Enhanced Oxygen Redox Reversibility in P3-Type

Magnesium-Doped Sodium Manganese Oxide $Na_{0.67}Mg_{0.2}Mn_{0.8}O_2$. *ACS Appl. Energy Mater.* **2020,** *3* (11), 10423-10434.

149. Song, B.; Hu, E.; Liu, J.; Zhang, Y.; Yang, X.-Q.; Nanda, J.; Huq, A.; Page, K., A Novel P3-Type $Na_{2/3}Mg_{1/3}Mn_{2/3}O_2$ as High Capacity Sodium-Ion Cathode using Reversible Oxygen Redox. *J. Mater. Chem. A* **2019,** *7* (4), 1491-1498.

150. Zhang, L.; Wang, J.; Li, J.; Schuck, G.; Winter, M.; Schumacher, G.; Li, J., Preferential Occupation of Na in P3-Type Layered Cathode Material for Sodium Ion Batteries. *Nano Energy* **2020,** *70*.

151. Komaba, S.; Yabuuchi, N.; Nakayama, T.; Ogata, A.; Ishikawa, T.; Nakai, I., Study on the Reversible Electrode Reaction of $Na_{1-x}Ni_{0.5}Mn_{0.5}O_2$ for a Rechargeable Sodium-Ion Battery. *Inorg. Chem.* **2012,** *51* (11), 6211-20.

152. Zhu, H.; Huang, Y.; Ren, J.; Zhang, B.; Ke, Y.; Jen, A. K.; Zhang, Q.; Wang, X. L.; Liu, Q., Bridging Structural Inhomogeneity to Functionality: Pair Distribution Function Methods for Functional Materials Development. *Adv. Sci.* **2021,** *8* (6), 2003534.

153. Huang, Y.; Yan, Z.; Luo, W.; Hu, Z.; Liu, G.; Zhang, L.; Yang, X.; Ou, M.; Liu, W.; Huang, L.; Lin, H.; Chen, C.-T.; Luo, J.; Li, S.; Han, J.; Chou, S.; Huang, Y., Vitalization of P2-$Na_{2/3}Ni_{1/3}Mn_{2/3}O_2$ at High-Voltage Cyclability via Combined Structural Modulation for Sodium-Ion Batteries. *Energy Storage Mater.* **2020,** *29*, 182-189.

154. Toby, B. H., EXPGUI, a Graphical User Interface for GSAS. *J. Appl. Crystallogr.* **2001,** *34* (2), 210-213.

155. Wu, X.; Chen, C.; Zhao, C.; Liu, H.; Hu, B.; Li, J.; Li, C.; Hu, B., Achieving Long-Enduring High-Voltage Oxygen Redox in P2-Structured Layered Oxide Cathodes by Eliminating Nonlattice Oxygen Redox. *Small* **2023**, e2300878.

156. Hu, B.; Qiu, Q.; Li, C.; Shen, M.; Hu, B.; Tong, W.; Wang, K.; Zhou, Q.; Zhang, Y.; He, Z.; Zhang, T.; Chen, C., Tailoring Anionic Redox Activity in a P2-Type Sodium Layered Oxide Cathode via Cu Substitution. *ACS Appl. Mater. Interfaces* **2022,** *14* (25), 28738-28747.

157. Liu, X.; Zuo, W.; Zheng, B.; Xiang, Y.; Zhou, K.; Xiao, Z.; Shan, P.; Shi, J.; Li, Q.; Zhong, G.; Fu, R.; Yang, Y., P2-$Na_{0.67}Al_xMn_{1-x}O_2$: Cost-Effective, Stable and High-Rate Sodium Electrodes by Suppressing Phase Transitions and Enhancing Sodium Cation Mobility. *Angew. Chem. Int. Ed.* **2019,** *58* (50), 18086-18095.

158. Niu, Y.; Hu, Z.; Zhang, B.; Xiao, D.; Mao, H.; Zhou, L.; Ding, F.; Liu, Y.; Yang, Y.; Xu, J.; Yin, W.; Zhang, N.; Li, Z.; Yu, X.; Hu, H.; Lu, Y.; Rong, X.; Li, J.; Hu, Y. S., Earth-Abundant Na-Mg-Fe-Mn-O Cathode with Reversible Hybrid Anionic and Cationic Redox. *Adv. Energy Mater.* **2023,** *13* (27).

Publication

Publication during PhD study:

1. **Peng, J**.; Sarapulova, A.; Fu, Q.; Li, H.; Liu, H.; Dolotkoa, O.; Kleiner, K.; Ying, Y; Wu, Y.; Baran, V.; Welter, E.; Nagel, P.; Schuppler, S.; Merze, M.; Knapp, M.; Ehrenberg, H.; Indris, S. Understanding the Electrochemical Reaction Mechanism of the Co/Ni Free Layered Cathode Material P2-$Na_{2/3}Mn_{7/12}Fe_{1/3}Ti_{1/12}O_2$ for Sodium-Ion Batteries, submitted after revision.

2. Wang, H.; Bo, Y.; Klingenhof, M.; **Peng, J**.; Wang, D.; Wu, B.; Pezoldt, J.; Cheng, P.; Knauer, A.; Hua, W.; Wang, H.; Aken, P.; Sofer, Z.; Strasser, P.; Guldi, D.; Schaaf, P. A Universal Design Strategy Based on $NiPS_3$ Nanosheets towards Efficient Photothermal Conversion and Solar Desalination, **2023**, 2310942.

3. Han, D.; Zhang, J.; Yang, M.; Xie, K.; **Peng, J**; Dolotkoa, O.; Huang, C.; Wu, Y.; Shao, L.; Hua, W.; Tang, W. Enhancing the Long-Term Cycling Stability of Ni-Rich Cathodes via Regulating the Length/Width Ratio of Primary Particle, submitted after revision.

4. Yang, X.; Wang, S.; Li, H.; **Peng, J**.; Zeng, W.; Tsai, H.; Hung, S.; Indris, S.; Li, F.; Hua, W. Boosting the Ultra-stable High-Na-Content P2-Type Layered Cathode Materials with Zero-Strain Cation Storage via a Lithium Dual-Site Substitution Approach, **2023**, *17*(18), 18616-18628

Previous publication during master study

1. Zhao, W.; **Peng, J.**; Wang, W.; Liu, S.; Zhao, Q.; Huang, W. Ultrathin Two-Dimensional Metal-Organic Framework Nanosheets for Functional Electronic Devices. **2018**, *377*, 44-63.

2. Zhao, W.; **Peng, J.**; Wang, W.; Jin, B.; Chen, T.; Liu, S.; Zhao, Q.; Huang, W. Interlayer Hydrogen-Bonded Metal Porphyrin Frameworks/MXene Hybrid Film with High Capacity for Flexible All-Solid-State Supercapacitors. **2019**, *15* (18), 1901351.

3. Zhao, W.; Wang, W.; **Peng, J.**; Chen, T.; Jin, B.; Liu, S.; Zhao, Q.; Huang, W. Wrinkled Two-Dimensional Ultrathin Cu (II)-Porphyrin Framework Nanosheets Hybridized with Polypyrrole for Flexible All-Solid-State Supercapacitors. **2019**, *48* (26), 9631-9638.

Declaration

Die vorliegende Arbeit wurde im Zeitraum vom Oktober 2020 bis Oktober 2023 am Institut für am Institut für Angewandte Materialien und der Anorganischen Chemie der Fakultät für Chemie und Biowissenschaften am Karlsruher Institut für Technologie (KIT) unter der Leitung von Prof. Dr. Helmut Ehrenberg angefertigt.

Hiermit versichere ich, die vorliegende Arbeit selbstständig verfasst und keine anderen als die angegebenen Quellen und Hilfsmittel verwendet sowie Zitate kenntlich gemacht zu haben. Die Dissertation wurde bisher an keiner anderen Hochschule oder Universität eingereicht.

M. Sc. Jiali Peng